

**SELF-ASSEMBLY MICROFABRICATION OF MULTILAYERED
HELICAL NANOMEMBRANE AND ITS APPLICATION AS
MICROSWIMMING ROBOTS**

by
MILAD SHOJAEIAN

Submitted to the Graduate School of Natural Science and Engineering
In partial fulfillment of the requirement for the degree of
Master of Science

Sabanci University

July 2021

**SELF-ASSEMBLY MICROFABRICATION OF MULTILAYERED
HELICAL NANOMEMBRANE AND ITS APPLICATION AS
MICROSWIMMING ROBOTS**

APPROVED BY:

[Redacted signature line]

DATE OF APPROVAL: 13/07/2021

© MILAD SHOJAEIAN 2021

All Rights Reserved

ABSTRACT

SELF-ASSEMBLY MICROFABRICATION OF MULTILAYERED HELICAL NANOMEMBRANE AND ITS APPLICATION AS MICROSWIMMING ROBOTS

MILAD SHOJAEIAN

Mechatronics Engineering, M.Sc. Thesis, July 2021

Thesis Supervisor: Prof. Dr. Serhat Yeşilyurt

Keywords: Microswimming robots, self-assembly micro-fabrication, multilayer nanomembranes, numerical modeling, magneto-acoustic propulsion

Microswimming robots are promising agents in biomedical disciplines due to their various potential functionality such as targeted drug delivery and microsurgery. This dissertation is dedicated to three main areas: (i) development of a self-assembly micro-fabrication technique to generate micro-scale, non-crystalline, multilayer, magnetic and helical nanomembranes; (ii) modeling and simulation; and (iii) magneto-acoustic propulsion. A thin film of nickel is sandwiched between two silicon nitride nanolayers with internal strain mismatch. Two methods of fabrication are proposed to determine the direction of rolling. The first one is changing the width-to-length aspect ratio and thickness, and the second one is topological modifications by grating the top layer of the tri-layer composite. The process of rolling from a 2D ribbon to a 3D shape is modeled by COMSOL V5.6. by moving boundary conditions inspired by the real rolling process. The results are compared and validated by experimental data with an error of less than ten percent for all cases. Near-wall swimming of the fabricated microrobots is characterized inside a cuboid reservoir filled with isopropyl alcohol by means of a rotating magnetic field. The effects of vibration are studied by using a piezo transducer next to the reservoir. The results show a maximum swimming velocity of 125 $\mu\text{m/s}$, which is improved to 250 $\mu\text{m/s}$ under 1 kHz vibration frequency.

ÖZET

KENDİLİĞİNDEN OLUŞMA YÖNTEMİYLE ÇOK KATMANLI SARMAL NANO-MEMBRAN ÜRETİMİ VE MİKROYÜZÜCÜ ROBOT OLARAK KULLANIMI

MILAD SHOJAEIAN

Mekatronik Mühendisliği YÜKSEK LİSANS TEZİ, Temmuz 2021

Tez Danışmanı: Prof. Dr. Serhat Yeşilyurt

Anahtar kelimeler: Mikroyüzücü robotlar, kendiliğinden şekil alma yöntemiyle mikro-
üretim, çok katmanlı nanomebranlar, sayısal modelleme, magneto-akustik yüzdürme

Mikroyüzücü robotlar hedef dokuya ilaç teslimi ve mikroşiruji gibi çeşitli biyomedikal uygulamalar için ümit vaat eden yapılardır. Bu tez üç ana alana odaklanmıştır: (i) mikro ölçekte, kristalize olmayan, çok katmanlı manyetik ve sarmal yapıda nano-membranlar elde etmek için kendiliğinden şekil alma temelli bir mikro-üretim yönteminin geliştirilmesi, (ii) bu yapıların modelleme ve simülasyonu ve (iii) bu yapıların manyetik ve akustik tahrikle yüzdürülmesi. İnce bir nikel tabakası, aralarında iç gerinim farkı bulunan iki silisyum nitrür nano-tabakanın arasına yerleştirilmiştir. Yapının yuvarlanma yönünün tayini için iki farklı üretim yöntemi önerilmiştir. Bunların ilki, genişlik ve uzunluk oranıyla kalınlığın beraberce değiştirilmesi, ikincisi ise üç-katmanlı yapının üst katmanında rendelenmiş bir yüzey profili elde edilmesidir. 2-boyutlu bir şeritin 3-boyutlu sarmal bir yapıya dönüşümü, deneylerde gözlenen sarmalanma sürecinin hareket eden sınır şartlarıyla temsil edilmesiyle COMSOL V5.6 programında modellenmiştir. Simülasyon sonuçları deney sonuçlarıyla kıyaslanmış ve bütün vakalarda yüzde ondan az bir hata payı gözlemlenmiştir. Üretilen mikro-robotların duvar yakınında yüzme performansı izopropil alkol ile doldurulmuş kübik bir rezervuarda ve döner manyetik alan altında karakterize edilmiştir. Rezervuarın yanına yerleştirilen bir piezoelektrik dönüştürücü yardımıyla titreşimin etkileri de çalışılmıştır. Titreşim olmaksızın elde edilen en yüksek hız olan 125 $\mu\text{m/s}$, 1 kHz titreşim frekansı altında 250 $\mu\text{m/s}$ 'ye çıkmıştır.

ACKNOWLEDGEMENTS

Firstly, I would like to thank Professor Serhat Yeşilyurt, my thesis advisor over the last three years. If I had to select the best feature of my professor, I would definitely opt for his motivation in addressing the problems and giving precious opinions during the project. Like a student, he always keeps abreast of the projects, and this motivates the students to boost his/her sense of responsibility. I am glad that I have had this chance to work with him, assisting me to take steps towards the academic world more professionally.

I would like to thank Professor Mehmet Ali Gülgün, Dr. İsmet İnönü Kaya, Dr. Ayhan Bozkurt, and Dr. Murat Kaya Yapıcı for sharing their invaluable advice and experience. I am also thankful to my other jury members, Dr. Bekir Bediz, and Dr. Yegân Erdem, for giving precious advice to make this thesis more professional. I would like to thank my colleagues, Fatemeh Malekabadi, Dr. Omid Babaie Rizvandi, Dr. Murat Gökhan Eskin, and Dr. Ebru Demir. My special thanks go to Dr. Hakan Osman Çaldağ for his infinite support during the project. I also would like to thank the SUNUM specialists specifically Süleyman Çelik, Onur Serbest, and Dr. Cenk Yanık for their suggestions and support in cleanroom fabrications.

I am very thankful to all of my dear friends at Sabanci university who not only motivated me throughout the project but also taught me how one can share his/her know-how knowledge with no hesitation. I specifically would like to appreciate Kosar HassanNezhad who has always stayed by my side and encouraged me to take strong steps.

Last but not least is my beloved family who has always paved the way for studying. I have been far from them for a long period of time and what made this time bearable has been their existence and their emotional support. I love them to the moon and back.

This thesis is dedicated to my beloved family

TABLE OF CONTENTS

LIST OF FIGURES	III
LIST OF TABLES	V
LIST OF ABBREVIATIONS.....	VI
1 INTRODUCTION	1
1.1 BACKGROUND	3
1.1.1 Microfabrication.....	3
1.1.1.1 Additive microfabrication.....	3
1.1.1.1.1 3D Printing	3
1.1.1.1.2 Direct Laser Writing (DLW).....	3
1.1.1.1.3 Glancing Angle Deposition (GLAD)	4
1.1.1.1.4 Vapor Phase Deposition (Growth)	4
1.1.1.1.5 Electrospinning.....	5
1.1.1.2 Self-assembly of strain-induced thin-film ribbons	6
1.1.1.2.1 Scrolling: theoretical aspects.....	6
1.1.1.2.2 Self-rolled up nanomembranes.....	7
1.1.1.2.2.1 Crystalline nanomembranes	7
1.1.1.2.2.2 Amorphous nanomembranes	8
1.1.1.2.3 Self-assembled helical nanomembrane	10
1.1.1.2.3.1 Crystalline nanomembranes	10
1.1.1.2.3.2 Noncrystalline nanomembranes	11
1.1.2 FEM Modeling and Simulation.....	12
1.1.3 Magnetic and acoustic propulsion.....	15
1.2 MODELING, FABRICATION, AND PROPULSION OVERVIEW AND NOVELTIES	19
2 METHODOLOGY	21
2.1 FABRICATION PROCESS	21
2.1.1 Microfabrication procedure.....	21
2.1.1.1 Step 1: Sacrificial layer deposition	23
2.1.1.2 Step 2: Low frequency (LF) silicon nitride deposition.....	25
2.1.1.3 Step 3: Nickel deposition.....	29
2.1.1.4 Step 4: High frequency (HF) silicon nitride deposition.....	31
2.1.1.5 Step 4: Lithography	33
2.1.1.5.1 Mask.....	34
2.1.1.5.2 Photolithography process	35
2.1.1.6 Step 5: Etching.....	38
2.1.1.7 Step 6: Second lithography.....	41
2.1.2 Problems in fabrication	43
2.2 MODELING AND SIMULATION PROCESSES.....	45
2.2.1 Rolled-up ribbons.....	45
2.2.2 Imperfect and perfect helices.....	52
2.3 MAGNETIC AND ACOUSTIC PROPULSION SETUP	54

3	RESULTS AND DISCUSSIONS.....	60
3.1	FIRST METHOD: GEOMETRY MODIFICATION (THICKNESS VARIATIONS).....	60
3.2	SECOND METHOD: GEOMETRY MODIFICATION (GRATING)	70
3.3	PROPULSION	75
3.3.1	Magnetic swimming performance in an mm-scale tube.....	77
3.3.2	Magneto-acoustic swimming performance in a cuboid reservoir	79
4	CONCLUSIONS.....	82
4.1	FUTURE WORKS.....	83
	BIBLIOGRAPHY	87
	APPENDIX	93

LIST OF FIGURES

Fig. 1.1.	Schematic view of a pre-stressed bilayer.....	7
Fig. 2.1.	Process flow of fabricating self-rolled up microstructures	22
Fig. 2.2.	Inside view of the PVD device used.....	24
Fig. 2.3.	The sample before (a) and after (b) chromium deposition	25
Fig. 2.4.	A part of the Surface profile of chromium deposited wafer	25
Fig. 2.5.	Sample with 160nm LF SiN _x deposited on the sacrificial layer	27
Fig. 2.6.	Profilometry configuration for measuring the stress	27
Fig. 2.7.	Stress Measurement by profilometry: LF silicon nitride with a thickness of 160 nm: a) parallel, and b) orthogonal	29
Fig. 2.8.	Nickel thin film deposited by E-beam PVD on LF Silicon nitride.....	30
Fig. 2.9.	Stress measurement of nickel: a) parallel to the flat edge of the silicon substrate, b) orthogonal to the flat edge.....	31
Fig. 2.10.	Ellipsometry results of a 24-minute deposited SiN _x (HF).....	32
Fig. 2.11.	Stress measurement of SiN _x (HF): a) parallel to the edge of the wafer, and b) orthogonal to the edge	33
Fig. 2.12.	Final mask designed for batch fabrication.....	35
Fig. 2.13.	Wafer coated with 1.4μm PR	36
Fig. 2.14.	Photolithography device	38
Fig. 2.15.	Etching processes: a) RIE of HF, b) wet etching of Nickel, c) RIE of LF and removing PR.....	40
Fig. 2.16.	Schematic view of grating parameters.....	41
Fig. 2.17.	Microscopic image of the grated pattern after photolithography.....	42
Fig. 2.18.	Wafer slicing by the dicing saw.....	42
Fig. 2.19.	Schematic view of releasing the structures from the substrate	48
Fig. 2.20.	SEM image of a rolled-up bilayer ribbon (LF=32 nm, HF=60 nm).....	50
Fig. 2.21.	Simulation result of rolled up bilayer nanomembrane with an LF/HF=32 nm/60 nm	51
Fig. 2.22.	Schematic view of the general modeling of the etching process	52
Fig. 2.23.	Time-lapse images of the rolling of a ribbon under etching process (L=10 W, C/W=3.5),	53
Fig. 2.24.	a) Helmholtz coils, and b) magnetization, and propulsion schematic	56
Fig. 2.25.	a) Schematic exploded view of the mold, and b) fabricated aluminum mold	57
Fig. 2.26.	PDMS chamber bonded on a microscope glass slide	57
Fig. 2.27.	The glass-PDMS-transducer setup	58
Fig. 2.28.	The setup used for micro swimming performance	59
Fig. 3.1.	Mask designed for investigating geometric effects in rolling.....	61
Fig. 3.2.	Effect of aspect ratio on rolling while the length is 800 μm. a) L/W=1, and C/W=0.35, b) L/W=2, and C/W=0.7, c) L/W=4, and C/W=1.4, and d) L/W=8, C/W=2.8 (Scale bar size is 200μm)	63
Fig. 3.3.	Modeling and simulation of rolling process: steps of releasing	64
Fig. 3.4.	Energy minimization graph	65
Fig. 3.5.	Diameter changing behavior regarding thickness variation (black filled circles are simulation rolled-up ribbons, red filled circles are experimental data).....	67
Fig. 3.6.	Thickness variation effect while T-LF was kept constant at 245nm for all cases. a) THF =10 nm, b) THF=20 nm, and c) THF=300 nm. The widths of the ribbon for part i, ii, and iii are	

respectively 40 μ m, 90 μ m, and 120 μ m while the length for all cases is ten times greater than the width.....	67
Fig. 3.7. Aspect ratio and thickness modification method. a) image of an 80nm SiN _x LF/10nm SiN _x HF bilayer with a width of 70 μ m and aspect ratio of L/W=10, b) SEM image of a 15nm SiN _x LF/30nm SiN _x LF bilayer with a width of 15 μ m and aspect ratio of L/W=10, and c) image of a sandwich LF/Ni/LF layer with the thicknesses of 35nm/100nm/55nm. (i, ii, and iii are respectively related to the width of 90 μ m, 110 μ m, and 120 μ m while the aspect ratio was constant at L/W=10) .	69
Fig. 3.8. Micro helical sandwich nanomembrane fabricated by aspect ratio/thickness modifications., a) perfect helical ribbon, and b) imperfect helical ribbon	69
Fig. 3.9. Various configurations of patterned nanomembrane: a) Fully compacted helix, b) perfect helix, and c) imperfect helix. (the scale bar is 200 μ m)	71
Fig. 3.10. a) The percentage of the helical structures that are obtained based on various grating angles and depths, and b) the scatter graph of obtained compacted (red), imperfect (purple), and perfect (blue) helices with respect to the grating angles	72
Fig. 3.11. helical structures obtained by grating patterning parameters of w/L=g/L=0.025	72
Fig. 3.12. Comparison between experimental and simulation results for grating parameters of w/L=g/L=0.025	74
Fig. 3.13. Comparison between experimental and simulation results; (a) and (d) $\theta=45^\circ$, (b) and (e) $\theta=50^\circ$, (c) and (f) $\theta=60^\circ$. From a-c, w/L=g/L=0.025 while H/T _{HF} = 0.4, and from e-f, g/L=0.025, w/L=0.1 while H/T _{HF} = 0.6. For all cases L=1050 μ m, and W=120 μ m	74
Fig. 3.14. The new swimmer with 150 nm sandwich nickel.....	76
Fig. 3.15. Coordinate systems and the direction of swimming.....	76
Fig. 3.16. Time-lapse image of the movement of the microswimmer through a circular channel at magnetic frequency of 5 Hz	77
Fig. 3.17. swimming performance in a small tube. a) swimming velocity in the direction parallel to the helical axis, b) swimming velocity in the direction perpendicular to the helical axis, and c) the orientation angle of the swimmer.....	78
Fig. 3.18. Swimming trajectory under the magnetic frequency of 13 Hz	80
Fig. 3.19. Swimming performance under magneto-acoustic fields. A) forward velocities, b) lateral velocities, and c) orientation angles	81
Fig. 3.20. Vibration modes for two acoustic frequencies, 1 kHz left, and 10 kHz right.....	81

LIST OF TABLES

Table 2.1. PECVD Recipe for LF	26
Table 2.2. PR spin coating recipe	36
Table 2.3. PMMA Spin Coating Recipe.....	36
Table 2.4. Photolithography Exposure Parameters	37
Table 2.5. RIE Recipe for LF and HF SiN _x	39
Table 2.6. Material and mechanical properties.....	49
Table 2.7. Mesh and Section independence study (C=50 μm).....	50
Table 2.8. Comparison of 2D and 3D simulation results with experimental data	51
Table 2.9. The properties of the coils	56

LIST OF ABBREVIATIONS

DLW	Direct laser writing
GLAD	Glancing angle deposition
CVD	Chemical vapor deposition
CNT	Carbon nanotubes
CNW	Carbon nanowires
VLS	Vapor-liquid-solid
MOCVD	Metal organic chemical vapor deposition
DLC	Diamond like carbon
PR	Photoresist
PECVD	Plasma enhanced chemical vapor deposition
PVD	Physical vapor deposition
PMMA	Poly methyl methacrylate
LF SiN_x	Low frequency silicon nitride
HF SiN_x	High frequency silicon nitride
SEM	Scanning electron microscopy
FEM	Finite element method
EBL	Electron beam lithography
MIBK	Methyl isobutyl ketone
RIE	Reactive ion etching
IPA	Isopropyl alcohol
DI-water	Deionized water
GUI	Graphical user interface
VSM	Vibrating sample magnetometer

1 INTRODUCTION

In the fast-growing scientific world, microrobots with various forms of shapes, and motion mechanisms, have been utilizing extensively due to their unique functionalities which are inaccessible for macro scale robots [1]. The designing of the majority of such robots, however, are inspired by nature, so that they can be directly fabricated from natural patterns [2], or manufactured by synthetic materials [3]. In order for the robots to be mobilized, an array of methods have been proposed that can fall into two categories: 1) off-board actuation including magnetic field, acoustic field, and light source of energy; and 2) on-board power sources like chemical energy and electrical energy [4, 5].

This thesis will go over one kind of bio-inspired artificial microrobot (i.e. microswimming robots) that have drawn extensive attention over the last two decades due to their span of applications specifically in the biomedical discipline, ranging from drug delivery and micromanipulation [6-9] to biochemical detections [10]. The small scale of such robots poses a challenge in the mechanism of locomotion; as depicted in Eq. (1-1), at low Reynolds numbers ($Re \ll 1$) where the viscous forces dominate the inertial forces, the hydrodynamic equation could be considered time-independent (i.e. Stokes flow). That is, reciprocal motions mechanism, like fish swimming, would not be effective anymore in gaining net displacement [11, 12].

$$Re = \frac{F_{inertial}}{F_{viscous}} = \frac{\rho v^2 L^2}{\mu v L} = \frac{\rho v L}{\mu} \quad (1 - 1)$$

where, ρ , v , L , and μ respectively stand for density of the fluid (kg/m^3), speed (m/s), characteristic dimension (m), and dynamic viscosity ($\text{kg} \cdot (\text{m} \cdot \text{s})^{-1}$). As an alternative, the motion mechanisms of ciliated and flagellated natural organisms like *E-coli* bacteria [13], which are based on generated propagating waves, have come into play. For instance, *Monotrichous* bacteria with a single flagellum consists of a head and a helical tail; the head generally provides a torque to rotate the tail, resulting in backward wave propagation, leading to the propulsion of the whole swimmer forward or backward [14-16].

To replicate this behavior, and also, to remotely propel and control the artificial microswimmers, a wide array of methods has been proposed [17-21], among which magnetic and acoustic actuation fields play integral roles in both in-vivo and in-vitro applications due to their viability, controllability and permeability properties [4]. In terms of safety, also, the human body is not at risk in case of using static magnetic fields less than 8T [22]. On the other hand, the acoustic field is a biocompatible off-board actuation force, whereby one may convey the required energy to move the microswimmers with various shapes using the generated waves as acoustic streaming or vibration modes [23, 24].

These unique properties have allowed researchers to mimic the mobilization behavior of *E-coli* bacteria by using a magnetic head attached to a helical tail. Having the magnetic head rotated by a magnetic field (generally by Helmholtz coils), the required torque for rotation of the helical tail is provided, leading to the corkscrew-like motion of the whole microswimmer into fluid [25-28]. Another motion scenario emanated from the *Spirochete* bacteria locomotion mechanism, which is also appropriate for high viscous environments [15, 21, 29], is when the microswimmers lack a magnetic head; instead, the whole helical tail is made out of magnetic materials making it possible to be rotated by external rotating magnetic fields [2, 8, 30-34].

So far, a brief explanation about the bio-inspired microswimming robots and the mechanism of locomotion has been discussed. However, the most challenging part of the microswimmers is the fabrication of micro helical tails which are amongst the new generation of 3D microstructures. Also, since the fabrication of such micron-scale helices is incredibly costly and time-consuming, nowadays, modeling and simulation software is employed to develop robust designs with the final cost of the fabrication reduced substantially. In the following subsections, a literature review will be given first about ubiquitous fabrication procedures of swimmers ranging from additive manufacturing to self-assembly techniques. Then, a brief review of modeling and simulation methods in the literature, followed by the swimming performance of the fabricated swimmers will be given. Finally, a brief explanation of the methods employed for modeling, fabrication, and propulsion in the thesis will be given, together with novelties and comparisons with prior literature.

1.1 Background

1.1.1 Microfabrication

A broad range of microfabrication techniques can be used in the manufacturing of micro helical structures [35]. Having an eye on some of the most prevalent and significant techniques, we will review the nanomembranes self-scrolling fabrication techniques, as a part of the main objectives of this thesis.

1.1.1.1 Additive microfabrication

1.1.1.1.1 3D Printing

With the advent of additive manufacturing by some novel techniques, like 3D printing, over the past decade, flexibility in the fabrication of complicated microstructures has developed considerably. In our group, previously Acemoglu and Yesilyurt demonstrated millimeter-scale swimmers manufactured by 3D printing of structures made out of VisiJet EX 200 polymers [36] with a cylindrical polarized neodymium magnet attached to the head for manipulation and propulsion of the swimmer by an external rotating magnetic field. The performance of this kind of configuration was satisfactory so that, later on, Caldag and Yesilyurt analyzed the motion and developed control methods of such swimmers [37, 38]. This kind of method of fabrication although enjoy several advantages like being cost-effective, fast, and portable in small sizes, however, it is limited to studies for the understanding of the mechanism and not suitable for micro-scale applications. Hence, as even a slight change in the final geometries of the microswimmer can affect the performance of the swimmer dramatically [39], this method requires many modifications in terms of nozzle resolution and the material used.

1.1.1.1.2 Direct Laser Writing (DLW)

DLW is another form of additive fabrication, whereby generating feature sizes as small as few microns is feasible. The high special resolution of this method is due to using a technique called two-photon absorption. The photosensitive materials constitute the basis of the process. Once the laser shines, the regions of the material that are exposed to the focal spot will be polymerized. As a result, moving the laser beam through the material will create 3D structures that will be remained on a substrate (e.g. glass) when exposing to a developer. So far, some works have employed this

method to create micro helical swimmers made out of bilayer [32] or composite [34] magnetic materials. Moreover, recently, research has been carried out by Ceylan et.al [8], in which printed microswimmers have a bio gradable material, making them medically functional. This microswimmer is intended for cargo delivery and has a diameter of 6 μm and a length of 20 μm , along which a cylindrical core (with double cones at both ends of the swimmer) is covered by a double helix. The material used in this process is a combination of iron oxide magnetic nanoparticles, gelatin methacryloyl, and MMP2 enzyme. The authors demonstrated that this microswimmer can be degraded by this enzyme as a biocompatible byproduct after 118 hours. Tottori et.al [31], also proposed another novel idea by which the core of the helical swimmer is made out of SU8 by DLW, and then, to make it magnetic, they covered the surface by physical vapor deposition of Ni/Ti.

1.1.1.1.3 Glancing Angle Deposition (GLAD)

One technique that employs both mechanical rotations and tilting together with physical evaporation to reach a 3D structure is called GLAD. This method is an improved version of the conventional oblique angle deposition method with a difference that the position of the substrate is not stationary. Instead, it is mounted on an inclined rotating sample holder and the deposition of 3D structures is controlled utilizing a feedback controller. Although helpful, the final structure may suffer from some caveats including large grain sizes, and surface and body defects, because of shadowing effects [40-42]. However, this method has been used in literature to fabricate thin film micro helical configurations. For instance, Robbie et.al [43, 44] produced nano helical columns made out of MgF_2 , SiO_2 , and CaF_2 , with a wavelength of 50 nm to 2 μm . the authors suggested that by using special materials with low adatom mobility, fabrication of a few nanometer sculptures would be attainable as well. In terms of magnetized swimmers, another work by Ghosh et al [45] demonstrated the GLAD method to fabricate micro helices made out of silica followed by simple thermal evaporation to cover the structures with a ferromagnetic material (i.e. Cobalt).

1.1.1.1.4 Vapor Phase Deposition (Growth)

This method is mainly based on the vapor transport and reaction in a specific environment. Because of the versatility of conditions, one can have structured materials fabricated. Mostly, the Chemical vapor deposition (CVD) method is employed to create novel materials, like

Carbon nanotubes (CNTs) or Carbon nanowires (CNWs) by means of a vapor-liquid-solid (VLS) procedure. To this end, carbon inside the precursor gas is a liquid catalyst droplet that after saturation it nucleates at lower temperatures creating CNT and CNW. This kind of structure can form a helical structure in specific circumstances which is attributed to the interface between carbon and catalyst at the tip of the structure. Several models so far have explained this phenomenon which is believed to be due to introduced stress at the interface and also experiencing deposition nonuniformity [46-48], wettability at the interface [49, 50], and in a more general point of view of VLS process, the reason why such unique geometries generated in some other materials irrespective of carbon-based structures [51, 52]. Although the fabrication process of such helices is not straightforward, however, their nanoscale diameter and wavelength together with electromagnetic properties, make them useful structures that can be utilized in future studies in various applications [53].

1.1.1.1.5 Electrospinning

The method of fabrication consists of some steps: 1) selecting a material with a proper molecular cohesion, 2) driving this material via a syringe to form a droplet at the tip of the needle, 3) applying a high voltage and put the device near a grounded substrate. The last step causes an electric field, resulting in overcoming the surface tension of the droplet by an electrostatic repulsion force, leading to stretching of the droplet until it forms fibers beyond a critical point called Taylor cone [54]. These fibers are then collected by the grounded substrate. In terms of the helical shape of the fibers, which is mostly due to the buckling of fibers after hitting the collector, Yu et al [55] managed to produce helical fibers made out of polycaprolactone by employing a slanted glass collector, and by controlling the tilting gradient together with the gap distance between the nozzle and the glass were. Shariatpanahi et al [56] produced long micro helical polystyrene fibers with a diameter of a couple of microns in water and controlled the properties of which by varying a high frequency applied voltage. The mechanical [57], optical and thermal [58] properties show a promising potential of such fiber structures in various fields of studies. Moreover, in the future, using magnetic nanoparticles or coating by magnetic thin films is likely to increase their versatility in electromagnetic fields as well.

1.1.1.2 Self-assembly of strain-induced thin-film ribbons

Besides the methods mentioned above, there is an emerging self-assembly technique by which structured configurations (e.g. microtubes and micro helices) are produced. Since the main focus of this thesis is on such a technique, first the mechanism behind it, then, the versatility of this method in producing rolled-up thin films with various shapes will be discussed and examined.

1.1.1.2.1 Scrolling: theoretical aspects

It is evident that initially confined pre-stressed structures, once released, minimize the potential elastic energy by deforming. A tangible example would be a doubly clamped beam that is buckled as a result of increased ambient temperature, or a stretched/compacted spring. Suppose that a very thin beam (ribbon) has initial stress inside while attaching to a substrate; after releasing, it will be stretched or compacted (buckled) respectively due to initial compressive or tensile stress. In a more complicated postulate, consider a confined bilayer ribbon in each layer of which there are compressive and tensile stresses. This will result in a 3D rolled-up structure with a defined diameter based on the amount of initial strain mismatch, mechanical properties, and also geometry. In Fig. 1.1., a schematic of the free body diagram is shown for the initially stressed 2D bilayer. In Fig. 1.1. (a), the bilayer is fixed from underneath while having an initial compressive stress (indicated by the arrows pointing each other) in the first layer, and a tensile stress (indicated by the arrows pointing in opposite directions), in the second. After its release, the structure deforms to minimize its initial elastic energy. Bending moments (M_1 , and M_2) are generated due to the forces emanated from the initial stresses. Since no external forces are acting on the structure, all the forces and moments must be in equilibrium. Based on this behavior, first, we will explain different methods to achieve rolled-up structures for a wide variety of applications, and then, the techniques that are employed to turn such structures into helical ribbons will be elaborated.

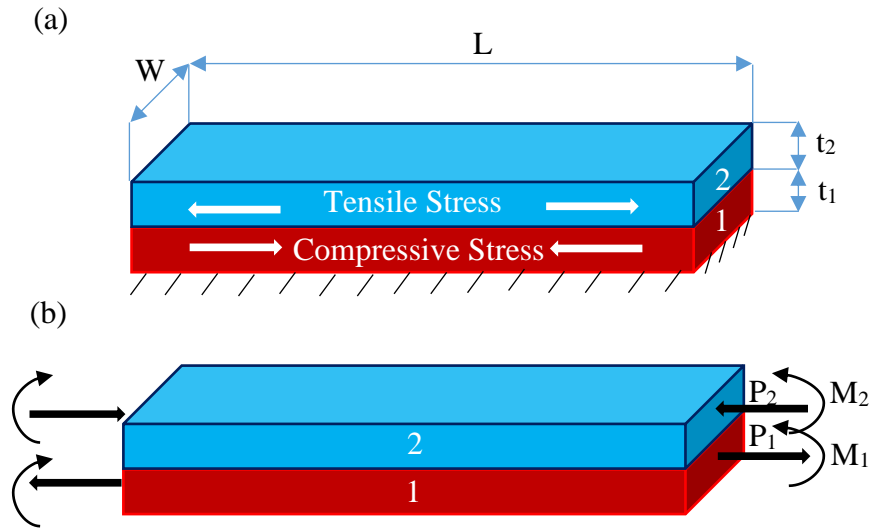


Fig. 1.1. Schematic view of a pre-stressed bilayer

1.1.1.2.2 Self-rolled up nanomembranes

1.1.1.2.2.1 Crystalline nanomembranes

Crystalline nanomembranes, usually have anisotropic mechanical properties and deform alongside a special direction because of that reason. This unique behavior has been utilized in various studies to achieve a variety of 3D structures from 2D patterned films

As a rolled-up tube, Prinz et al [59] produced an InGaAs/GaAs bilayer heterostructure with a thickness of a couple of nanometers and a diameter of $2\ \mu\text{m}$. They took advantage of the epitaxial properties of the prestressed layers so that the bilayer took the form of a tube in the predetermined crystal orientation after the removal of the sacrificial layer made of AlAs underneath the bilayer due to the elastic nonuniformity in the crystal lattice configuration of the epitaxial layers. Likewise, Zanardi Ocampo et al [60] used a similar technique to produce micromirrors. Chun and Li [61] also profited the same method of epitaxial growth of thin films by metal organic chemical vapor deposition (MOCVD) to produce nanotube semiconductors. The authors studied the effect of crystalline orientation on the rolling direction by a selective etching method using lithography processes to create etching windows. With a total thickness of 12nm, they observed rolled-up structures with a diameter of around 590nm. Moreover, as an example of the structures manufactured with the use of epitaxial nanomembranes, Yu et al [62] demonstrated the growth of epitaxial silicon on

silicon/germanium layers. The strain mismatch between the layers assisted them to achieve rolled-up tubes after detaching the structure from the silicon substrate by etching the SiO₂ sacrificial layer. As an application of the end products, the fabricated tubes were utilized as cell culture substrates. The authors demonstrated clearly how the tube diameter changes nonlinearly by playing with the thickness of the nanomembrane layers.

Golod et al [63] produced self-assembled multilayer microtubes, consisting of a combination of SiGe, Si, SiN_x, and Cr nanolayers. They used silicon (001) as a sacrificial layer to be etched selectively in a defined direction (because of different etching selectivity among different crystal orientations). As the layers have tensile, free, and compressive intrinsic stresses, after removing the silicon layer underneath, the whole structure rolled up to form a tube shape. In other works of the same authors [64], Si/SiGe tubes are fabricated by means of etching a doped silicon substrate. They used two different doping concentrations to increase the etch rate at low doped regions while high doped regions served as an etching stopper. Single crystal materials (for directional etching) have been utilized in other studies as well, i.e. Prinz and Golod [65]. Seleznev et al [66], also used a similar method to create a combination of epitaxial (InGaAs/GaAs) and amorphous (SiO₂/Si₃N₄/Au) rolled-up micro sensors and micro heaters.

1.1.1.2.2.2 Amorphous nanomembranes

Controlling the process is more demanding in amorphous nanomembrane since the mechanical properties are identically distributed. Hence, other techniques need to be taken into account in order to obtain a desired 3D shape.

Mei et al [67] used two different methods to achieve self-rolled up structures made out of a wide range of materials ranging from metals and dielectrics to diamond-like carbon (DLC). Since their focus was on non-epitaxial thin films, they used directional etching methods utilizing created slits using GLAD and also photolithography/etching techniques. The interesting part of their work is that they used a simple photoresist (PR) as the sacrificial layer which is etched away quickly and readily by acetone which has a high selectivity over all of the inorganic materials mentioned above. In another work performed by Schulze et al [68], they used the same method by GLAD technique to evaporate a bilayer of SiO/SiO₂ while leaving an etching window to remove the photoresist sacrificial layer. Such rolled-up

structures were then employed to instigate a cell culture. Huang et al [69] also utilized noncrystalline sacrificial layer and multilayer thin films. A 20nm of a sacrificial layer is evaporated by e-beam evaporation and SiN_x (LF)/ SiN_x (HF)/Ni/Au are the multilayer 2D structures grown in order by plasma-enhanced chemical vapor deposition (PECVD) and physical vapor deposition (PVD) methods. These nanolayers possess compressive, tensile, tensile, and tensile stresses, respectively, leading to rolled-up 3D structures after detaching from the substrate through a lateral etching window created in front of an edge of which.

In an interesting work by Stoychev et al [70], the final shape of the self-scrolling polymer layers is controlled by the geometric parameters of the bilayer. They showed that three indispensable parameters affecting the direction of rolling are width, length, and circumference. It is observed that the nondimensional parameters, length/circumference, and width/circumference ratios, used to describe the rolling in either long side, short side, or diagonal side of nanoribbons after etching the sacrificial layer isotopically.

Another novel study [71] describes the rolling up of a single layer of thin film by varying the stress distribution deliberately. The authors used a layer of poly (methyl methacrylate) (PMMA) as the sacrificial layer. Then using a nanoimprinting method, some slots were created through the PMMA so that the grating patterns appeared. After that, a thin layer of tens of nanometers of titanium was coated on this grated surface, so that it takes the shape of this surface. Putting the whole structure into acetone resulted in removing the sacrificial layer, leading to rolled-up tubes. This phenomenon occurred because rolling from the grated edge requires far more energy than that of other edges. Hence, one can intentionally determine the rolling direction even if using an amorphous sacrificial layer that is etched isotopically from all sides.

As an application, very recently some research has been carried out by employing noncrystalline rolled-up nanomembranes. For instance, Michaels et al [72] investigated the body modification performed on LF/HF SiN_x bilayers to control the thermal effect on the structure. Moreover, a strained multilayer (Al_2O_3 /LF/HF/CU) has been used to generate rolled-up sensors [73], interdigital capacitors [74], inductors [75], and transformers [76].

1.1.1.2.3 Self-assembled helical nanomembrane

The rolling mechanism of the helical structures is the same as the tube or ring-like nanomembrane explained earlier. However, to induce the ribbon to roll in a specific direction, whereby the helical structure is obtained, is a challenging issue since two other parameters (i.e. helical angle and wavelength) in addition to diameter emerge. Like tube/ring rolling techniques, we can categorize the methods of fabricating helices into two categories: 1) crystalline nanomembrane, 2) non-crystalline nanomembrane

1.1.1.2.3.1 Crystalline nanomembranes

In this regard, there are several works taking advantage of the anisotropy distribution of mechanical properties in crystalline thin films to produce complicated 3D shapes like helices or spirals. For instance, Prinz on Golod [65] demonstrated that even 23% of elastic anisotropy in (100) silicon is helpful to create spirals. This shape is obtained once the 2D strained micro ribbons are printed with an angle to the rolling direction. To this end, the authors oriented the ribbons on (100) and (110) silicon substrate respectively in $\langle 110 \rangle$ and $\langle 112 \rangle$ directions. As a result, both elastic and chemical anisotropy in films and sacrificial layers led to the fabrication of helical ribbons with a diameter and pitch of a couple of microns while the rolling direction was 48° . Previously, Printz et al [59] also proved that using a strained (100) InGaAs/GaAs bilayer tilted from $\langle 010 \rangle$ direction results in helical nanostructures. Similarly, Golod et al [64] used GeSi/Si nanomembrane and achieved helical ribbons. In terms of a perfect microswimmer magnetic robot, also, Zhang et al [28] fabricated an InGaAs/GaAs bilayer as a tail with a magnetic head made of Cr/Ni/Au on top of a single crystal substrate as a sacrificial layer (i.e. AlGaAs (001)). After removing the sacrificial layer, the whole structure is rolled up as a microswimmer with a helical tail and ahead.

Dai and Zhang [77] managed to come up with a model to have control over the chirality of rolled-up nanoribbons by growing materials on a silicon (111) substrate. In this research, a multilayer nanoribbon (i.e. SiGe/Si/Cr) was patterned in a clock-like configuration and then the behavior of each ribbon after wet etching of silicon substrate by ammonia was examined. Since silicon (111) enjoy the anisotropic mechanical property, the multilayer which

was fabricated by epitaxially grown method experienced the same properties. As a result, controlling the behavior of rolling is not limited to Young's modulus anisotropy of the structure. Hence, in this paper it is identified that a combination of lateral anisotropy of etching together with the orientation of nanoribbons regarding the fastest etching direction plays an integral part in controlling the scrolling behavior, leading to either rolled-up nanostructure or helical ones with various helical angles.

In other words, researchers have taken advantage of a crystalline sacrificial layer while using amorphous nanomembrane on top of which. Hence, the anisotropic essence of the crystalline sacrificial layers (due to the elastic nonuniformity) leads to a directional etching, resulting in chirality properties in the created structures. For instance, Huang et al [69] deposited a multilayer of noncrystalline nanomembrane (LF SiN_x/HF SiN_x/Ni/Au) on top of silicon (110) as a sacrificial layer, while patterning it as ladder-shaped ribbons with an angle of 15° relative to (110) facets.

1.1.1.2.3.2 Noncrystalline nanomembranes

So far, we have reviewed the fabrication of helical structures with the help of crystalline nanostructures properties in either the sacrificial layer or the whole nanomembrane. However, only a few studies have been dedicated to noncrystalline nanomembranes. In such cases, the mechanical properties of the nanostructures are isotropic with a uniform stress distribution. As a result, when the sacrificial layer is removed uniformly, every side of the ribbon is supposed to be rolled up identically. Therefore, some modifications are to be imposed deliberately to the geometry of the ribbons to make the structure scroll in a desirable direction. For instance, as mention in 1.1.2.2.2, using an etching window assists one to reach a perfect rolled-up nanomembrane.

In the case of self-rolled up helical ribbons, however, only a few methods have been proposed until now. If we consider a ribbon in a 3D coordinate system (length in x-direction, width in y-direction, and thickness in z-direction), modification through width and thickness can end up with stress and bending stiffness anisotropy. In this regard, Zhang et al [78] by modifying the tip of the ribbons showed that slanted tips may affect the chirality of the final

structure (either in shape or in rolling direction). In a more completed version of this method, replacing 2D perfect ribbons with slanted head ribbons resulted in helical structures. The reason behind this is asymmetric etching which causes the driving force to be anisotropic. In this model, the authors demonstrated that playing with the angle of the head enables one to obtain helices with different helical angles. The repeatability of the method was proved for amorphous, polycrystalline, and nanocrystal nanomembranes [79]. The authors in previous research [80], also, unveiled the role of 2D patterning in achieving various 3D structures. For instance, using a hockey stick-like 2D pattern with a tapered base and slanted head with different angles make it possible to reach imperfect helical structures.

Other studies also took advantage of stiffness anisotropy that is achievable manually just by changing the topography of the ribbons. For example, Huang et al [71] by creating oriented patterns with height differences, fabricated self-assembled helical nanoribbon. They just evaporated a single layer of Titanium on a slanted wrinkled shape PMMA mold. As a result, an anisotropic stiffness and a nonuniform strain mismatch distribution were intentionally induced to the thin film. Having the layer released from the substrate by solving the PMMA in acetone, and due to energy minimization, the layer tends to roll up from a flat edge rather than a wrinkled edges. As a consequence, the rolling direction allows the ribbon to form a helical shape with different helical angles and pitches based on the primary angle of the slots created in the structure. In another study by Cui et al [81], the impact of anisotropic bending stiffness on the behavior of rolling was investigated. They fabricated a bilayer structure, one of which is a prestrained polymer (i.e. Grafix Shrink Film) which is sensitive to temperature variation, and the other layer is a film (i.e. AL sheet) with a defined stiffness. As a result, using different patterns, a wide range of 3D structures was fabricated just because of stiffness variations.

1.1.2 FEM Modeling and Simulation

Simulations and modeling software are tools paving the way to take vigorous steps towards novel designs. In prestrained rolled-up structures, there are a couple of simulation methods, the results of which have been compared to the obtained results in fabrication. Among all,

those which resemble the fabrication processes are more reliable, versatile, and for sure, more challenging. This section aims to have an overview of some important models used to simulate the behavior of self-rolled-up structures.

Guo et al [82] modeled prestressed linear elastic bilayer by mean of the structural mechanic module and tetrahedral meshes in COMSOL Multiphysics 4. For the sake of simplicity, they took Young's modulus as 1 which is assumed to be isotropic through the structure, and also considered the density as zero as a result of the quasi-static method. Considering a misorientation angle about the X and Y axes, they studied the bistability behavior of the structure after freeing from the predefined constrained from the corners. By changing the constrained to the middle and one edge, they also studied the doubly bent behavior of the structure. In another work [83], they also showed that both geometric misorientation and anisotropic implemented initial strain would result in either helical, twisted, or ring shape structures. To avoid the structure from perfectly releasing and floating, they intentionally fixed the bilayer at a corner point. Using the same method mentioned above by COMSOL V4.3a for crystalline materials, Chen [84] studied the chirality of different configurations, including V-shaped and slanted head ribbons, made out of multilayer nanomembranes (i.e. SiGe/Si/Cr). He also revealed that how geometric nonlinearity could be of significance (as previously proved in [85] for bistable structures) in self-rolled-up structures by verifying his model to the experimental data achieved by Zhang et al [78].

In another work that was carried out by Chen et al [86] by using ABAQUS FEM software, composite layups together with four nodes doubly curved thin/thick shell elements were employed to model a prestrained bilayer. The mismatch strain then was obtained by defining various thermal expansion coefficients while changing the temperature. Using a quasi-static solving model, and dividing the whole structure into small strip elements, and releasing them step by step, they analyzed the rolling procedure. To have control over the rolling intentionally, they introduced a constraint with delayed releasing.

Huang et al [69] used a transient quasi-static molding to simulate the behavior of amorphous multilayer ribbons made out of LF SiN_x and HF SiN_x. The authors applied a fixed boundary condition on the bottom of the bilayer which is released step by step employing transient quasi-static modeling. Each step was taken to be around 0.05 of the circumference

of the rolled-up structure. Geometric nonlinearity in this work was also taken into account as a result of large deformation. They measured the stress inside each layer and then implemented different thermal expansions while using appropriate temperature increments to reach that amount of stress inside each layer. They confirmed their model by verifying the results by experimental images coming out of scanning electron microscopy (SEM). In the other phase of their work, they investigated the behavior of structures that are released anisotropically from underneath. For instance, to model helical ladders, they took advantage of moving boundary conditions in the direction of the actual etching process. This method has been proved to be reliable so that some other papers used such a method to model the rolled-up structures in different applications [74, 76]. Likewise, Chun et al [87] investigated the effects of geometry on the behavior of the rolling procedure. The authors utilized ABAQUS software by employing eight-node thick shell elements in order to be able to examine the properties variation alongside the thickness. In their study, the materials (InGaAs/GaAs) were assumed to be fully elastic. By considering the etching process to be isotropic, they elucidated that not only aspect ratio together with the diameter of the structure play integral parts in rolling direction, three other significant factors (i.e. ultimate energy, history dependency, and kinetic control of isotopic etching process) also determine the final shape of the rolled-up structure.

Chen et al [88] by employing ABAQUS software, used two different methods in their modeling of grated structure. The first one was quasi-static in which the structure is divided into a set of segments perpendicular to the rolling direction and then made them released gradually until it is freed completely. Another method was employed in the case of isotropic etching in which the releasing of the structure is not predefined. They performed such simulation as a transient model and examine the rolling behavior of either rolled-up or helical nanomembrane. Then, they investigated the effects of some significant parameters (patterns density and thickness together with aspect ratio) in the final shape and geometry of the helices.

Xu et al [89], recently in an interesting paper, used a pre-layer nanomembrane (e.g. Au on glass) to create van der Waals interaction. Then, a multilayer of other materials, like SiO/Fe/Ag, was deposited as an active nanomembrane with initial stress inside. Ejecting a microdroplet at a specific edge of the patterned structure leads to having liquid-triggered movement of the structure because of overcoming the van der Waals force and pre-layer

delamination from the substrate. This leads to generating various shapes (tubular and helical microstructures) just by changing the location of the droplet injection. Then, they predicted this behavior by FEM modeling. To this end, they modeled the system as a quasi-static problem in which the structure is detached from the substrate gradually and step by step by defining a set of segments which represent the etching process. Regarding the location of release, the ribbon can form either a tubular shape or a helical structure; inspired by this fact, the segments were considered as either straight lines or slanted lines, respectively.

1.1.3 Magnetic and acoustic propulsion

As discussed at the beginning of this chapter, magnetic helices can be employed as microrobots. If these robots are capable of moving by an external source of energy, they can be served for bio-application. To this end, two ubiquitous sources of energy have been proposed (i.e. magnetic field and acoustic field). To use the magnetic field, one may utilize materials with a suitable response in the fabrication of the swimmers, such as ferromagnetic materials (e.g. nickel, steel, iron, and cobalt). For this reason, the swimmers are made out of either a magnetic helical and helical tail, or just a magnetic helical tail. The magnetic fields have to be rotated to provide the required torque for the rotation of the swimmer. To this end, Helmholtz coils are employed which are mainly consist of a couple of opposite pairs with a center axis perpendicular to the helical axis. However, in some cases, to control the orientation of the swimmer, a pair of coils with the center axis parallel to the helical axis is also added to the other mentioned pairs. The acoustic field, unlike the magnetic field, can be applied to all kinds of small robots. The acoustic field can be exerted by a wide range of transducers like focus transducers or piezoelectric disk transducers. In this section, we will have a brief review of the magnetic and acoustic locomotion of microswimmers, and examine the behavior of the swimmer by discussing the swimming velocities.

Gao et al [2] collected spiral xylem vessels with a fiber diameter of 2 μm on the surface of which a bilayer of Ti/Ni was deposited. They stretched and diced them mechanically to produce microswimming robots with diameters between 10-60 μm that were tested under magnetic field by triaxial Helmholtz coils. The magnetic field strength was fixed at 10 G with

varying the frequency ranging from 10 to 80 Hz. They reported that the swimmer at low frequency suffers from wobbling following by cork-screw-like motion at higher frequencies, ending up with a step-out at high frequencies greater than 80 Hz. Beyond step-out frequencies, the torque generated by the magnetic field is not sufficient to overcome the fluidic drag, leading to a decrease in the swimmer's velocity. Hence, the velocity increased linearly up to the maximum velocity of 250 $\mu\text{m}/\text{sec}$ at the frequency of 80 Hz and then experienced a descending behavior.

Li et al [30] utilized the template-based electrodeposition method to produce submicron rod helices made of Pd/Cu with a minimum diameter of 100 nm and length of 600 nm that were coated with nickel to make it magnetized. They used three swimmers with different diameters (i.e. 100 nm, 200 nm, and 400 nm) and observed the swimming behavior of which under the magnetic field at three various frequencies of 90 Hz, 120 Hz, and 150 Hz. They demonstrated a linear increase for the swimming velocity by increasing the frequency, while the bigger the swimmer resulting in higher velocity up to 15 $\mu\text{m}/\text{s}$ at $f=150$ Hz. For lower frequencies, they discussed tumbling motion that changes to cork-screw motion at higher frequencies greater than 100 Hz.

In an interesting work, Tottori et al [31] studied how two swimmers can be assembled and disassembled at specific frequencies owing to magnetic interaction. They fabricated two different swimmers with the help of a 3D lithography process and coated them with Ni, which was going to be propelled under a rotating magnetic field of 1 mT. two swimmers with the length of 24 μm and 35 μm in length and diameters of 4 μm and 6 μm were fabricated by that method. The authors demonstrated that the two swimmers can swim together as a bigger swimmer at low frequencies less than 40 Hz due to the dominant magnetic force than drag force in the smaller swimmer. However, as the frequency increases the counterbalance between the magnetic and fluidic forces change in smaller swimmer leading to a separation.

Zhang et al [25] produced microswimming robots made out of trilayer tail (i.e. InGaAs/GaAs/Cr) and head (Cr/Ni/Au) using the self-assembly technique that resulted in a diameter of 2.8 μm . To check the behavior of the swimmer, they produced both small and large magnetic heads. First, for the large head swimmer, the authors used three different magnetic fields of 1 mT, 1.5 mT, and 2 mT and increased the frequency from 5 Hz to 35 Hz.

They observed that swimmer velocity increases by increasing the frequency up to step-out level. Also, they concluded that due to the higher torque generated by 2 mT, the swimmer would swim at higher frequencies. As a comparison, they investigated the velocity-frequency variation of the two swimmers at the magnetic field of 2 mT. As a result, it is concluded that although the larger head has a lower velocity rather than the smaller one due to higher forward viscous drag, however, it can rotate at higher frequencies greater than the step-out of the smaller swimmer, leading to a velocity of around 12 $\mu\text{m/s}$ at $f=18$ Hz. This is believed to be due to the larger mass of Ni that can result in stronger magnetic torque.

Tottori et al [32] fabricated a pile of microswimming robots by employing the DLW method followed by PVD nickel/titanium coating. The fabricated swimmers had a length and diameter of 8.8 μm and 2 μm , respectively. The authors characterized the performance of the swimmers by employing both static and rotation magnetic fields. It is shown that the geometry can affect the magnetization so that the magnetization in larger length/diameters and lower helical angles are more preferable in the helix axis. On the contrary, once the length/diameter is decreased while the helical angle is increased, the magnetization closes to the perpendicular axis (radial axis) of the helical axis. This anisotropic magnetization, therefore, leads to misaligned swimming specifically at low magnetic frequencies. At higher frequencies, where the wobbling is disappeared and the swimmer enters a stabilization region, the swimmer aligns itself concerning the magnetic field. the authors also demonstrated that in the case of having all parameters fixed except for diameter, the swimmers with higher diameters show better performance in terms of velocity. Moreover, it was shown that the swimmer's velocity in DI-water and fetal bovine serum are the same, indicating that the velocity-frequency behavior of the swimmer would not be affected by viscosity.

Ceylan et al [8] manufactured double helix microswimming robots made of biodegradable materials while using iron oxide nanoparticles as magnetic materials that were magnetized under a uniform magnetic field in the course of fabrication. The authors observed that their fabricated swimmers with a diameter of 6 μm and length of 20 μm can show wobbling behavior at low frequencies less than 3 Hz, followed by cork-screw motion up to $f=5$ Hz with the maximum velocity of around 4 $\mu\text{m/s}$, and finally, experience step-out at higher frequencies.

Li et al [24] studied the behavior of magneto-acoustic hybrid nano swimmers. They fabricated the swimmer using a template-assisted electrochemical deposition method so that the swimmer consist of a magnetic Ni coated Pd nano spring and a concave Ni coated Au. The fabricated swimmers were then propelled by either a rotating magnetic field or ultrasound field. They first applied acoustic standing waves using a piezoelectric transducer to move the swimmer at the frequency of 618 kHz, followed by a rotating magnetic field. The speed of the swimmer in the case of using the acoustic field and magnetic field respectively was controlled by the ultrasound voltage and magnetic frequency. It is depicted that the swimmer's velocity increases by applying higher voltage (amplitude) so that a maximum velocity of around 20 $\mu\text{m/s}$ was obtained. Similarly, increasing the magnetic frequency resulted in faster movement of the swimmer of the maximum velocity of around 15 $\mu\text{m/s}$ at $f=200$ Hz. They also compared the performance of the swimmer once made of a nanorod, nano spring, and a combination of them, which was concluded that nano spring is faster under magnetic field whereas the hybrid swimmer has better performance under acoustic actuation field. Based on their experiments in various liquids, both swimmer's magnetic and ultrasound velocities diminished in order in seawater, cell culture medium, serum, and blood.

In another study, Ahmed et al [23] investigated the performance of a nano swimmer under the acoustic field. The swimmer with the length of around 20 μm and 0.5 μm was fabricated by multistep electrodeposition so that a bimetallic head was attached to a flagellum. They used a PDMS chamber in the vicinity of a piezo transducer both mounted on a piece of glass. In this study, they characterized the performance of the swimmer by changing the voltage and acoustic frequency, so that the higher the voltage resulted in higher velocities while at an optimum frequency (91 kHz) the highest velocity was obtained at around 60 $\mu\text{m/s}$.

Xu et al [90] fabricated iron oxide-coated *Spirulina* cells as a bio template micro helix. The setup used consists of a PDMS channel bounded on a piece of glass with a mounted piezo transducer underneath. Employing a rotating magnetic field of 5mT utilizing triaxial Helmholtz coils, combining with the acoustic levitation with a frequency of 4.8 kHz and amplitude of 300 Vp-p, the authors claimed how the lateral drifting is reduced. Moreover, the behavior of the swimmer in terms of drift angle was discussed based on changing the magnetic frequencies.

1.2 Modeling, fabrication, and propulsion overview and novelties

In this thesis, we have mainly focused on bilayer and sandwich noncrystalline micro helices. To this end, we first came up with a new sacrificial layer, i.e. E-beam evaporated chromium, with an etchant with high selectivity relative to the other main nanomembranes. The sandwich helical ribbon, which serves as a micro swimming robot, contains a ferromagnetic thin film (i.e. nickel layer) covered by two thin layers of silicon nitride with various initial stress inside; low-frequency silicon nitride (LF SiN_x) and high-frequency silicon nitride (HF SiN_x) with compressive and tensile initial stresses, respectively. Silicon nitride is a suitable material with impressive properties such as biocompatibility [74], stress controllability [72], suitable oxidation and corrosion resistivity together with thermal and chemical stabilization [91, 92]. Since nickel is believed to be toxic for the bio-environment [8] while susceptible to humid environments in terms of oxidation [25], exploiting a sandwich microswimmer with nitride cover layers makes it possible to enhance the performance of the swimmer in bio-applications. Moreover, the strain mismatch inside of the layers which are on the order of around 0.01 allows for controlling the dimension of the helix merely by changing the layer thickness [93]. This microswimmer is self-assembly fabricated just based on a magnetic helix. This eliminates the need for a magnetic head, leading to more suitable geometric symmetry and distribution of the weight; therefore, no additional control is required to keep the swimmer straight and aligned with the horizontal axis of the chamber [94]. In this project, our group has strived to fabricate a microswimmer by considering the ordinary materials and equipment in the cleanroom. For this reason, nanomembranes are noncrystalline materials that can be readily fabricated by PVD and PECVD. Since the structure is fully amorphous with uniformly distributed mechanical properties, we had to consider some factors to induce it to roll up in a desirable direction to obtain chirality. To this end, two different methods were put forward: a) creating grating patterns to determine the rolling direction, b) the geometry effect on producing micro helical ribbons.

The conversion between strain-induced nanomembranes to microswimmers has been modeled by COMSOL Multiphysics V5.6. Considering large deformation in the structure by implementing the geometric nonlinearity, we assumed the structure to be fully elastic and

isotropic to be solved by the structural mechanics module as a 3D multilayer structure. To simulate the detachment of the structure from the substrate after sacrificial layer etching, we mimicked the behavior of the real releasing coming out of our experiments. The structure is released isotropically from all edges by implementing moving boundary conditions. Then, after having almost all of the sacrificial layer removed, the structure which is rolled up alongside the long edge remains on the substrate for a while because of capillary force. After a while, due to energy minimization, at specific aspect ratios, it starts rolling about a diagonal line with gradually moving through the length until the structure is fully released. We first validated our results by comparing the diameter obtained from perfectly scrolled-up nanomembranes. After that, to ensure that the molding is reliable, we compared the results of helical structure properties (e.g. diameter, and pitch) by our fabricated helices.

The required torque for rotating the swimmer has been prepared by Helmholtz coils setup that provides an mT-scale magnetic field. The swimming is characterized in both a centimeter PDMS reservoir and an mm-scale cylindrical channel. In-channel experiments show that the swimmer tends to swim near wall boundaries, just like its counterparts. In the reservoir, also, the swimmer is observed to exhibit a lateral drift alongside its propulsion in the swimming direction. In addition to the magnetic field, in another bunch of experiments, acoustic actuation force using a piezoelectric transducer mounted on a piece of microscope slide next to the square PDMS reservoir is also been simultaneously exerted to the swimmer to observe the effect of which on both drifting and swimming velocities. The experiments demonstrate that at low acoustic frequency, the swimming velocity of the swimmer improves.

2 METHODOLOGY

This section presents the whole process of fabrication, including the devices used and the problems that had to be addressed, and afterward the modeling and simulation through elucidating the reliability of the model by comparing the results with some experimental data. In the end, also, the design of the setup used for the swimming experiments is elaborated.

2.1 Fabrication process

Since in fabricating micro/nanoscale structures even small contamination negatively affects the final obtained results, an extremely clean environment is required to carry out such experiments. Fortunately, this has been conceivable thanks to the state-of-the-art cleanroom laboratories with different classes which almost provide a particle-free environment because of robust ventilation systems in an isolated area from the other parts of the building. For this reason, all of our fabrication processes were performed in a well-equipped cleanroom at SUNUM at Sabanci University. To this end, we took advantage of a wide variety of micro/nanofabrication processes, including lithography, physical and chemical thin film depositions, spin coating, wet/dry etching, and topography, to make our designs practical.

2.1.1 Microfabrication procedure

In the thesis, two main techniques of microfabrication of self-assembled micro-helical ribbons have been examined and discussed: a) geometry modifications and b) grating method. The method of fabrication in both methods is the same to a large extent with two additional steps in the second method. Moreover, to shift from bilayer to sandwich nanoribbons, an excess step of deposition is required as well. For this reason, in the following, we will go through the fabrication of grating sandwich structures which cover the other phases of the fabrication as well, so that wherever required, the differences will be explained.

Schematically shown in Fig. 2.1., is a complete version of the fabrication process flow. In this figure, we categorized the fabrication process into 7 steps, and each step will be explained in detail in the following subsections. Similar to any other bottom-up/top-down microfabrication techniques, we were to deposit and growth the nanomembrane on a fairly thick substrate. In our cases, the substrate was chosen to be a 4-inch p-doped single crystal silicon wafer (100) with a thickness of $500 \pm 10 \mu\text{m}$. Yet, in some cases, another substrate (i.e., thermally grown silicon oxide on silicon wafers) was also utilized to provide a cleaner surface.

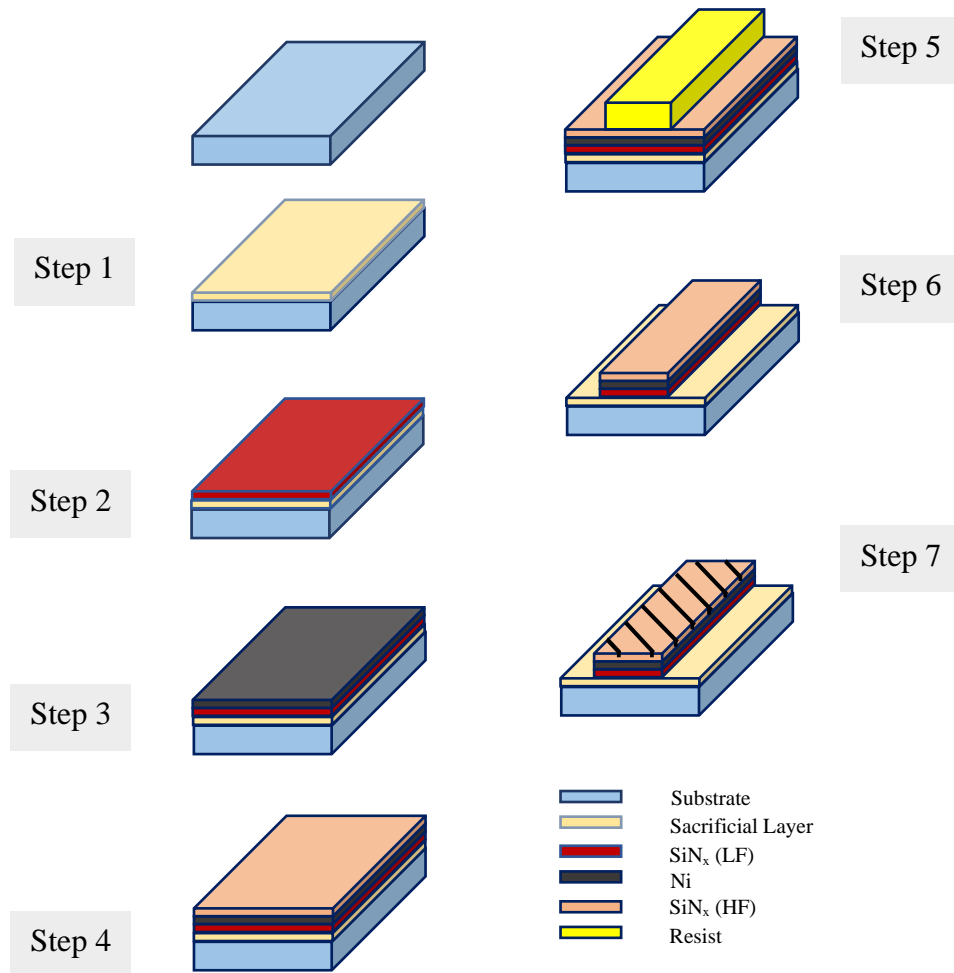


Fig. 2.1. Process flow of fabricating self-rolled up microstructures

2.1.1.1 Step 1: Sacrificial layer deposition

The sacrificial layer, generally, is an interlayer between the nanomembrane and the main substrate. Once it is etched away, the nanomembrane detaches from the substrate. This can result in different configurations like beam-type electrostatically actuation sensors and actuators. In our case, however, it brings about the releasing stresses inside the nanomembrane, leading to rolled-up 3D structures like helices. The selection of a suitable sacrificial layer, however, is of significance since it might affect the final result considerably. For instance, in sandwich structures in which different materials are used, if the etchant does not have a high selectivity to the other layers but sacrificial layer, the other nanomembranes are likely to be removed completely or partially by the etchant. This, for sure, leads to having a completely different final shape which may not be desirable.

In this thesis we used a wide range of sacrificial layers (i.e. Al, Ni, SiO₂, PMMA, and photoresist), among which, chromium has been selected because of six main reasons: 1) being a prevalent material in the cleanroom, 2) having high selectivity to the other layers at ambient temperatures, 3) being easy to fabricate, and 4) having roughly fast etching rate at ambient temperature (around 400nm/min in no diluted etchants), 5) being less hazardous than other acids like Hydrofluoric acid, and 6) being resistive to high temperatures (e.g. 300 °C in plasma-enhanced vapor deposition (PECVD) method melts the resists). To fabricate a thin layer of the sacrificial layer of around 100nm, the physical vapor deposition (PVD) method was utilized. In the PVD device (shown in Fig. 2.2., which is a Torr Evaporator machine), first, the sample, which has already been stuck to the main substrate by a holder and some piece of Kapton tapes, is put into the device. Putting a tungsten crucible with chromium pellets inside to the rotating pockets of the device, we press the vacuum bottom to reach a high vacuum (less than 8e-6 mTorr) by a turbomolecular pump. Having the vacuum reached, a bombardment of electrons emanated from a hot filament and directed by a magnetic field towards the center of the crucible is started. This electron bombardment causes the chromium to be melted and evaporated, so that after a while (because of the high vacuum which provides a high mean-free path) the evaporated metal is settled on everywhere inside the chamber including our main substrate. This method is called electron beam PVD or E-Beam PVD.

The important factors of the PVD method are the amount of vacuum which is controlled by a pressure gauge, and also the deposition rate which is measured by checking the natural frequency variations of a piece of quartz, based on the mass of the nickel deposited on the surface of that. In our case, the chromium was deposited at a vacuum of $5e-6$ mTorr, and a deposition rate of $2.5 \text{ \AA}/\text{Sec}$. The sample before and after PVD of chromium is depicted in Fig. 2.2.

To measure the thickness of the deposited chromium, a probe measurement method using a profilometry device (KLA Tencor Surface Profiler) was carried out. In this device, based on the frequency and speed of the microprobe, a bunch of height measurements is performed. Finally, using an interface, the profile of the surface is given. This process was carried out based on the height differences of non-deposited and deposited areas shown in Fig. 2.4. As demonstrated in this figure, after leveling and analyzing the profile, the step height (StepHt) was obtained at around 100 nm which was favorable.

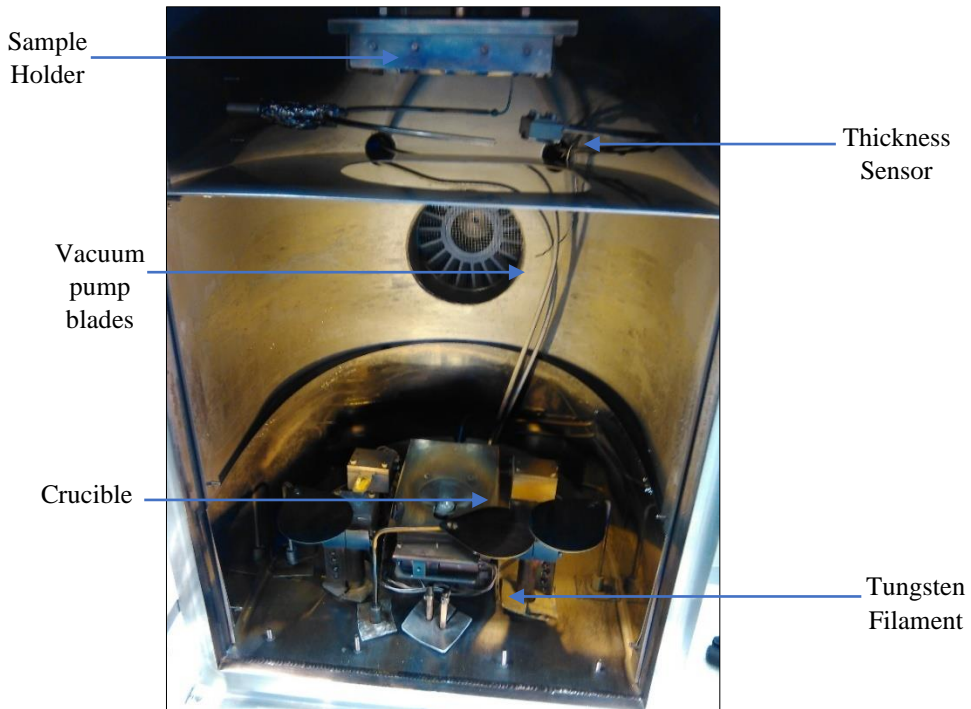


Fig. 2.2. Inside view of the PVD device used

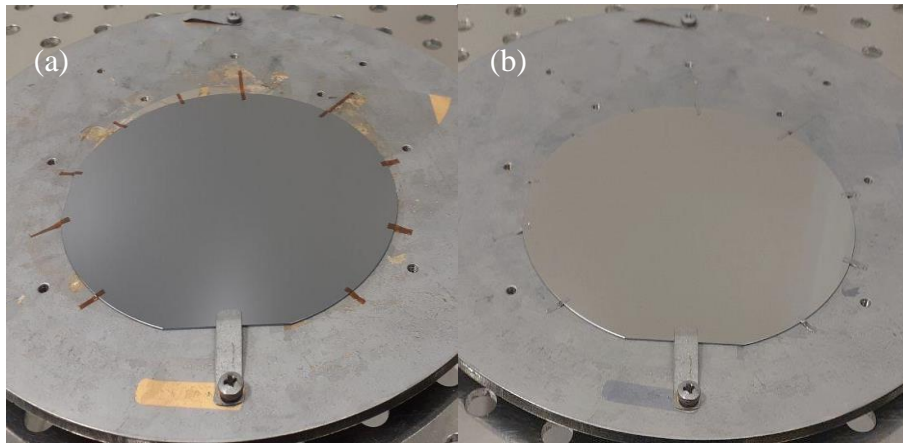


Fig. 2.3. The sample before (a) and after (b) chromium deposition

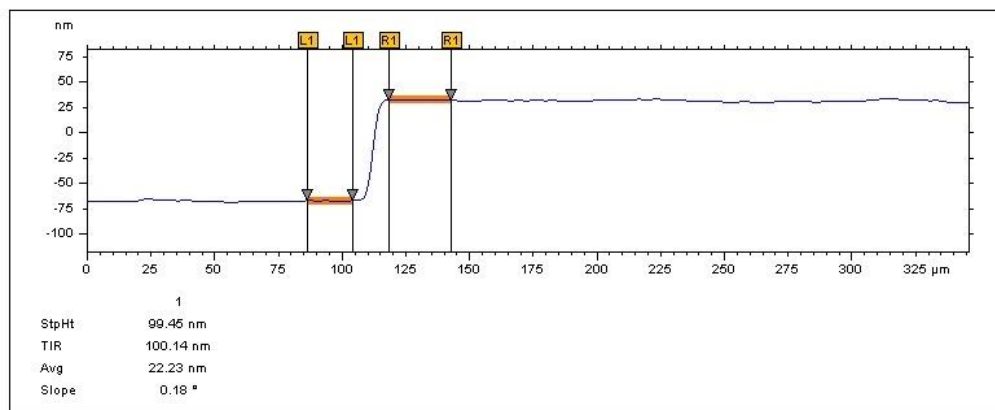


Fig. 2.4. A part of the Surface profile of chromium deposited wafer

2.1.1.2 Step 2: Low frequency (LF) silicon nitride deposition

To cover the core layer of the sandwich structure, we used silicon nitride thin films due to their unique properties mentioned in chapter 1. PECVD is a method that can produce a thin layer of dielectrics like silicon nitride, and silicon oxide, or semiconductors like amorphous silicon (a-Si). Thanks to the plasma and an electrical field, one is able to produce an amorphous thin film layer at low temperatures. However, lots of parameters influence the mechanical, and optical properties of the thin film, including power, gas mixtures, and their flow rate, pressure, frequency, and plate temperature. For instance, in silicon nitride deposition, having all parameters fixed except for the frequency, the film could have compressive or tensile stress inside, respectively for low frequency and high-frequency processes. This is attributed to the other subsequent parameters (e.g. ion bombardment effect)

[95]. Accordingly, the recipe used for the process plays an indispensable role in defining the final quality of the film.

In this thesis, we used PECVD (OXFORD Plasma Pro100) device by employing a constant recipe that was recommended by the manufacturer. Therefore, we did not go through the effects of changing parameters on the final quality of the films which was far from the scope of this thesis. The recipe mentioned in Table 2.1. was used to deposit a couple of tens of nanometers of the thin film on top of the sacrificial layer. These parameters then give a deposition rate of around 8-10 nm/min (based on the conditions of the main chamber) which was measured by both profilometry and Ellipsometry devices.

Table 2.1. PECVD Recipe for LF

Temperature	Power	Pressure	Frequency	5%SiH₄/N₂	NH₃	N₂
300 [°C]	20 [W]	650 [mTorr]	380 [kHz]	400 [sccm]	20 [sccm]	600 [sccm]

After deposition of 160nm on top of the sacrificial layer, the sample had the color shown in Fig. 2.5. It is noted that the uniformity of the thin film layer depends on the shape symmetry and also the heat distribution. That is, the reason why the whole wafer seems more uniform than the quarter shape is the symmetricity of the wafer resulting in smother distribution of thickness through the surface. It is worth noting that since the fixture of the PECVD machine is not designed for wafer slices, we have to stick them on a dummy wafer with Kapton tape. The key factor here is that the heat distribution would be nonuniform because of the intermediate wafer used. For this reason, it is highly recommended to increase the preheating time from 2 minutes to 10 minutes whenever using wafer slices on dummy wafers in order to have a perfect heat transfer.

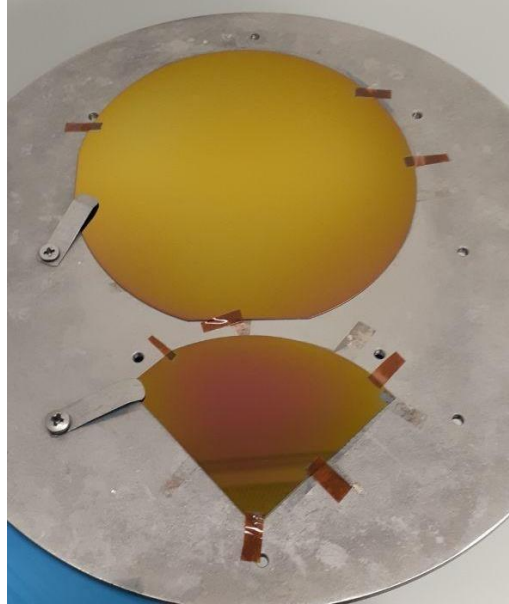


Fig. 2.5. Sample with 160nm LF SiN_x deposited on the sacrificial layer

One factor that is of importance in our designs is understanding the amount of stress inside the thin films. Since the stress varies based on different recipes, and even for the same recipes in different devices, measuring the stress is beneficial to control the final dimensions of the microswimmer. To this end, we deposited a layer of around 160 nm LF SiN_x on bare silicon, and used 3-point support (a standard method of stress measuring as shown in Fig. 2.6), whereby the stress inside the film was measured by the profilometry device.

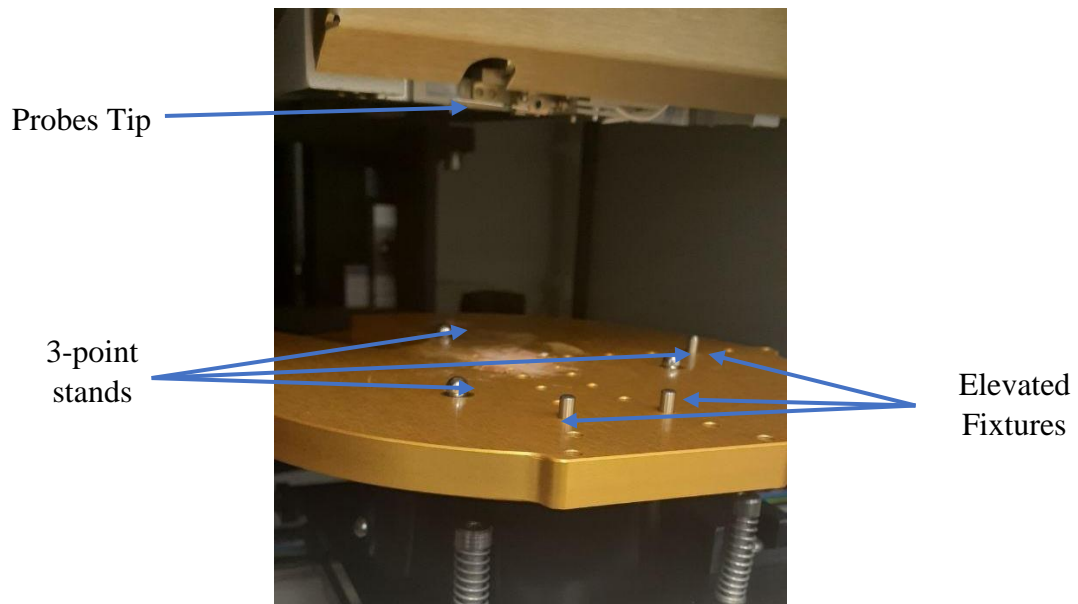
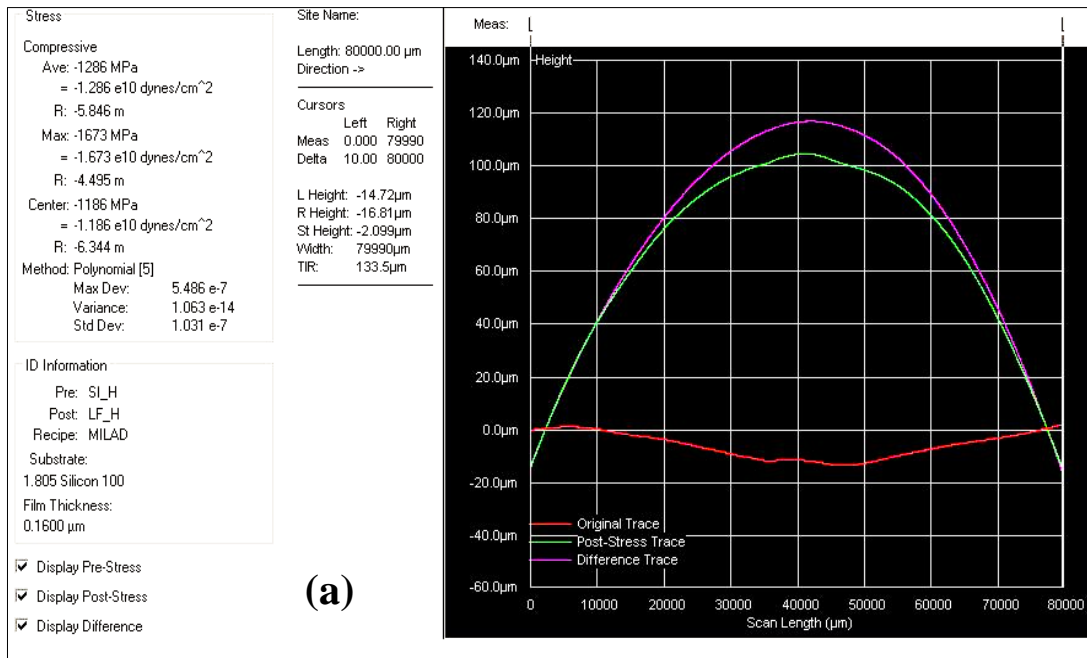


Fig. 2.6. Profilometry configuration for measuring the stress

The tip of the machine travels on the sample through a line with a length of 80% of the diameter of the wafer, so that it collects a wide range of data points, the number of which can be varied based on the defined frequency and speed of scanning. Each of these points has unique 2D coordinates relevant to the start point of scanning. By a 5th order polynomial curve fitting (recommended by the user manual of the device), a curve is obtained with an approximated radius of curvature. Now, having the radii of curvatures of the sample before and after the deposition, the stress can be calculated based on the Stoney formula mentioned below [97]:

$$\sigma = \frac{E_s}{6(1 - \nu_s)} \left(\frac{h_s^2}{h_f} \right) \left(\frac{1}{R_f} - \frac{1}{R_s} \right), \quad (2 - 1)$$

in which, E_s , ν_s , h_s , and R_s stand for substrate elastic modulus, Poison’s ratio, thickness, and radius of curvature, while h_f and R_f represent film thickness and radius of curvature, respectively. Based on this formula, the interface of the profilometry device analyzes the data and gives the amount of stress inside the film.



(a)

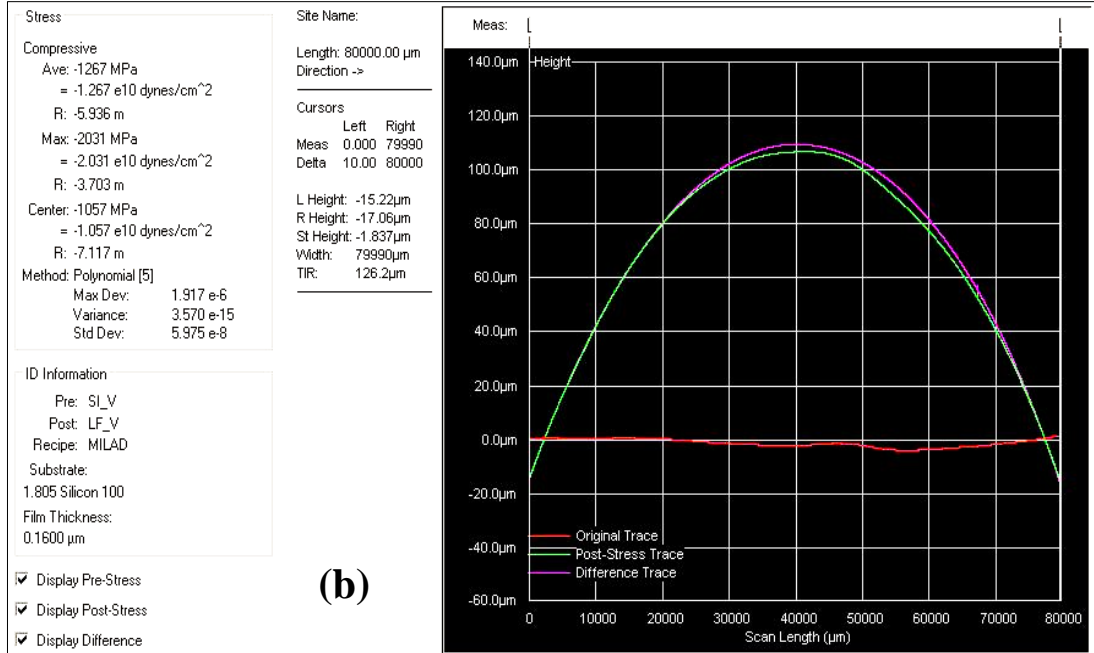


Fig. 2.7. Stress Measurement by profilometry: LF silicon nitride with a thickness of 160 nm: a) parallel, and b) orthogonal

For instance, as depicted in Fig. 2.7., the average amount of stress was achieved at -1286 MPa which shows that the low-frequency silicon nitride has compressive stress inside. Since silicon nitride is assumed to be amorphous with isotopically distributed mechanical properties, we expect to achieve the same amount of stress in other directions. For this reason, in addition to the stress measurement shown in Fig. 2.7. (a), we measured the stress in an orthogonal direction as well, which resulted in the stress of -1267 MPa as depicted in Fig. 2.7. (b). This trivial difference is acceptable due to various reasons like edge effects of non-perfectly circular wafers that can result in thickness variations. Also, some other factors can influence the distribution of stress through the sample [98-100].

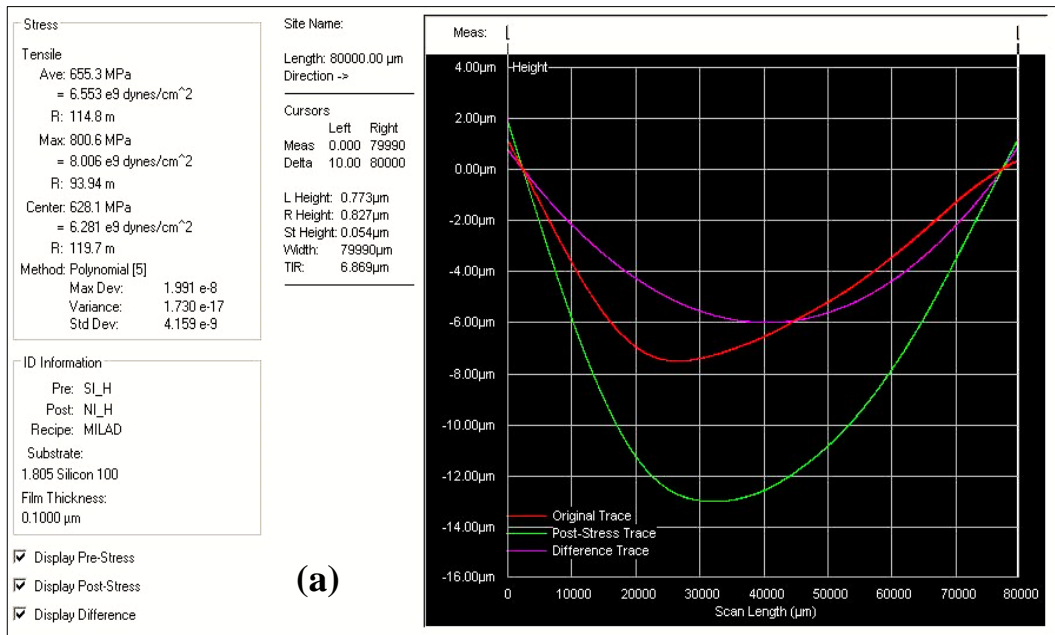
2.1.1.3 Step 3: Nickel deposition

This thesis has aimed to create microswimming robots which can be driven by magnetic fields. For this reason, ferromagnetic materials are the best options to perform this mission. Here, we used nickel thin film due to its unique physical properties [101, 102]. The nickel thin film was deposited by E-beam PVD at a vacuum of $5e-6$ mTorr and deposition rate of $2-3 \text{ \AA. min}^{-1}$, resulted in 50 nm of thickness shown in Fig. 2.8.



Fig. 2.8. Nickel thin film deposited by E-beam PVD on LF Silicon nitride

Again, the stress inside the thin film was measured by the profilometry device which is on average around 646.25 MPa tensile as derived from parts (a) and (b) of Fig. 2.9.



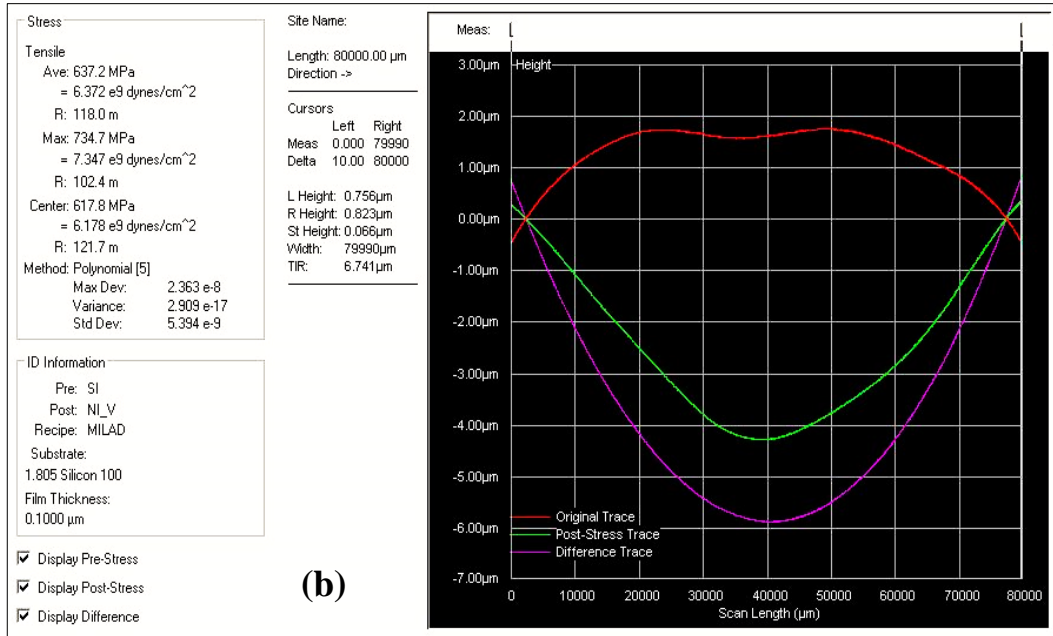


Fig. 2.9. Stress measurement of nickel: a) parallel to the flat edge of the silicon substrate, b) orthogonal to the flat edge

It is worth mentioning that for bilayer nanomembranes, this step is omitted so that just two layers of silicon nitrides with opposite stresses were deposited.

2.1.1.4 Step 4: High frequency (HF) silicon nitride deposition

The processes of fabrication of this step are exactly the same as what was mentioned in 2.1.1.2 for LF SiN_x with the difference that in HF SiN_x deposition, the frequency was set to 13.56 MHz. The thickness measurement was carried out by means of J.A Woollam Ellipsometer device. This device used an optical technique in order to measure the optical and mechanical properties of dielectric materials like silicon nitride. It consists of a light source that shines a light or laser beam on the sample with different angles and measures the polarization after reflection from the surface. Using a standard model (continuing amplitude component (Psi) and phase difference (Delta) versus wavelength) for different materials, and compare the results by fitting the thickness and roughness automatically together with other parameters, the approximate thickness with a mean squared error (MSE) is obtained. For sure, the lower the MSE, the more accurate the results. However, in our case, it is recommended that for MSE less than 20, the results enjoy high reliability. The measurement report given in Fig. 2.10. represents the perfect curve fitting with an MSE of 9 that gives a thickness of around 364 nm. As the time of deposition was 24 minutes, the deposition rate was understood to be around 15

nm/min in case the main chamber is devoid of contamination after cleaning it by a special recipe.

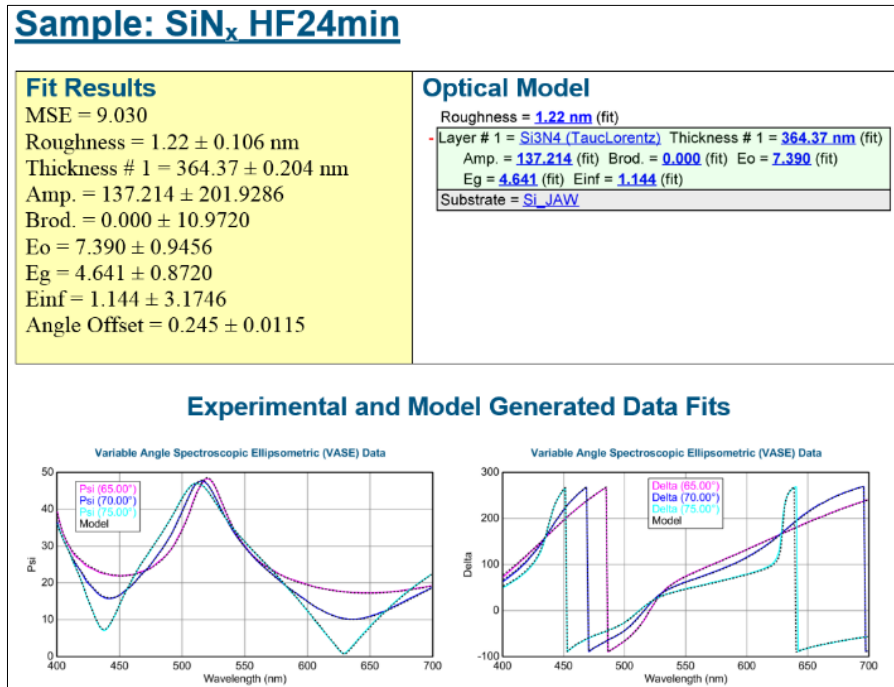
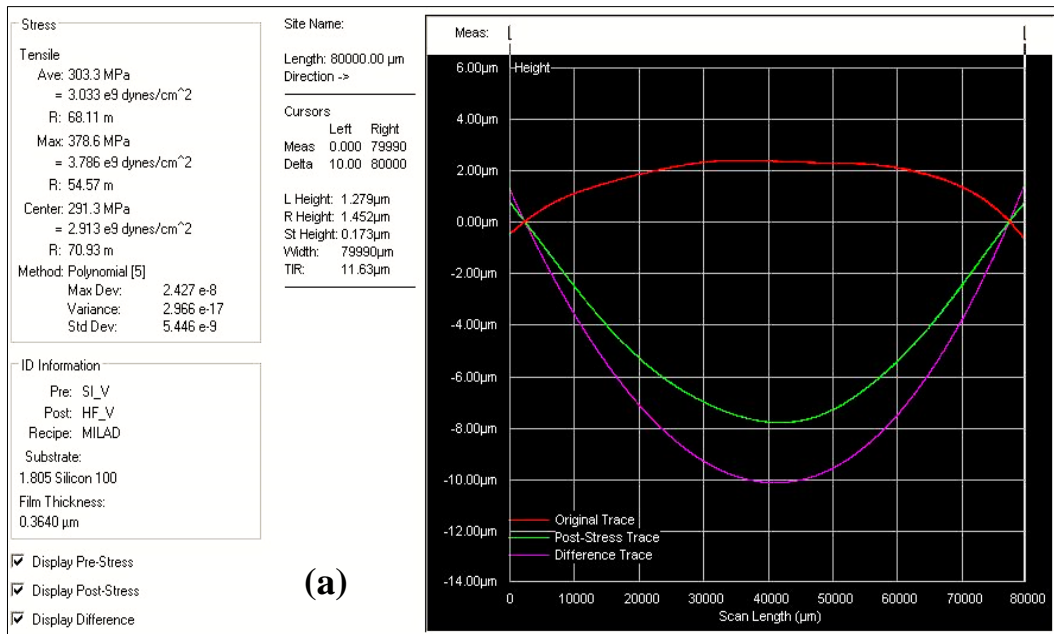


Fig. 2.10. Ellipsometry results of a 24-minute deposited SiN_x (HF)

Now, having the thickness, by using the profilometry device, the stress inside the LF layer was measured to be around 304.5 MPa on average (depicted in Fig. 2.11).



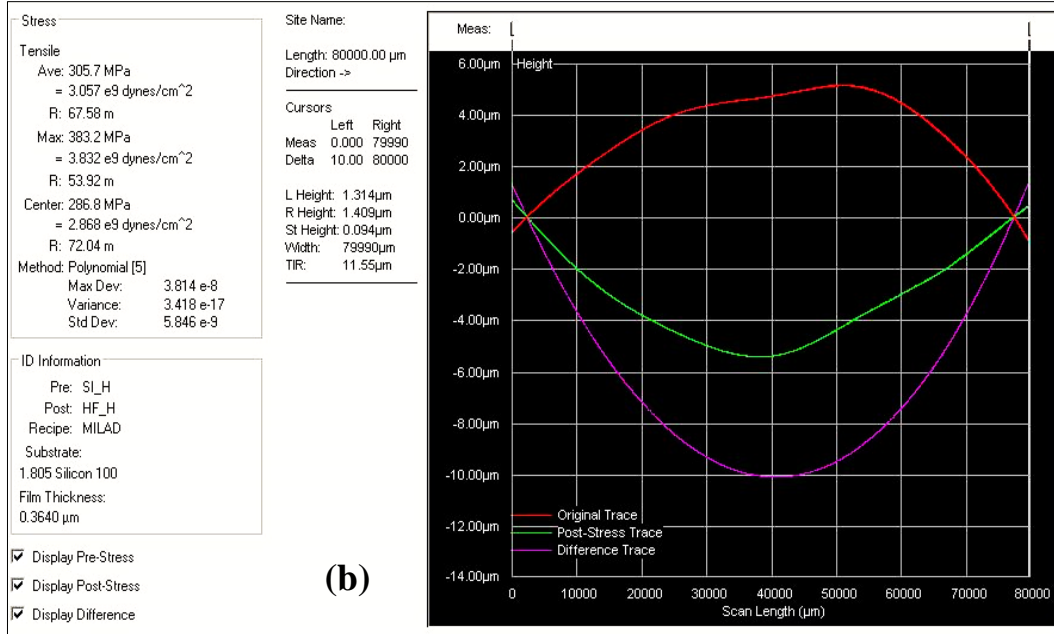


Fig. 2.11. Stress measurement of SiN_x (HF): a) parallel to the edge of the wafer, and b) orthogonal to the edge

2.1.1.5 Step 4: Lithography

After the deposition of all layers, the 2D patterns are to be transferred to the layers through a top-down process. This is called lithography which in our case was done by two different methods: 1) electron beam lithography (EBL): which uses electron beams emitted from an electron source (e.g. tungsten filament, or filed emission guns) and accelerated, demagnified, and moved through the sample by an anode, a set of electromagnetic condenser lenses, and scanning coils, respectively. When the accelerated electron beam hits a substrate, it interacts with the structural elements of that. In the case of using a polymer like Poly (methyl methacrylate) (PMMA), the chemical bonds are weakened so that in contact with a developer like (Methyl isobutyl ketone) MIBK, those exposed regions will be removed, resulting in 2D patterns created through the PMMA. 2) Photolithography: the mechanism of creating 2D patterns is exactly the same as EBL with some differences. For instance, instead of the electron, UV light is shone through a mask and after passing through the open regions of the mask it reaches the sample which is covered by a photoresist (PR) material. After putting the sample into a developer, those regions that have been susceptible to the UV light will be removed. In some special cases, also, the chemical bonds of the exposed regions can be

strengthened and not remove after developing based on the PR material, lithography recipe, and post-processing procedures applied. This is called reversal lithography which is performed using a negative PR or PMMA. However, the majority of our experiments were focused on photolithography by positive PR. Hence, in the rest, we will just go through this process and describe the other processes used by EBL.

2.1.1.5.1 Mask

For the sake of producing microswimmers with the best performance, a wide range of designs was prepared by Layout Editor software either for EBL or photolithography. Since for most of the structures, the feature sizes were more than 50 μm , we used high-resolution printed masks for photolithography. However, for some shapes with feature sizes of a couple of nanometers, we had to use EBL. The masks were prepared as dark fields or light fields based on their applications. After more than 40 experiments with different masks containing various designs, in the end, for the final results which required more than 36 systematic experiments, we used a batch fabrication process to reduce the time and cost of production. For this reason, two main masks were produced to cover both techniques of fabrications that were utilized. In this step, the mask shown in Fig. 2.12. contains a set of rectangular ribbons that are arranged in order to cover different angles. The ribbons have areas of around $105 \times 1050 \mu\text{m}^2$, $120 \times 1050 \mu\text{m}^2$, $145 \times 1050 \mu\text{m}^2$. However, here in this experiment we just report the results coming from the second sets of rectangles. The repeatability of the experiment was checked by having three of each series in every experiment. The mask area was designed to be as much far as possible from the edges of the wafer at which the thickness is nonuniform because of edge effects created in PECVD and also in PR spin coating. The objective of the plus sign in a square at the left-hand side of the mask is to prepare a mask aligning process for the subsequent photolithography with the other masks that need to be perfectly positioned. The surrounding circle with two edges exactly represents the geometry of the wafers used.

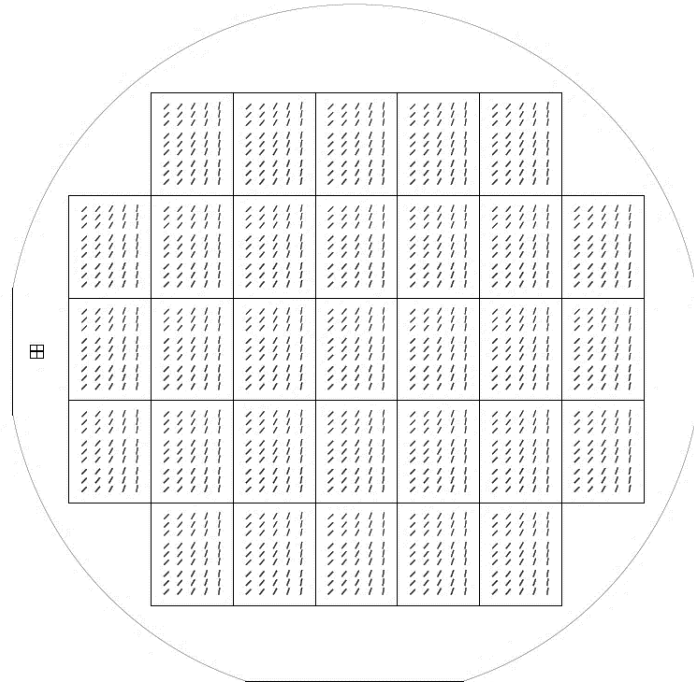


Fig. 2.12. Final mask designed for batch fabrication

2.1.1.5.2 Photolithography process

Since sensible to light, the processes of the lithography have to be carried out in a room in which some damaging wavelengths are filtered. For this reason, the process is performed in a room with yellow fluorescent light tubes that filter light with wavelengths less than 500 nm [103]. This room is the cleanest section of the cleanroom so that providing a neat environment for the resists which are very sensitive to dust and other contaminations. The process of lithography generally consists of three main steps that will be explained below:

Spin coating of PR: As mentioned above, cleanliness is a key parameter in the lithography process. Hence, before starting the process, one has to make sure that the surface is full free of any contaminations, and if necessary, dehydrate the sample in an oven or on a hot plate for a couple of minutes at around 120 °C. Afterward, the PR is poured on the sample by a cleaned and new plastic pipette very smoothly such that no bubbles remain on the sample. It is noted that in case there are any bobble or contamination particles on the substrate, we see that the PR is not coated uniformly on the sample which can reduce the resolution of the final shape of the 2D patterns. The PR used for this project was Photoresist 5214E which can provide a

thin film layer of different thicknesses based on the recipe used. For this reason, regarding the datasheet of this resist, to have a 1.4 μm thick resist, a one-step recipe mentioned in Table 2.2 was used. After that, the sample needs to rest for 2 minutes in order for stabilization, followed by keeping on a hot plate at 110°C for 60 seconds to have the solvent inside the PR evaporated moderately. Then, it has to be put somewhere clean with a dark cover (e.g. a petri dish surrounded by aluminum foil) to let the sample cool down slowly at ambient temperature. The rainbow-like color of coated PR shown in Fig. 2.13., is due to newton waves so that if one rotates the sample the color may change as well.

Table 2.2. PR spin coating recipe

Time	Acceleration	Speed
60 [s]	450 [rpm^2]	4000 [rpm]



Fig. 2.13. Wafer coated with 1.4 μm PR

In the case of using EBL, we coated AR-P 672.06 PMMA based on the three-step recipe given in Table 2.3. Then, the sample should be put on a hot plate for around 60 seconds at 175 °C. This led to reaching a thickness of 350 nm.

Table 2.3. PMMA Spin Coating Recipe

	Time	Acceleration	Speed
Step1	4 [s]	450 [rpm^2]	500 [rpm]
Step 2	50 [s]	450 [rpm^2]	4000 [rpm]
Step 3	5 [s]	450 [rpm^2]	0 [rpm]

- Lithography process: Having the sample PR spin-coated, it is ready for the lithography process. To this end, the mask shown in Fig. 2.12., was located in the mask holder depicted in Fig. 2.14., of the “Midas Mask Aligner MDA-60 MS” device, so that it kept on that by pressing vacuum bottom. Now, the prepared sample is put on the sample holder of the device so that the cut edge of the wafer exactly aligns with the same part on the sample holder. This is useful as a pre-alignment method for the subsequent processes in which multi masks are to be used and aligned with respect to each other. Again, a vacuum is served to keep the sample so that no movement would occur. It should be noted that in lithography, accuracy is the key point since we are talking about a couple of micron resolutions. Hence, even a very tiny displacement of the sample results in a big error in the subsequent processes. The most indispensable part is the recipe that one may use. This recipe contains lots of parameters varying with respect to the different PR, substrate, and profile resolutions. However, the best recipe that worked well in our case is tabulated in Table 2.4.

Table 2.4. Photolithography Exposure Parameters

Exposure Time	Energy	Mask Thickness	Sample Thickness	PR Thickness
6 [s]	120 [mJ]	2.36 [mm]	500 [μm]	1 [μm]

For the EBL also, we used Raith/Vistec EBPG5000+ES EBL system which provides 100 kV energy, and the electric flux density used for patterning of our structures was set to $325 \mu\text{C}.\text{cm}^2$.

- Developing: To remove the electron or UV-light exposed regions, the sample should experience a developing process. However, right after the exposure process, in order for stabilization, the sample should have rested for around one to two minutes somewhere clean. Then it was immersed in a developer (i.e. AZ 726 MIF developer). The time of development can vary based on the freshness of the PR. For instance, in our case in which we used a non-expired PR, it took around 1 minute to have the exposed PR removed. This time is of importance in order to not have undercutting and missing the resolution. During the developing process, a very smooth shaking of the

petri dish would be useful. After the developing process, the sample was required to be put inside deionized water (DI-Water) for 2 minutes. After that, it had to be dried using nitrogen gas very gently. In the case of using PMMA for EBL, the developing process falls into three steps: 1) 60 seconds immersing in a 3(IPA):1(MIBK) solution, 2) 10 seconds in 1(IPA):1(MIBK), and 3) resting in IPA for 1 minute.

All the processes mentioned above ended up with a sample with a PR mask through which patterns were created. Now, the patterns had to be transferred to the whole layers which are discussed in the subsequent section.

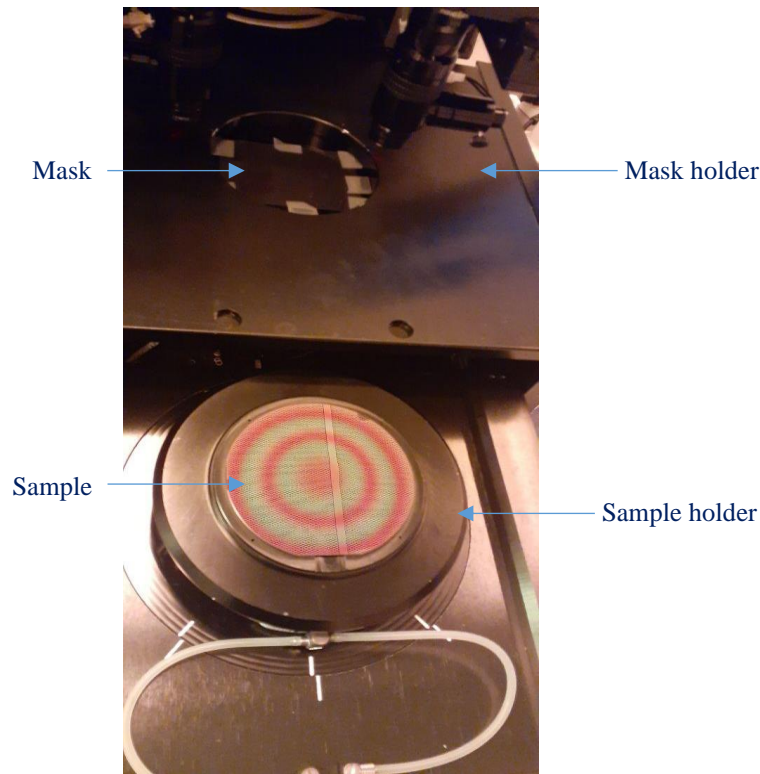


Fig. 2.14. Photolithography device

2.1.1.6 Step 5: Etching

Etching means removing material or part of it chemically or physically. In this project, we used two methods of etching processes with respect to the materials used. The first one was reactive ion etching (RIE) known as dry etching which is a plasma etching process taking

advantage of a combination of physical ion bombardment and chemical reactions. This assisted to have a directional anisotropic etching with the minimum lateral undercutting. This process depends on the dielectric or metal films, such that using some key parameters including gas types, flow rate, pressure, and power, change the performance of the process. The second etching process is chemical etching based on which the material will be dissolved once immersing or exposing to a special solvent or vapor phase of which. It is worth noting that not only the material is removed when the etching process is started, but some or a whole part of the resist mask will also be removed as well. Hence, the process of etching could be limited for some materials. For instance, metals like Ni are more resistant to the gas mixture used for etching dielectrics (e.g. silicon nitride). On the other hand, resist masks must be survived during the etching process. All the facts considered, the etching process in our fabrication was done by both RIE for Silicon nitride layers and wet etching for the nickel layer. This helped us to carry out the etching process while having the resist perfectly survived.

Generally, the recipe used for etching SiN_x in RIE machine (OXFORD Plasma Pro100) is shown in Table 2.5. In the case of using just a bilayer silicon nitride films, we put the sample into the device for less than three minutes (since the etch rate was around 5-8 nm/sec). In the case of using sandwich layers in which the nickel core is covered by two layers of silicon nitride, first, the top HF SiN_x layer was dry-etched by RIE for around 1.5 minutes, and after a wet etching process to etch the nickel layer, the bottom LF SiN_x layer was etched away by RIE at around 50 seconds. It is worth mentioning that, due to the chamber's conditions, it is highly recommended to do a process of etching each time after cleaning the chamber. However, for academic applications where the device is used repeatedly by other people, regularly cleaning the chamber would be impossible since it is a very time-consuming process. Instead, one may use another alternative; perform RIE for a limited time (e.g. 10 seconds), and measure the high differences before and after etching. This helps to understand the etch rate of the recipe at that time. However, the color-changing tracking under the microscope may be helpful.

Table 2.5. RIE Recipe for LF and HF SiN_x

Temperature	Pressure	SF_6	CHF_3
20 [°C]	10 [mTorr]	20 [sccm]	80 [sccm]

Like what mentioned above, since the used resist (especially PMMA) would not be survived if using RIE for etching nickel, we had to employ a wet etching process instead. There are a bunch of solvents that can remove nickel [104, 105]. However, we characterized some of them (diluted HCl, AL80, HNO₃, Auga regia, and FeCl₃) to see their selectivity to the resists. Most of them although work properly in etching the nickel, but there are many drawbacks with them as well. For instance, ammonia with a fairly high etch rate of nickel, peeled off the resist completely. HCl damaged the silicon nitride, and Aluminum etchant AL80 has a very low etch rate at ambient temperature. For this reason, two options remained (i.e. Auga regia and FeCl₃). Aqua regia although works, it had a very slow etch rate around 10-20 nm/min. The best and final option was FeCl₃ 85% which has a very high etch rate (a couple of microns per minute), providing perfectly sharp edges. To increase the controllability of the etching process so that to minimize undercutting, the etchant was diluted by DI-water with a rate of 1(FeCl₃ 85%):20(DI-Water). This assisted us to etch 50nm of nickel in just 10-15 seconds while having sharp edges and negligible undercutting.

Having three subsequent etching processes (i.e., RIE of HF SiN_x, wet etching of nickel, and RIE of LF SiN_x) completed, the patterns were transferred through the nanolayers, and as a result, a bunch of mesas was achieved as shown in Fig. 2.15. (c). After the etching processes, to remove the PR, hot acetone at 60 °C was used followed by rinsing in IPA and DI-Water and drying by nitrogen gas. It should be pointed out that in the case of fabrication bilayers the wet etching processes would not be required and just one step of RIE is enough.

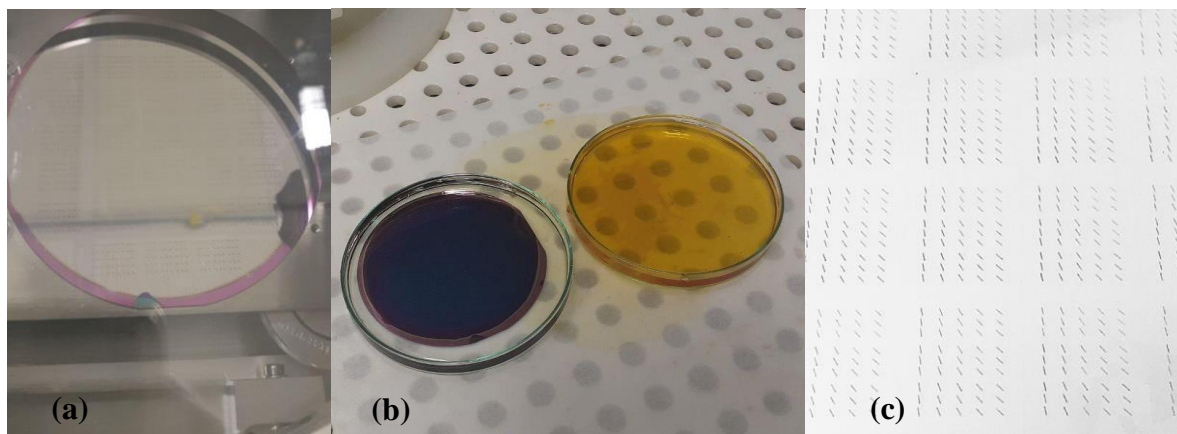


Fig. 2.15. Etching processes: a) RIE of HF, b) wet etching of Nickel, c) RIE of LF and removing PR

2.1.1.7 Step 6: Second lithography

This process is an additional technique to create grating mesas. Hence, for the first method of our fabrication which is based on thickness variation, this step was omitted. In the grating method, four main parameters should be taken into account: g (gap distance between each island), w (width of each island), H (height of islands), and θ (the angle of the patterns). These parameters are demonstrated as a schematic view in Fig. 2.16. In this project, a wide range of experiments was carried out with combinations of the following nondimensionalized parameters, in which L is the constant Length of the mesas, and T_{top} is the thickness of the top layer which is HF silicon nitride.

- g/L : 0.025, 0.05, 0.075
- w/L : 0.025, 0.1, 0.175, 0.25
- H/T_{HF} : 0.2, 0.4, 0.6

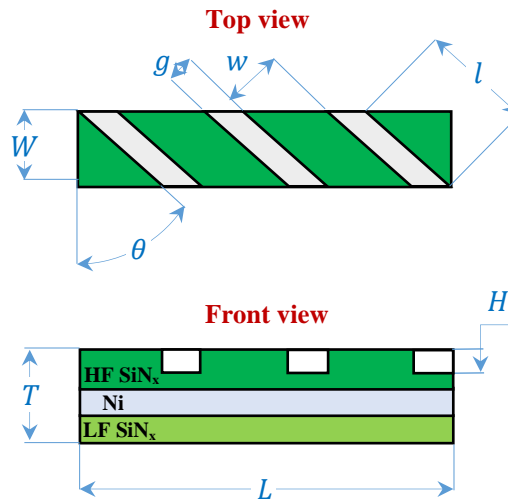


Fig. 2.16. Schematic view of grating parameters

To this end, another mask was prepared, in which three sets of each combination of g/L and w/L were used, so that it was aligned to the first patterns achieved from mask 1 by means of the cross mark. After spin coating of the PR with the same recipe shown in Table 2.2, and going through the post-processing procedure, the patterns were engraved through the PR through the photolithography process using the similar recipe mentioned in Table 2.4. After developing, the patterns were created as shown in Fig. 2.17. The blue regions show the surface of the silicon nitride that is opened to be etched away based on the defined heights (H). The next stage, as depicted in Fig. 2.18, was slicing the whole wafer by “ATV RV 129”

wafer Scriber device in order to divide the samples into three sets which needed to be etched based on H/T_{HF} ratio mentioned above.

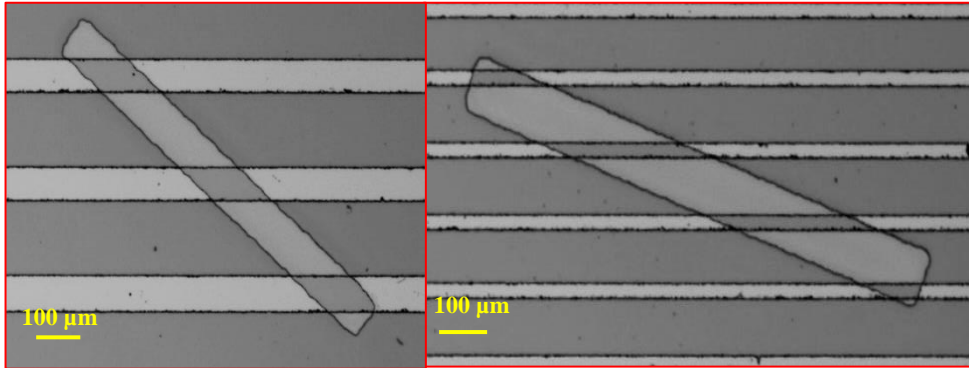


Fig. 2.17. Microscopic image of the grated pattern after photolithography

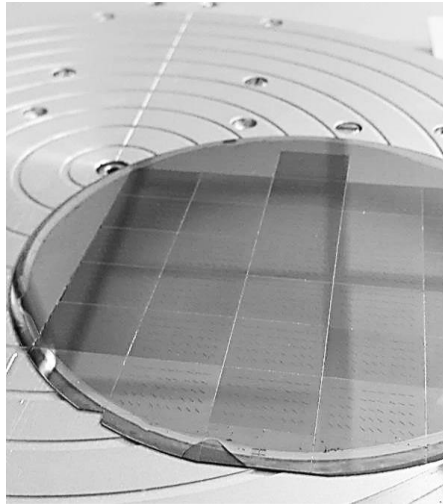


Fig. 2.18. Wafer slicing by the dicing saw

After slicing the wafer, it needs to be cleaned by the nitrogen gun in order to get rid of wafer residues on the sample. Like what was mentioned earlier, three sets of samples were prepared for one-step silicon nitride RIE (shown in Table 2.5) which gives grated mesas with three various grating heights. After RIE, the samples were put in hot acetone at 60 °C for a couple of minutes, and if required, sonication was utilized as well, together with smoothly cleaning by specific soft swabs. After that, the acetone was cleaned by IPA followed by DI-water and dried under nitrogen gas.

Having the sample ready, we just needed to etch the chromium sacrificial layer. To this end, chromium etchant Cr01 was used at ambient temperature. Here, it is worth pointing

out that although at higher temperatures the etch rate of chromium will be increased dramatically, however, we carried out the experiments at ambient temperature at which the selectivity of nickel etching is extremely low. Hence, we preferred to increase the time of the experiment in favor of surviving the core nickel shell as a magnetic layer as much as possible. Therefore, each experiment took around two and a half hours to have the ribbons with a width of 120 μm started rolling. Then, images and videos were taken from the rolled structure in real-time by optical microscope (since they become floated and hard to find them out once detaching from the substrate). it should be noted that the first method of fabrication was not an exception in this regard.

2.1.2 Problems in fabrication

What was mentioned above about the microfabrication process is just the final version of our fabrication. However, over the course of three years, many challenges in front of us needed to be addressed. Some of them were mentioned during the explanation of each process. In this section, some others are discussed and most of them were performed under the supervision of the technicians in Sabanci university nanotechnology research and application center (SUNUM). So, first, one must be certain about what he/she is doing by consulting the people in charge, and then perform the processes since some of them may be extremely hazardous, like hot acetones, PECVD recipes, RIE recipes, acids, hydroxides, perfect ventilation systems (e.g. the hydrofluoric acid is a very dangerous material in both liquid and vapor phases. So it is extremely recommended to use aprons, gloves, glasses, and shields under standard ventilation systems).

One of the main problems was the existence of pinholes generated during the PECVD of silicon nitride. These pinholes become more important to be eliminated as much as possible when dealing with nanomembranes with a thickness of less than 100 nm. In our case, pinholes, in essence, do not cause considerable effects on the structure since the size of which are usually less than a micron [106]. However, their side effects are problematic especially when trying to etch the sacrificial layer, so that once the structure is put inside the etchant, it penetrates the pinholes and starts etching from them in addition to the edges. This may change

the direction of rolling completely. For the sandwich layer, the nickel core layer was aimed to be survived as much as possible. Hence, the existence of pinholes resulted in etching the unexpected area of the nickel as well. Several methods were proposed in order to eliminate the number of pinholes, among which using very clean substrate was our priority since the other methods deal with changing the parameters of cleaning. Due to the fact, in all of our experiments, we tried to use new wafers coming from the package. We also used thermally grown silicon oxide on a silicon wafer to have a more uniform and clean substrate. In every process, we tried to run a main chamber cleaning recipe before going through our main processes.

In the cutting processes, the scratching line is created by a diamond tip. Since silicon substrate is crystalline, it prefers cutting alongside the crystal planes. Therefore, the cutting depth had to be controlled in order to ensure cutting right from the scratching lines. However, taking all the facts considered, cutting had to be performed very carefully and most of the time it resulted in a failure. Finally, we found out a very sharp edge to cut the sample on that while aligning the scratching lines right on the sharp edges. In some cases, in which the nanomembrane is not covered by a resist mask, we deliberately spin-coated a PR before the cutting process, so that the wafer particles lay on the PR, which are removed easily by solving the PR in acetone and sonication.

Since the cleanliness of the substrate is of significance, some other methods of cleaning were used, including piranha solution cleaning, hot acetone cleaning, ultrasonic cleaning, and mechanical cleaning by swaps to get rid of organic residues. These methods, however, do not guarantee a clean surface while they remain their own residue. Instead, there are some other methods known as RCA cleaning processes whereby first a thin layer of the surface is oxidized and then cleaned, resulting in a very neat surface. Sometimes, after using resists, it was hard to remove them from the surface especially if they were hard-baked. Therefore, we put the sample in RIE under oxygen plasma with fairly high power (less than 100 W) in a couple of minutes. These processes assisted us to clean the surface very accurately.

We tried a wide range of patterning to reach consistency in our results. However, drawing these patterns as they were too much (more than thousands in an experiment), it was impossible to use common drawing software like SOLIDWORKS. Instead, other vector-based

software like Layout Editor or AutoCAD had to be employed. These kinds of software do not occupy too much memory, and as a result, designing an array of patterning was possible. Using the devices like PVD for some materials was very challenging. For instance, since nickel is a magnetic material, the electromagnetic field inside the device, which is used to conduct the electron beams towards the center of the crucible, directly affects the melting process of nickel. As a result, when using new pellets, by ramping up the current something like firework happens inside the chamber resulting in nickel particle bombardment everywhere including the sample. Hence, we had to wait for an hour to have the melted nickel stabilized first. Then, by ramping up the current the process was carried out. Since the boiling point of nickel is very high, if one wants to increase the deposition rate, the nickel can be combined with the surface of the crucible and create alloys. For this reason, there is a trade-off between the deposition rate and the quality of the final products. Some suggest using graphite crucible instead of tungsten. This may improve the quality of the film, however, the graphite crucibles are likely to be broken at high temperatures due to thermal gradients. Therefore, trying and error in this process may be required in order to obtain the best results.

2.2 Modeling and simulation processes

In this section, we first go through rolled-up structures, how to model them, and comparing the results by some of our rolled-up microstructures to verify our simulation. Then, taking advantage of this method and showing energy minimization, we show how to model helical and corkscrew-like structures. In the next chapter, we will show in detail how accurate our model is by comparing the results with our own manufactured micro helical structures.

2.2.1 Rolled-up ribbons

To simulate the process of rolling, COMSOL Multiphysics V5.6. was employed to model the multilayer micro ribbons as a 3D structural solid mechanics. The rolling process and materials were assumed to be fully elastic. Then, two or three nanolayers of silicon nitride and nickel were placed on top of each other by defining them as 3D blocks. Since the structure is too

thin, inertial effects are neglected. Hence, the structure is released step by step by defining moving boundary conditions with quasi-static approach. To apply initial stress, we defined mismatch thermal expansion for each layer. The general linear governing equations in solid mechanics of COMSOL are based on the linear momentum balance according to the Newton's second law which relates the stress, strain and displacement filed as follows [107]:

$$\rho \frac{\partial^2 \mathbf{u}}{\partial t^2} = \nabla \cdot \mathbf{S} + \mathbf{F}_V, \quad (2-2)$$

$$\mathbf{S} = \mathbf{S}_{ad} + \mathbf{C} : \boldsymbol{\varepsilon}_{el}, \quad (2-3)$$

$$\boldsymbol{\varepsilon}_{el} = \boldsymbol{\varepsilon} - \boldsymbol{\varepsilon}_{inel}, \quad (2-4)$$

$$\boldsymbol{\varepsilon}_{inel} = \boldsymbol{\varepsilon}_0 + \boldsymbol{\varepsilon}_{th} + \boldsymbol{\varepsilon}_{hs} + \boldsymbol{\varepsilon}_{pl} + \boldsymbol{\varepsilon}_{cr}, \quad (2-5)$$

$$\boldsymbol{\varepsilon} = \frac{1}{2} [(\nabla \mathbf{u})^T + \nabla \mathbf{u}], \quad (2-6)$$

$$\mathbf{S}_{ad} = \mathbf{S}_0 + \mathbf{S}_{ext} + \mathbf{S}_q, \quad (2-7)$$

in which, $\mathbf{u}=[u,v,w]$ is the displacement field, ρ is the density, $\frac{\partial^2 \mathbf{u}}{\partial t^2}$ is the acceleration, $\nabla \cdot \mathbf{S}$ is Cauchy stress tensor, \mathbf{F}_V is volume force, $\boldsymbol{\varepsilon}_{el}$ is the total elastic strain, $\boldsymbol{\varepsilon}$ is the linear strain-displacement, $\boldsymbol{\varepsilon}_{inel}$ are initial and inelastic strains, $\boldsymbol{\varepsilon}_0$ is initial strain, $\boldsymbol{\varepsilon}_{th}$ is thermal strain, $\boldsymbol{\varepsilon}_{hs}$ is Hygroscopic strain, $\boldsymbol{\varepsilon}_{pl}$ is plastic strain, $\boldsymbol{\varepsilon}_{cr}$ is creep strain, \mathbf{S}_0 is initial stress tensor, \mathbf{S}_{ext} external stress tensor, \mathbf{S}_q is extra stress coming from viscous damping, and \mathbf{C} is the elasticity tensor, generally defined by the elastic modulus and the Poisson's ratio. In our case, the acceleration term is omitted as a results of stationary problem. Similarly, other terms related to body force and other stress and strain tensors are neglected, except for thermal strain tensor which is intentionally apply to the systems as follows:

$$\boldsymbol{\varepsilon}_{th} = \boldsymbol{\alpha}(T - T_{ref}), \quad (2-8)$$

where, $\boldsymbol{\alpha}$ is the thermal expansion coefficient, and T is the temperature that is defined for each layer to obtain the measured stresses. Transforming a 2D structure into a 3D helical structure is a process required large deformation. This large deformation results in mid-plane stretching, leading to geometric nonlinearity, that is to be considered in the displacement field.

For this reason, the normal equations explained in Eqs. (2-2) - (2-7) are required to be modified so that this effect is included. In COMSOL, there is an option named “include geometric nonlinearity”, after selecting it the equations are updated. To this end, the Green-Lagrange strain and the second Piola-Kirchhoff stress are utilized instead of engineering strain and stress, so that to solve the problem, COMSOL employs a total Lagrangian formulation. Considering the abovementioned modifications, the governing equations are changed as follows [108-111]:

$$0 = \nabla \cdot \mathbf{P}^T, \quad (2 - 9)$$

in which \mathbf{P} is the first Piola-Kirchhoff stress tensor, that can be obtained by using a transforming matrix (\mathbf{F}) and the second Piola-Kirchhoff stress tensor (\mathbf{S}) expressed as follows:

$$0 = \nabla \cdot (\mathbf{F}\mathbf{S}), \quad (2 - 10)$$

$$\mathbf{S} = \mathbf{C} : \boldsymbol{\varepsilon}_{el}, \quad (2 - 11)$$

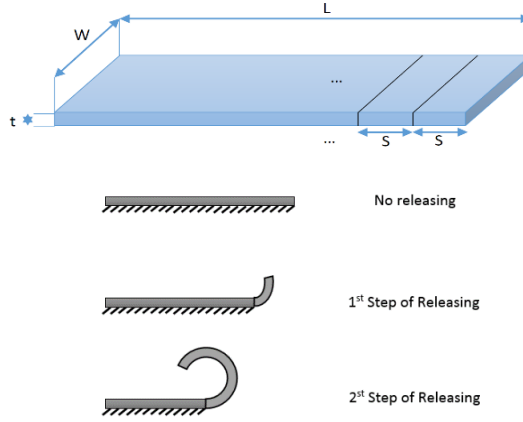
$$\boldsymbol{\varepsilon}_{el} = \boldsymbol{\varepsilon} - \boldsymbol{\varepsilon}_{th}, \quad (2 - 12)$$

$$\boldsymbol{\varepsilon} = \frac{1}{2} [(\nabla \mathbf{u})^T + \nabla \mathbf{u} + (\nabla \mathbf{u})^T \nabla \mathbf{u}], \quad (2 - 13)$$

$$\mathbf{F} = \mathbf{I} + \nabla \mathbf{u} = \mathbf{I} + \frac{\partial \mathbf{u}}{\partial \mathbf{X}} = \begin{bmatrix} 1 + \frac{\partial u}{\partial X} & \frac{\partial u}{\partial Y} & \frac{\partial u}{\partial Z} \\ \frac{\partial v}{\partial X} & 1 + \frac{\partial v}{\partial Y} & \frac{\partial v}{\partial Z} \\ \frac{\partial w}{\partial X} & \frac{\partial w}{\partial Y} & 1 + \frac{\partial w}{\partial Z} \end{bmatrix}, \quad (2 - 14)$$

As schematically depicted in Fig. 2.19., the microstructure is initially confined before the etching process of the sacrificial layer started. Afterward, this layer is released incrementally by defining a set of sectioned boundary conditions underneath the structure, mimicking the etching process. By defining strain mismatches between nanolayers, once one segment is released, the problem is solved stationary, resulting in the rolling of that segment. Then, the solution and physics properties of this section are used as the initial condition for the next step, in which another segment is detached. This process loop continues until the rolled-up configuration is obtained. Finally, the curvature or diameter of the rolled-up nanomembrane is measured. To induce the strain mismatch inside the layers, as previously

mentioned, we applied thermal expansion since it provides a fairly better approximation of stress distribution either in-plane or through-thickness of the nanomembranes. Another reason was that the COMSOL fail to give accurate stored elastic energy when using stress, and as we needed to calculate the energy stored to prove energy minimization, the thermal expansion method was the best choice.



$$\mathbf{u} = \mathbf{0} \text{ for } L - n$$

where $n = 0, S, 2S, \dots$,

Fig. 2.19. Schematic view of releasing the structures from the substrate

Before going through the method in detail, it should be noted that the curvature and related stress shown in the previous section just give stress information about the surface of the structure. However, we know that in-plane stress is not uniformly distributed through thickness [112-114], meaning that, there is a stress gradient through thickness that needs to be taken into account. However, this requires real-time curvature measurement which is demanding work requiring special measurement equipment in both PECVD and PVD devices. For this reason, we used another alternative in which the sample curvature at the top is measured, then using RIE and measuring thickness by Ellipsometry followed by measuring the curvature by profilometry, the stress can be defined at different thickness locations. Based on this method, we measured one curvature at higher thicknesses (more than 100 nm) and one measurement at less than 100 nm and took the average of the amount of the stresses. The average stress can be calculated as follows:

$$\bar{\sigma} = \frac{1}{h_f} \int_0^{h_f} \sigma_{xx}(z) dz , \quad (2 - 15)$$

where, $\bar{\sigma}$ is the average stress while $\sigma_{xx}(z)$ is the amount of in-plane stress with respect to the thickness. In this correlation, also, h_f represents the thickness of the film. Regarding the technique, the LF SiN_x curvature was measured at 48 nm thickness leading to -1815 MPa, while in HF SiN_x it was achieved at around 129.5 MPa at a thickness of 75nm. Based on Fig. 2.7, and Fig. 2.11., and considering Eq. (2-15), the average stress is obtained as -1444.7 MPa and 277.3 MPa, respectively for LF and HF silicon nitride layers. For this reason, for those thicknesses that are much greater than 100 nm respectively for LF and HF, these average stresses were considered. For the nickel layer, also, at the thickness of 50 nm, the amount of stress was obtained at 518.8 MPa. Similar to LF and HF, for thicknesses much bigger than 100 nm, the average stress was obtained at 587 MPa, while for lower than 100 nm it was assumed to be constant.

In addition to thickness, geometry may affect the stress as well [114, 115]. Moreover, mechanical properties including elastic modulus in thin films are also thickness-dependent [116-119]. However, measuring the exact values demand material characteristic processes like nanoindentation techniques which have been out of the scope of this thesis. Hence, we decided to keep it constant at an average value reported in the literature. Considering the information given above and taking the related assumptions, the material properties used in the simulation are tabulated in Table 2.6. Note that, the thermal expansion coefficients (α) and temperature increments (T) were carefully set to give the stresses obtained.

Table 2.6. Material and mechanical properties

Layer Thickness (nm)	E _{SiN_x} [GPa]	E _{Ni} [GPa]	v _{SiN_x}	v _{Ni}	T [°C]	α _{LF} [1/°C]	α _{HF} [1/°C]	α _{Ni} [1/°C]
Lower range thickness ≤ 100 nm	210	200	0.28	0.31	2300	2.75 e-6	-1.95 e-7	-7.75 e-7
Upper range thickness > 100 nm	210	200	0.28	0.31	1820	2.75 e-6	-5.20 e-7	-1.11e-6

In the modeling, we should have first performed a mesh study to reach consistency in our results. Moreover, since the problem was supposed to be solved quasi-statically, determining the size of each section (S) as shown in Fig. 2.19., was crucial to be defined as well for the next level of simulating the isotropic etching. For this reason, both mesh sizes and section sizes were defined by a ratio of the rolled-up circumference (C). To this end, one of the fabricated rolled-up structures shown in Fig. 2.20., with an inner circumference of about

50 μm was considered as a reference, so that both mesh independence and size independence studies were accomplished based on that. The results for four different sections with an increment of three even multiplications of 50 are tabulated in Table 2.7. The simulation graphical user interface (GUI) result is depicted in Fig. 2.21.

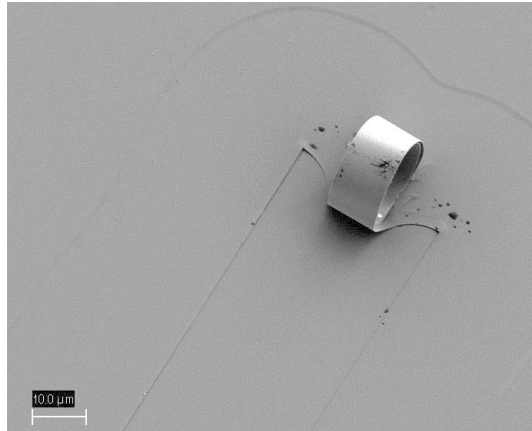


Fig. 2.20. SEM image of a rolled-up bilayer ribbon ($LF=32\text{ nm}$, $HF=60\text{ nm}$)

Table 2.7. Mesh and Section independence study ($C=50\ \mu\text{m}$)

Mesh size \ Section size	C/50		C/100		C/200		C/400	
	D [μm]	Time	D [μm]	Time	D [μm]	Time	D [μm]	Time
C/400	-	-	-	-	-	-	16.22	17'38''
C/200	-	-	-	-	16.23	3'59''	16.23	10'50''
C/100	-	-	16.30	1'16''	16.25	4'35''	16.24	17'45''
C/50	17.22	31''	16.36	1'3''	16.30	4'2''	16.28	16'25''

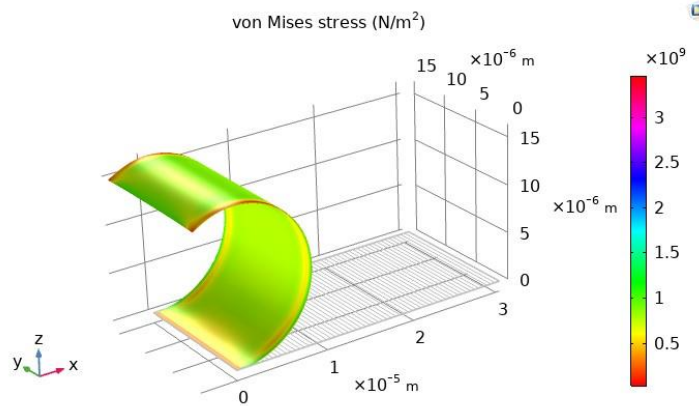


Fig. 2.21. Simulation result of rolled up bilayer nanomembrane with an LF/HF=32 nm/60 nm

The optimized mesh sizes, as well as section sizes, were achieved at C/200 based on the results of Table 2.7. These amounts are used in the rest of all of our simulations. For instance, as depicted in Table 2.8., the simulation results were compared to the experimental rolled-up nanomembranes, with an obtained average error of around 2 %. This can be considered as an acceptable comparison showing the method of simulation is reliable. A wide range of factors can be the culprit for the discrepancy between the simulation and experimental data; for instance, the neglected uncertainties corresponding to the stress gradient through-thickness, mechanical properties variation through-thickness, and the calculation method discussed in Table 2.7. Moreover, as all the structures were floated after release, it was demanding to take scanning electron microscopy (SEM) images of all of them. Therefore, there might be some error of measurement because of the refraction of light through the etchant liquid which causes the edge of the images to be seen blurry. Another factor that may cause this discrepancy is the thickness variation through the surface of the sample (that might exceed even more than 10 nm from one side to the other) because of edge effects that were discussed earlier. Although we tried to use the samples from the middle of the whole wafer, which is more uniform than the edges, there are possibilities to have nonuniformity in the thickness, as well as the stress through the surface.

Table 2.8. Comparison of 2D and 3D simulation results with experimental data.

LF SiN _x /HF SiN _x [nm]/[nm]	Measured Diameter [μ m]	Calculated Diameter in 2D [μ m]	Calculated Diameter in 3D [μ m]	Error

32/60	15.82	15.78	16.23	2.6 %
40/75	20.70	19.61	20.96	1.25 %
160/305	88.90	89.48	89.83	1.05 %
160/390	111.20	113	113.34	1.92 %

2.2.2 Imperfect and perfect helices

In the amorphous nanomembranes, the etching process starts isotropically from everywhere, and the final shape can be a rolled up structure, imperfect helices, or perfect helices. To mimic the etching process in modeling, regarding the quasi-static releasing method discussed in the last subsection, and the amount of optimized mesh and section sizes, we considered the boundary conditions shown in Fig. 2.22. Based on this figure, we modeled the bilayer or sandwich structure as an initially confined cantilever or mesa. Then, it gradually released from the substrate step by step from all sides with equal sections of S , ending up with a straight red line ($L-W$). Finally, the structure is completely released but confined by the green point to prevent the numerical analysis to enter an infinite loop.



Fig. 2.22. Schematic view of the general modeling of the etching process

This method can be considered as a generalized model for all isotropic etching processes that can lead to either rolled-up, imperfect or perfect helices. The deformation and energy results obtained by this model will be discussed in detail in the next chapter. This model is very helpful especially in the simulation of the behavior of strained nanomembranes with low aspect ratios since the final shape of the structure is pre-defined before the structure is fully released from the substrate.

At high aspect ratios, however, the structure temporarily sticks to the substrate after the etching process is finished, due to capillary force or intermolecular interaction forces (more details regarding the effect of aspect ratio to the behavior of rolling will be given in the next chapter). For this reason, the structure tends to release its energy from the longest side of the ribbon, i.e. diagonal line. Fig. 2.23. is a time-lapse image of a high aspect ratio bilayer that is released gradually once putting in the etchant. We can see that the sacrificial layer is removed from every side of the ribbon up to the time of 3'29'', at which the structure is fully removed. However, it does not have the final shape as a result of adhesion. After a while, it starts rolling from the diagonal line that is gradually moving through the length of the ribbon and finally deforms as a compacted helical structure. Our modeling is inspired by this behavior so that we just use three oriented lines with equal distances (i.e. i) (0,0) and (L,W), ii) (7/30 L,0) and (23/30 L,W), and iii) (14/30 L,0) and (16/30 L,W)), and point constrain in the middle to let the numerical method reach a convergence. Using such a method, we skipped the sectioned releasing and just simulate the behavior of the structure after sticking; therefore, we only used the optimized mesh size that was discussed in Table 2.7.

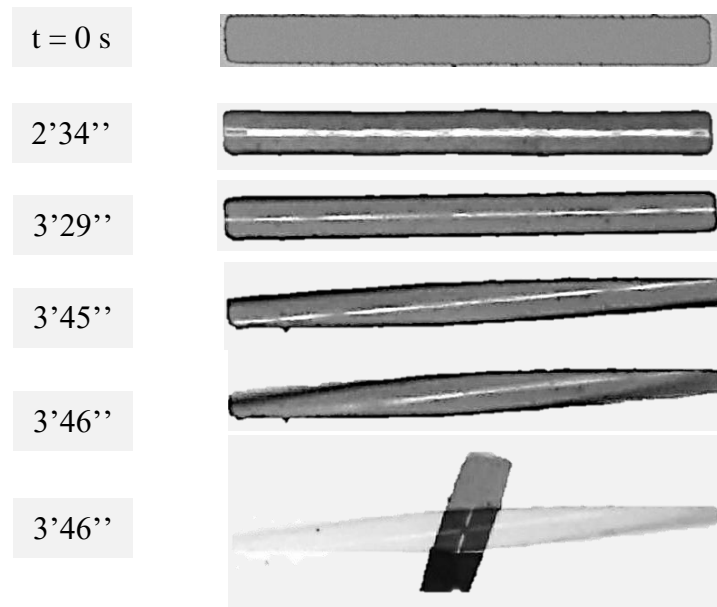


Fig. 2.23. Time-lapse images of the rolling of a ribbon under etching process ($L=10 W$, $C/W=3.5$),

2.3 Magnetic and acoustic propulsion setup

In this section, the setup used for testing the locomotion of the fabricated swimmers is examined. The setup in our experiments consists of four main parts: a) Helmholtz coils which generate the rotating magnetic field [120], providing the required torque for the swimmer to rotate and move, b) the PDMS chamber, c) piezoelectric transducer, and wave generator to provide the acoustic amplitude and frequency, and d) the optical microscope equipped with a camera.

a) Magnetic field and magnetization

As mentioned earlier, since the swimmer's weight is well-distributed, the control over the orientation of the swimmer was neglected. For this reason, we just used two pairs of coils that are perpendicular to each other as schematically depicted in Fig. 2.24.(a). The coils were previously designed in our group so that it provides the required magnetic field while well-matching the optical microscope has been utilized. The housing of the coils was designed and fabricated by the 3D printing process. The dimensions of the coils and the magnetic field they generate are depicted in Table 2.9. Note that both y and z coils have been designed with the same properties to generate a uniform magnetic field. A rotating magnetic field on that plane exerts a magnetic force (F_m (N)) and torque (τ_m (N·m)) on the swimmer, which is given as [121, 122]:

$$\mathbf{F}_m = v(\mathbf{M} \cdot \nabla)\mathbf{B} \quad (2 - 16)$$

$$\boldsymbol{\tau}_m = v\mathbf{M} \times \mathbf{B} \quad (2 - 17)$$

where v is the volume of the magnetic thin film (i.e., nickel), \mathbf{M} ($\text{A}\cdot\text{m}^{-1}$) is the magnetization of the nickel thin film layer. In soft magnetic thin films, the magnitude of the magnetization is a function of the applied field. \mathbf{B} (T) is also the external magnetic field vector with a magnitude of B_0 which is simply calculated for a single coil as follows

$$B_0(z) = \frac{\mu NI}{2} \frac{R^2}{(R^2 + z^2)^{\frac{3}{2}}}, \quad (2 - 18)$$

in which μ , N , I , R , and z respectively represent the permeability of free space, the number of turns, the current (A), the radius of the coil (m), and the distance from the center of the coil from the coil axis. It is obvious that the maximum magnetic field magnitude for a single-coil is obtained at $z=0$. However, using Helmholtz pair coils the governing equation is changed to the follows:

$$B_0(z) = \frac{\mu N I R^2}{2} \left\{ \frac{1}{\left(R^2 + \left(z + \frac{d}{2} \right)^2 \right)^{\frac{3}{2}}} + \frac{1}{\left(R^2 + \left(z - \frac{d}{2} \right)^2 \right)^{\frac{3}{2}}} \right\}, \quad (2 - 19)$$

where $d=R$ is the distance between two coils in meter, while the origin of the coordinate system is set to be between the two coils which is located at a distance of $R/2$ from each coils. Based on the equation, at the distance of $z=0$, the magnetic field is $0.68 \mu N I / R$ while in the half distance of two coils it is obtained as $0.72 \mu N I / R$. This shows that how uniform the magnetic field would be if two coils are coupled. In our group, we used this configuration together with taking advantage of an interface to set the given shifts in order to compensate for the possible uncertainties in fabrication. However, to have the microswimmer rotated smoothly and perfectly, two pairs of coils have been utilized with an out of phase sinusoidal magnetic field as follows to generate a rotating magnetic field (as depicted in Fig. 2.24. (a)):

$$\mathbf{B} = B_0 [0 \quad \cos(\omega_m t) \quad \sin(\omega_m t)]^T, \quad (2 - 20)$$

where, $\omega_m = 2\pi f_m$ is the rotation rate, by changing the sign of which the rotation of the swimmer changes, and as a result, the forward or backward swimming is achievable. Before putting the swimmer inside the magnetic field, we collected them with a magnet to change the magnetization orientation in the lateral direction (shown in Fig. 2.24. (b)). Applying the rotating magnetic field, the swimmer moves as a result of created backward waves (depicted in Fig. 2.24. (b)). The magnetic fields were measured by a gaussmeter device.

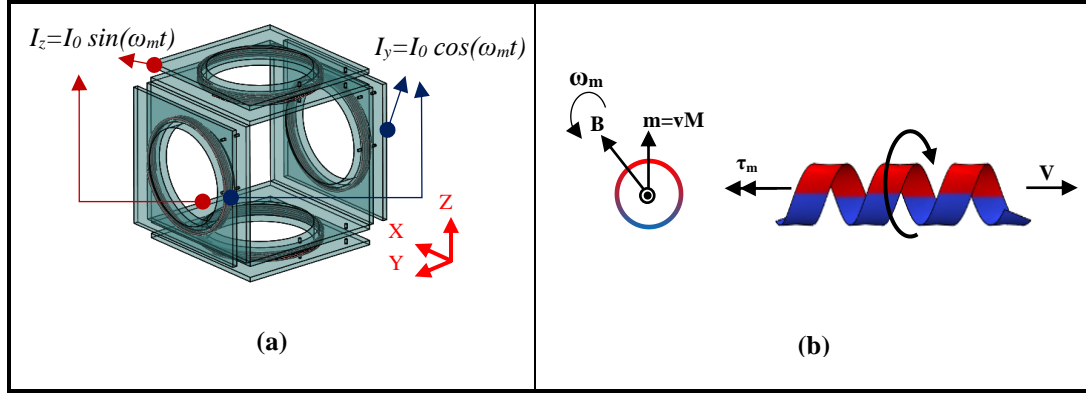


Fig. 2.24. a) Helmholtz coils, and b) magnetization, and propulsion schematic

To apply the required current through the coils Maxon ADS_E 50/5 motor drivers and NI DAQ hardware has been utilized. A MATLAB user graphical interface was designed to control the amount of alternating current at a defined frequency. Using this interface, also, one can define phase shift coefficients to have a smooth uniform rotating magnetic field. Moreover, this interface that is synchronized by an oscillator is capable of controlling the amplitude and frequency of the applied acoustic field.

Table 2.9. The properties of the coils

Inner Diameter [cm]	4.5
Outer Diameter [cm]	6.5
Thickness [cm]	0.25
Number of Rotations	100
Wire Diameter [mm]	0.5
Approximate Wire Length [m]	10.74
Measured Resistance [Ω]	1.9
Magnetic Field [mT/A]	2.1

b) PDMS Chamber

In addition to an mm-scale tube, to check the behavior of the swimmer in a wide chamber, and also see the effect of the acoustic field and traveling waves on the swimming performance, a cuboid PDMS chamber was fabricated with the dimensions of 1 cm×1 cm×0.5 cm. To this end, we had an aluminum modular mold fabricated by a CNC machine. The exploded view also and the image of the mold are depicted in Fig. 2.25.

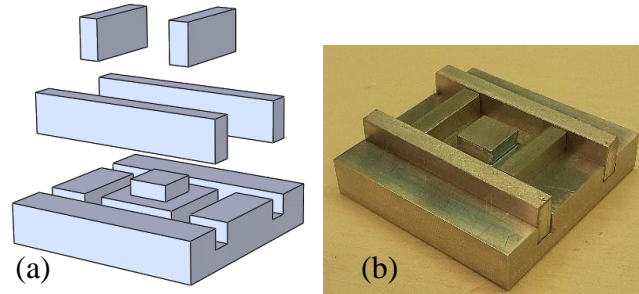


Fig. 2.25. a) Schematic exploded view of the mold, and b) fabricated aluminum mold

The PDMS polymer base with a curing agent (sylgrad 184 silicone elastomer kit, Dow Corning, Midland, MI, USA) with a ratio of 10:1 is mixed and stirred smoothly. Then it is poured inside the mold followed by a repetitive degassing process by a low vacuum pump to remove the bubbles inside the material. Finally, it is put in an oven for two hours at 75 °C to have it solidified. Subsequently, the mold with PDMS is put somewhere to cool down. After that, by separating the movable parts of the mold, the PDMS chamber can be removed from the mold readily. Afterward, a piece of a microscope glass slide is accurately cleaned by acetone so that no particles or stains remain on it. The final step is to use an oxygen plasma process (either by a vacuumed chamber or by utilizing a Corona oxygen plasma treater) to bound the PDMS to the glass. The final product is depicted in Fig. 2.26.



Fig. 2.26. PDMS chamber bonded on a microscope glass slide

c) Piezoelectric transducer

In this thesis, we used a piezoelectric disk element located next to the PDMS chamber. This transducer was connected to an oscillator (Agilent Keysight 33220A 20MHz

Function/Arbitrary Waveform Generator) that provides the maximum amplitude of 10 volts and the maximum frequency of 20 MHz. However, we just used two frequencies in the range of 1-10 kHz. We did not use an amplifier to stay in a safe mode to not break the glass. In the acoustic experiment, we mainly focused on vibration modes so that the glass-PDMS was sandwich between two plexiglass pieces, that were cut through a laser cutting process. This assisted us to have doubly clamped beam vibration modes coming out of the piezoelectric actuation. The setup is depicted in Fig. 2.27. The liquid we used was isopropyl alcohol (IPA) since it has a lower surface tension than water, by which the swimmer will sink easier. However, it is quickly evaporated, so that we had to use a cover glass with a thickness of 0.15 mm and coated with an anti-vapor spray.



Fig. 2.27. The glass-PDMS-transducer setup

d) Microscope and camera:

To record the swimming processes under a rotating magnetic field and acoustic field, an optical microscope (Nikon SMZ1270) equipped with a camera (Basler acA2440-75um) was utilized which allowed observing and recording the real-time images of the swimming. The framerate of the recording was fixed at 25 FPS, and the contrast of the images is possible to be changed simultaneously to make the image-processing straightforward. Using the grids and marker point of the camera in the middle, also, help to fix the position of the chamber, so that the obtained results have consistency and are reliable. The setup is shown in Fig. 2.28.

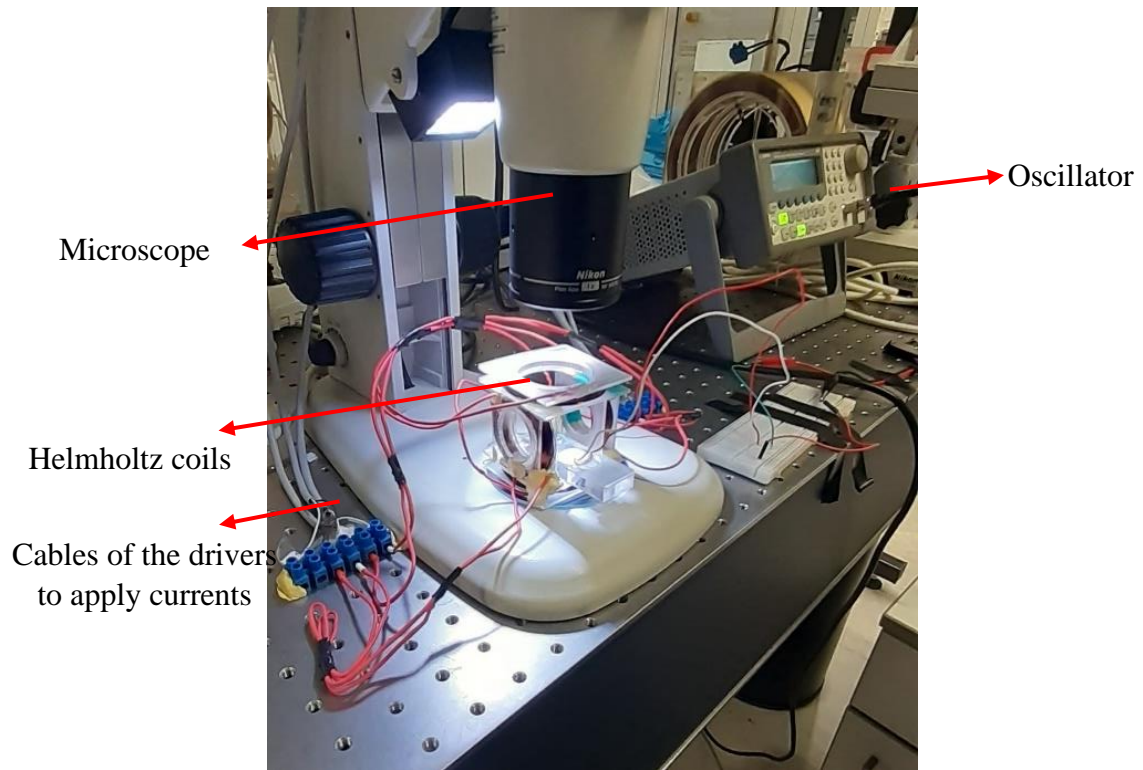


Fig. 2.28. The setup used for micro swimming performance

3 RESULTS AND DISCUSSIONS

In this chapter, the fabrication and simulation results of two methods of fabrication will be examined. First, we will elaborate on the first method corresponding to the effect of geometry on obtaining helical structures, and subsequently, the grating method and the effects of its significant parameters. In the end, the swimming performance of a swimmer made of the grating method will be investigated under a rotating magnetic field and acoustic actuation.

3.1 First method: Geometry modification (thickness variations)

As previously mentioned, we used amorphous nanomembranes in which the mechanical properties are distributed isotropically. Hence, to get helical ribbons, one should induce the structure to roll in a desirable direction in order to not obtain a tube-like or ring-like structure. One of the best options is to take advantage of the geometry modification in microstructures.

During every rolling processes, two regions can be observed: 1) passive region, in which the structure is still constrained to the substrate by either sacrificial layer or other factors like van der Waals intermolecular interaction or capillary force resulting from the liquid trapped between ribbon and substrate, and 2) active region, in which the stresses inside the structure are released after detaching, letting the strain energy to be released by deforming the structure in the form of bending and stretching/compacting, respectively in directions perpendicular to the edges and parallel to the edges. The bending results in scrolling, and stretching/compacting leads to wrinkling. Normally in thin films, after a while, the wrinkling shapes flatten to pave the way for rolling. The rolling continues from the edges at which the maximum energy is released. For instance, in a ribbon with a high aspect ratio, it is most likely to have the structure rolls from the long side edges at which energy is more released. However, in some specific aspect ratios, it might be different so that the structure experiences a totally various rolling direction. This is believed to be due to the deformation history or not perfectly isotropic etching in which rolling from the other side rather than the long side continues even if the energy is not as big as the long edge. For this reason, it has been demonstrated that in

semiconductor and polymer materials the rolling direction depends on three main geometrical factors including width (W), length (L), and circumference (C) of the roll-up nanomembrane, together with energy minimization, deformation history, and isotropic kinetic control of etching. According to those factors, generally, the rolling could happen either from the long side, short side, or diagonal directions [70, 87]. We carried out systematic experiments to see the rolling behavior of bilayer and sandwich structure, based on which the design and modeling have been accomplished. In this design, the circumference and length were considered to be constant while the width varied. To this end, a mask was prepared to cover a range of rectangular shapes as shown in Fig. 3.1. Although we investigated ten shapes, however, we discussed the four most important ones which give a view of the effect of geometry on rolling. The nondimensional ranges were considered as follows:

- $L/W \cong 1, 2, 4, \geq 8$
- $C/W \cong 0.35, 0.7, 1.4, \geq 2.8$

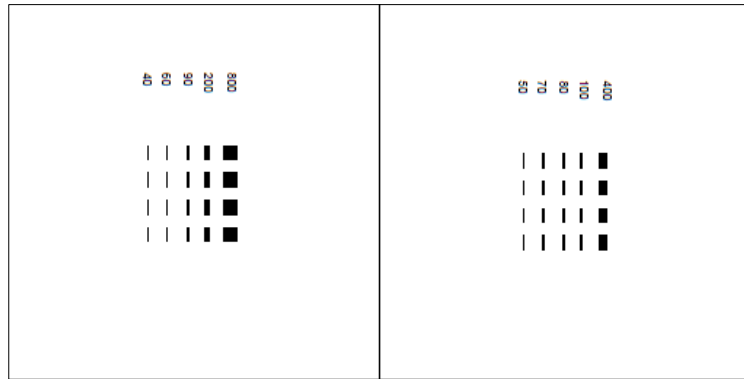


Fig. 3.1. Mask designed for investigating geometric effects in rolling

Given in Fig. 3.2. are four various rectangular patterns with the same length and circumference and different widths that were released and rolled up after immersing in chromium etchant (the etchant used for removing the sacrificial chromium layer). Generally, in self-rolling processes, the structure tends to deform in a direction through which the energy-releasing is maximum [70, 87]. For this reason, in an aspect ratio of 1, the structure tends to roll in all directions as depicted in Fig. 3.2. (a). In this experiment, we used a silicon nitride bilayer of a total thickness of 465 nm, which is much thicker than the bilayer mentioned in [87] which has a thickness of 38 nm. In addition, the elastic modulus of silicon nitride is much higher than the semiconductor material used in [87] and polymers investigated in [70]. For

this reason, our bilayer would suspect to show different behavior once undergoing bending moment as it has a higher flexural rigidity (EI). For instance, in the semiconductor membranes discussed in [87], some edges were compromised to allow other edges to continue rolling once reaching a deadlock, whereas our SiN_x bilayer entered a plastic region followed by experiencing failure in some parts to insist on the direction of rolling. In this case, those regions that started the rolling determined the final shape, showing the role of history dependency in the rolling direction. In our simulation, however, as we assumed a fully elastic model in which no failure was considered, we failed to precisely predict this behaviour coming from the stress concentration in deadlock regions. Yet, as it clears from the third column of Fig. 3.2.(a), rolling continues from all sides ending up with a deadlock region similar to the experimental observation.

As we increased the length to width ratio two times by decreasing the width (shown in Fig. 3.2. (b)), at the beginning of the etching process other edges embarked upon rolling followed by opening themselves after a while, thereby the long edge taking the rest of the rolling process. Similar to the aspect ratio of 1, the simulation result just predicted the rolling behavior right before the deadlock region after which failure happened. Typically, as mentioned earlier, rolling happened from edges that are energetically more preferable. This can be seen from part c of the figure in which the aspect ratio size is more sensible, such that the rolling started and continued from the long edges, leading to a long tube shape. Since no tearing occurred owing to the lack of deadlock regions, our modeling managed to have a good prediction of the rolling direction preference and the final shape of the structure.

The aim of mentioning three previous cases was to understand how aspect ratio can change over the rolling-up behavior of strain-induced nanomembranes. Now, we take a step further to go through high aspect ratios ($L \gg W$) while $C \gg W$, where the wrinkling generated inside the structure came into play to define the final deformed shape of the structure. In such situations, although rolling occurred from the long side edges, however, since the width is not long enough to lead a round of rolling, the nanomembrane did not restrict itself to just long side rolling as it stays in an unstable position. Instead, to minimize its energy and reach a stable state, it tended to roll from the opposite corners (as it could be seen as the longest edge after releasing the structure from the substrate) and then compact as illustrated in Fig. 3.2. (d).

This phenomenon can be dedicated to the behavior of the structure once detaching step by step and releasing completely from the substrate. As the structure is separated from the substrate gradually, in addition to the rolling about long and small edges, it wrinkles through both edges as well. The wrinkling as reported earlier in [123, 124] can affect and change the rolling behavior completely based on a wide range of parameters including aspect ratios. In our case, the wrinkling shapes might have rarely affected the behavior of rolling in smaller aspect ratios since they had enough time to be flattened to a large extent before the structure is completely released from the substrate. However, at higher aspect ratios and circumferences, once the structure is released, it does not have the final shape instantaneously; instead, while releasing the wrinkled shapes from the long edges, it adhered to the substrate mainly due to capillary force. After a while, the rolling direction changed from the long side to the diagonal side, and due to the stored energy, all of a sudden, the structure snapped between an unstable position to the compacted helical position in which the structure was in its most stable state (this processes previously depicted vividly in Fig. 2.23).

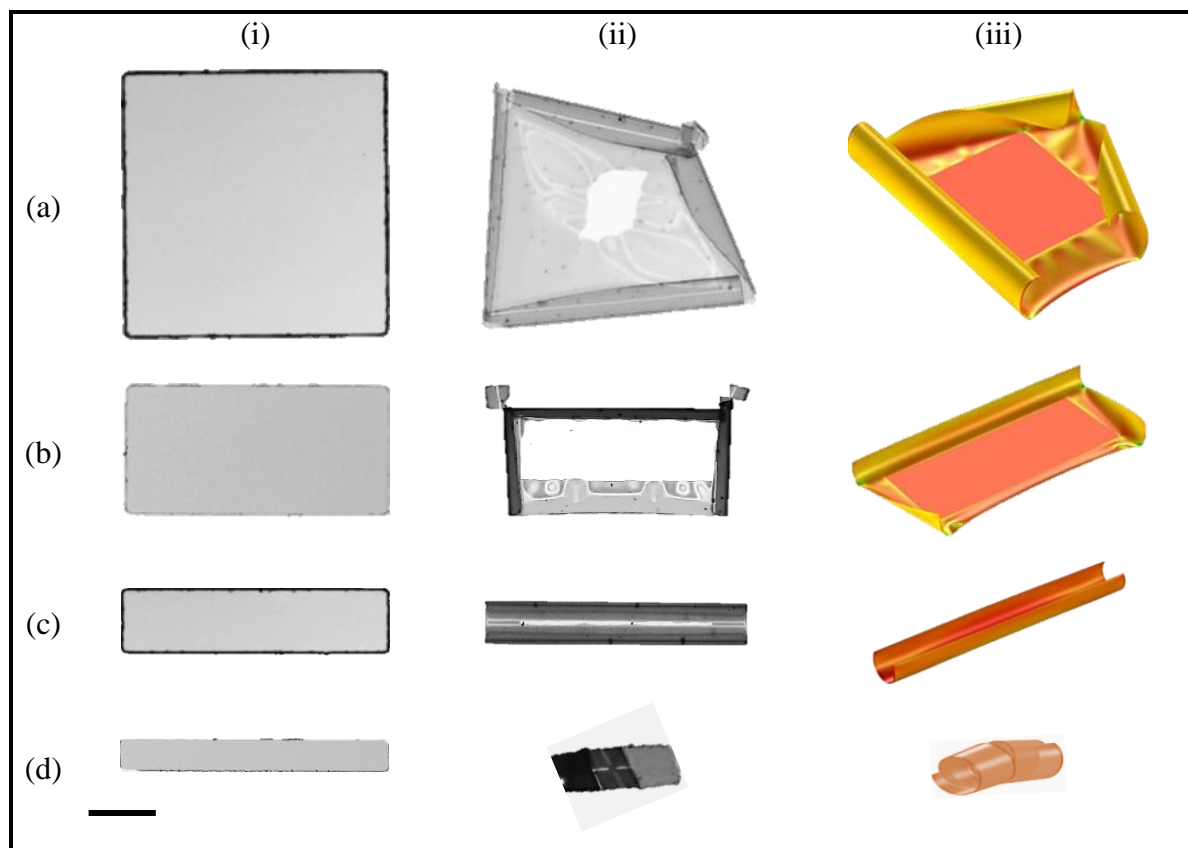


Fig. 3.2. Effect of aspect ratio on rolling while the length is $800\ \mu\text{m}$. a) $L/W=1$, and $C/W=0.35$, b) $L/W=2$, and $C/W=0.7$, c) $L/W=4$, and $C/W=1.4$, and d) $L/W=8$, $C/W=2.8$ (Scale bar size is $200\ \mu\text{m}$)

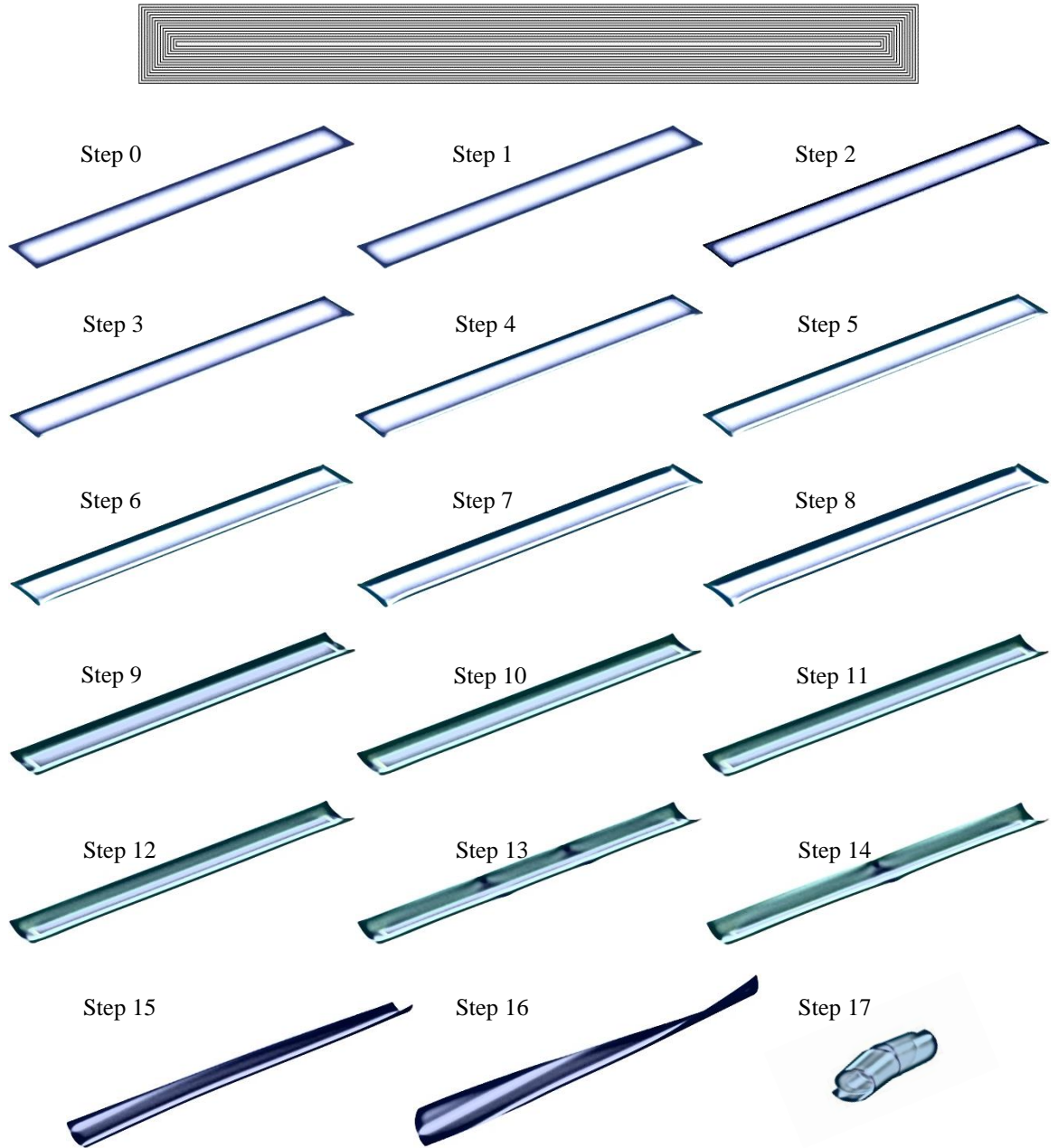


Fig. 3.3. Modeling and simulation of rolling process: steps of releasing

For high aspect ratio ribbons, in which the microstructure experiences sticking and then deforming, we may use additional extra boundary conditions in order to make the simulation at least two times faster. For this reason, Fig. 2.23. was given in which the behavior of the structure right before releasing by means of a set of video frames was depicted. This can tell us that the structure roll about a diagonal line first; then this line moves through the

length of the ribbon two times with fairly identical distances. Considering this behavior, the whole process of the deformation is depicted in Fig. 3.3. with 18 steps in which each step was considered to be a physical initial condition for the next step. From steps 13 and 14 of this figure, one can identify how the wrinkling came into play to determine the final shape of the structure. Illustrated in Fig. 3.4., is also a bar graph that shows how total elastic strain energy inside the structure (obtained from Eq. (3-1)) changes while detaching from the substrate. The stress and strain are calculated for the case where the geometric nonlinearity is considered as depicted in Eqs. (2-10) - (2-13). The graph elucidates a fairly linear reduction of the energy up to step 12, after which the structure experienced a change in the wrinkling mode in step 13 with a small change in the energy, followed by a drop to reach the final value at step 17. As a consequence, this reduction behavior of the calculated elastic strain energy could be considered as a testimony for the role of energy minimization in defining the final compacted helical shape after releasing

$$U_{tot} = \frac{1}{2} \int_{\Omega} S: \varepsilon_{el} dV, \quad (3 - 1)$$

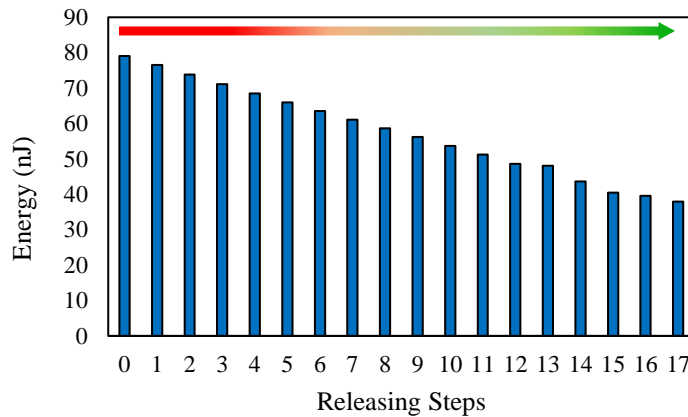


Fig. 3.4. Energy minimization graph

In addition to the aspect ratio, thickness variation can also change the rolling behavior of strain-induced bilayer or multilayer nanomembranes. For high aspect ratio ribbons, it was proven that once released from the substrate, the structure shows a helical behavior with a periodicity of zero (compacted and overlapped helices) due to the high stored energy inside. For this reason, for the same strain-induced bilayer or multilayer thin films, to obtain a perfect

helical structure, one may have to decrease the potential energy to prevent the structure from being compacted. The most straightforward method to do so is to keep the thickness as low as possible. This thickness reduction, on the other hand, decreases the flexural rigidity, eventuating in a smaller rolling diameter. If we assume the helical angle as a constant, the lower the diameter should give lower λ (periodicity), so that even energy reduction as a result of decreased thickness may not be useful to have a reasonable helical structure. Interestingly, in layered thin films with comparable thicknesses, the behavior of the diameter (or curvature) of the rolled-up nanomembranes with respect to the thickness reduction of the top layer is nonlinear; that is, the diameter firstly decreases with a gentle slope to hit a minimum value followed by a sharp-slope ascending behavior [125, 126]. The physics behind this phenomenon is believed to be due to the confrontation between actuation force and torque explained in detail in [127], which naturally can be observed in the analytical formula for finding the diameter of strain-induced bilayer or multilayer thin films as well [93, 128].

The inclusion of such facts in fabricating high aspect ratio ribbons would have mitigated abrupt snap behavior of the structure once releasing, resulted in a helical ribbon. To this end, first we calculated the diameters of a perfectly rolled up bilayer LF SiN_x / HF SiN_x while decreasing the HF thickness (shown in Fig. 3.5.) in order to have an approximation about where the structure reaches the extremum point. Then, we tried to check the behavior of the structure experimentally in thicknesses below that value (distinguished by green background color in the figure), in which the structure was susceptible to show a different deformation instead of compacting since the energy inside the structure became much lower. To see this effect on generating helical structures, Fig. 3.6. is presented in which three ribbons with various length is used, while length/width is kept constant at 10 (from i to iii). Also, three different SiN_x HF thicknesses (from a to c) are used; sure enough, at lower thickness range, helical structures were obtained for the lowest thickness amongst others (shown in Fig. 3.6. (a)). It is clear that in the case of using longer ribbons, as depicted in Fig. 3.6. (a-iii)), one can obtain a full pitch or helical structure. To further clarify the issue, Fig. 3.6. (b). is given, in which by adding just 10 nm to the thickness, perfect helical bilayers with two identical rounds were obtained. By Increasing the thickness to 300 nm (shown in Fig. 3.6. (c).) overlapping occurred, leading to helices with zero λ s. The diameter ranges for the LF thicknesses of 20 nm and 300 nm for a set of nine fabricated structures for each (defined by error bars) are

depicted in Fig. 3.5. as well. As expected, since in the green region the rolling behavior is more sensitive to thickness variation, the error bar shows a deviation of around 10 μm in measured diameters. This is believed to be the errors coming from the measurement or fabrication processes. However, in the yellow region which is less delicate to thickness changes, the deviation decreased to less than 5 μm .

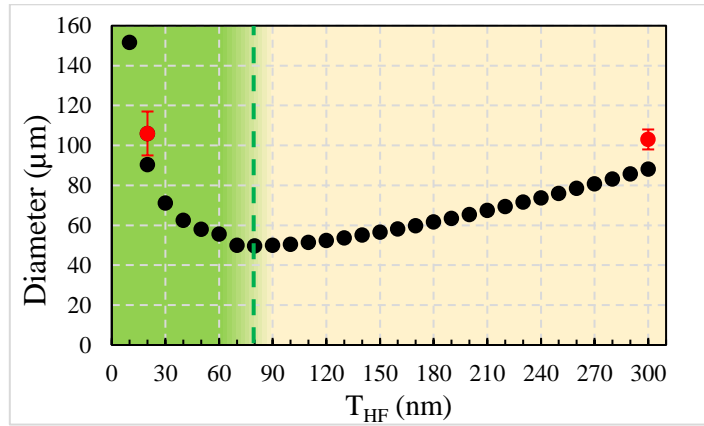


Fig. 3.5. Diameter changing behavior regarding thickness variation (black filled circles are simulation rolled-up ribbons, red filled circles are experimental data)

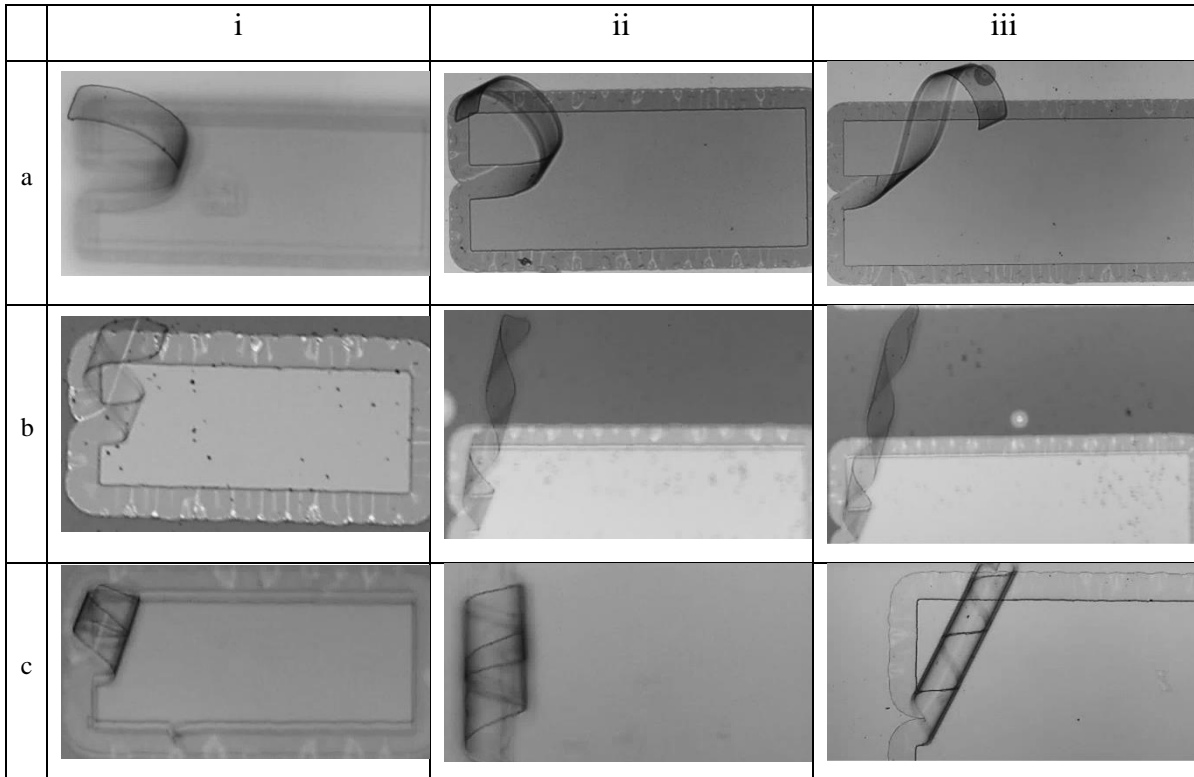


Fig. 3.6. Thickness variation effect while T_{LF} was kept constant at 245nm for all cases. a) $THF = 10$ nm, b) $THF = 20$ nm, and c) $THF = 300$ nm. The widths of the ribbon for part i, ii, and iii are respectively 40 μm , 90 μm , and 120 μm while the length for all cases is ten times greater than the width

To check the effectiveness and repeatability of this method, we also performed a couple of more experiments for both bilayer and sandwich structures with various thicknesses as depicted in Fig. 3.7. In part (a) of the figure, the thicknesses of both LF and HF silicon nitride were lowered so that the interesting twin helical structures were obtained. This figure can tell us that the wrinkling and its phase change could have a decisive role in the final shape and orientation of the helical ribbon. For such a case, we observed that the ribbon does not deform abruptly, instead, it follows a wave-like path coming out of the wrinkled film releasing, causing the structure to temporarily stick to the substrate by capillary force and then detach step by step. Although the path could be various from one structure to the other, the final shape is believed to be the same for identical ribbons (like Fig. 3.6. (b)). We also took advantage of the same technique to produce even smaller anchored helices (the SEM image is given in part b Fig. 3.7.). However, the versatility of the technique is more obvious in part (c) of the figure by producing sandwich micro helices. As discussed earlier, we first characterized the thickness variation by the analytical model to have a view of the bi-behavior of the structure, then, we took the obtained parameters in our fabrication. For instance, we used a sandwich structure made out of three layers (LF SiN_x/Ni/LF SiN_x) with strain mismatch inside, so that by decreasing the top layer thickness we reached its green region (discussed in Fig. 3.5.) in which helical structure can be generated.

Although a straightforward method in terms of fabrication, the aspect ratio/thickness modification method like other methods has some deficiencies. For instance, the thickness sensitivity of this method may pose a challenge in controlling the helical parameters including helical angle, or wavelength, requiring a wide range of characterization processes. Moreover, this method is specifically useful for the applications in which the helical structures are anchored to the substrate. we believe that this is due to the processes of releasing the wrinkles which may result in imperfect helices in case of using no anchors, as depicted in Fig. 3.8. for sandwich microstructures. All things considered, in addition to the mentioned method, we studied the effect of other geometry modifications (topography modification) on the behavior of sandwich nanomembranes that will be explained in the next section.

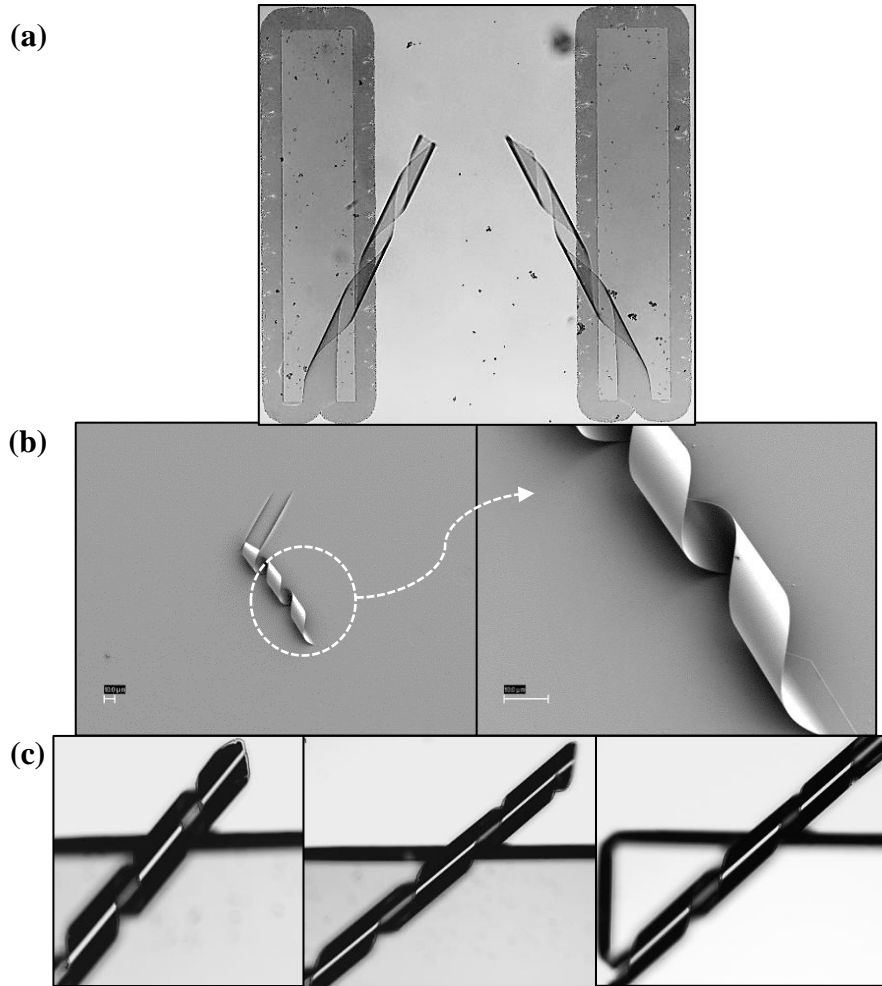


Fig. 3.7. Aspect ratio and thickness modification method. a) image of an 80nm SiN_x LF/10nm SiN_x HF bilayer with a width of 70μm and aspect ratio of L/W=10, b) SEM image of a 15nm SiN_x LF/30nm SiN_x LF bilayer with a width of 15 μm and aspect ratio of L/W=10, and c) image of a sandwich LF/Ni/LF layer with the thicknesses of 35nm/100nm/55nm. (i, ii, and iii are respectively related to the width of 90μm, 110μm, and 120μm while the aspect ratio was constant at L/W=10)

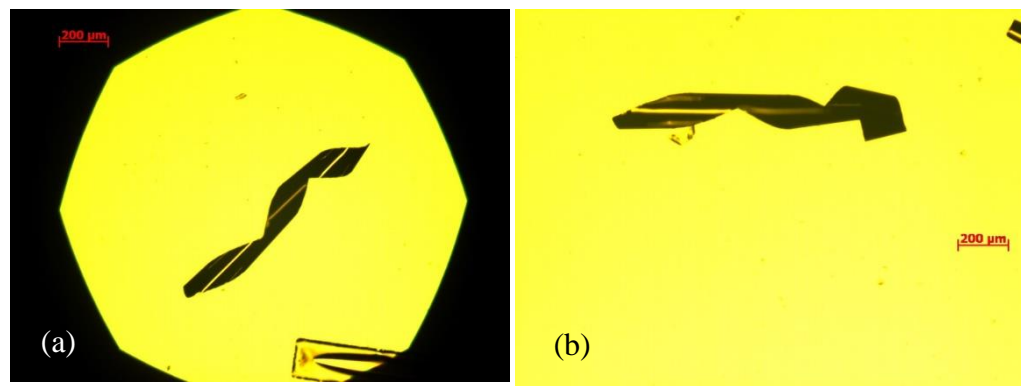


Fig. 3.8. Micro helical sandwich nanomembrane fabricated by aspect ratio/thickness modifications., a) perfect helical ribbon, and b) imperfect helical ribbon

3.2 Second method: Geometry modification (Grating)

In this section, we will go through the parameters effective on topological patterning leading to obtaining helical nanomembranes. As previously mentioned, regarding Fig. 2.16., three different nondimensionalized parameters, w/L , g/L , and H/T_{HF} were considered to see the behavior of the structure once systematically playing with various values of these factors. However, as discussed in Fig. 3.2., in addition to the aforementioned parameters, the aspect ratio is also a significant factor that can change the rolling direction of the structure even if the grating patterns are created in the nanomembrane. Hence, in order for the swimmer dimensions to be minimized, in all of our designs, we used a constant aspect ratio of around 9, so that the effect of the grating parameters on a ribbon with a width of 120 μm , and a length of 1050 μm , LF thickness of 160 nm, nickel thickness of 50 nm, and HF thickness of 310 nm will be examined.

As depicted in Fig. 3.2., in high aspect ratios, if there are no topological modifications, the structure tends to minimize its energy by deforming as a compacted helical ribbon. Now, if the grating patterns are imposed on the nanomembrane, three kinds of structures can be put forward based on the combinations of the grating parameters as represented in Fig. 3.9. In Fig. 3.9. (a), the structure is deformed like a perfect ribbon without any grating patterns on it. This shape is obtained whenever the effect of the grating is not enough to dominate the original rolling preference. Playing with the parameters of grating, one can take the lead of rolling, resulting in a perfect helical structure as demonstrated in Fig. 3.9. (b). However, overusing the grating parameters can bring about imperfect helical nanomembranes as Fig. 3.9. (c). For this reason, in this thesis, we have performed a characterization study to obtain helical structures that can be used as microswimming robots. Therefore, since the nickel layer is the cornerstone of the microswimmer, it has to be survived during the fabrication process as much delicate as possible. For this reason, we were limited to keep the top layer of the sandwich (HF SiN_x), so that no reaching the nickel layer after grating patterns.

In accordance with Fig. 2.16., four grating parameters are investigated with the following ranges: $\theta = 45^\circ, 50^\circ, \text{ and } 60^\circ$, $H/T_{HF} = 0.2, 0.4, \text{ and } 0.6$, $w/L = 0.1, 0.175, \text{ and } 0.25$, and $g/L = 0.025, 0.05, \text{ and } 0.075$. In all 81 experiments that were carried out, only in case the perfect helical structures were obtained. Given in Fig. 3.10. (a) is a bar chart that shows the

percentage of obtained perfect helices for all three heights and angles at specific w/L and g/L ratios. From the figure, one can conclude that lower values of g/L at a higher w/L ratio have more chance to get helices. On the contrary, once the g/L is increased, the ratio of w/L has to be decreased to result in helices. It can be concluded that both grating regions and non-grated regions play an integral role in defining the helical behavior of the structure as discussed earlier analytically for grating bilayers [88]. Obviously, the higher the grating or non-grated regions, the lower the aspect ratio of those regions; hence, as discussed previously in Fig. 3.2., at low aspect ratios the structure tends to release its energy from all sides. Therefore, we may not be able to have rolling from the long side of those regions; that is, the rolling may not occur perpendicular to the grating patterns, leading to either compacted or imperfect helical structures. on the other hand, the higher the grating or non-grated regions may result in a decrease of the effect of grating since the frequency of the patterning is decreased through the length of the ribbon.

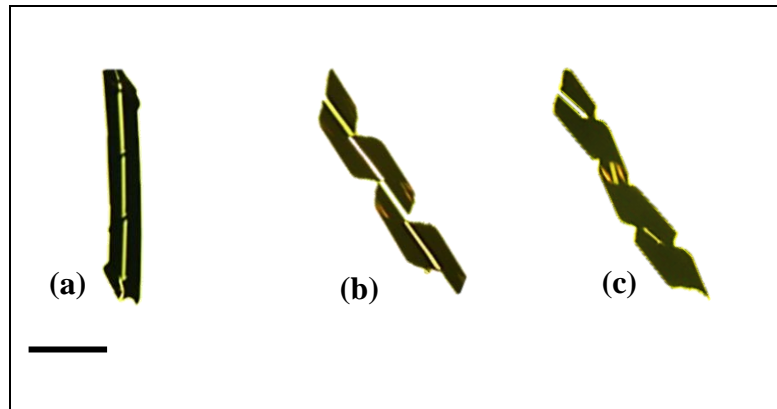


Fig. 3.9. Various configurations of patterned nanomembrane: a) Fully compacted helix, b) perfect helix, and c) imperfect helix. (the scale bar is 200 μm)

With an eye to the mentioned reasons, optimized values for g and w have to be considered. For this reason, we performed another set of experiments in which both $w/L=g/L=0.025$. This kind of experiment resulted in 100% perfect helices for $H/T_{\text{HF}}=0.4$ and 0.6 for all angles due to the following reasons: 1) the aspect ratio of the grating and non-grating regions become high enough to let those regions roll up from the long edges (perpendicular to the length of the grating parts), and 2) decreasing the w/L lead more grating patterns through the length of the ribbon, such that the effect of the grating is more

pronounced, resulting in smoother rolling. This helped us to achieve helices with lower periodicity as depicted in Fig. 3.11. The effectiveness of low ratios of w and g was also reported by Huang et al [71] for single layer step-like titanium thin film as well.

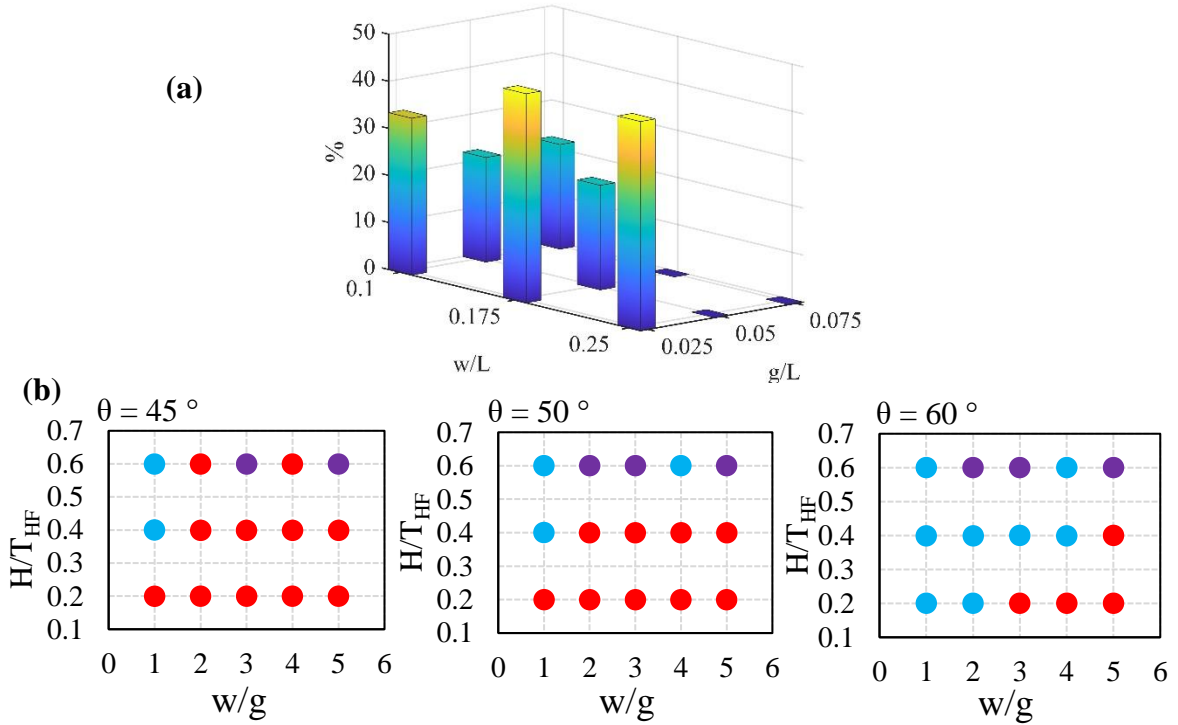


Fig. 3.10. a) The percentage of the helical structures that are obtained based on various grating angles and depths, and b) the scatter graph of obtained compacted (red), imperfect (purple), and perfect (blue) helices with respect to the grating angles

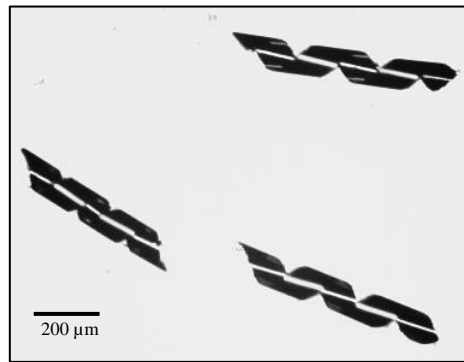


Fig. 3.11. helical structures obtained by grating patterning parameters of $w/L=g/L=0.025$

According to the obtained results, we also investigated the probability of obtaining helices by considering the heights and grating angles, while neglecting high w/g ratios. As depicted in Fig. 3.10. (b), at low grating depths, almost no helices are obtained except for an

angle of 60° . It can be concluded that at low depths, the grating structure is not effective enough to change the rolling behavior. However, as discussed above, low w/g can result in perfect helices while using at depths of 0.4 top layer, showing that the grating patterns positively affect the rolling direction. Increasing the depth to higher than half of the top layer mostly results in imperfect helices, meaning that the grating patterns are overused. The quality of the perfect helices produced by that depth also is not as smooth as that of 0.4 since the variation of the curvature in the grating and non-grating regions is more tangible. Higher w/g is not suitable since the chance of grating patterns to change over the rolling is lower because of the number of grating patterns through the length of the ribbon. However, at angles of 60° , where the aspect ratio of the grating and non-grating parts are high enough (consider the chord of the right triangle when one angle is increased), the structure has a higher chance to roll for the long edge (perpendicular to the long edge of the grating). For this reason, one can conclude that in lower w/g , medium depth, and high angles obtaining helical ribbons is guaranteed.

Fig. 3.12. depicts a comparison between the helices results obtained in experiments and the ones achieved by simulation. To this end, two series of helices (i.e. $H/T_{HF} = 0.4$ and 0.6) are considered for three various grating angles. For both series, the diameter of the helices stayed constant which is well predicted by the simulation with an average error of around 5%. As expected, by increasing the grating angle, one should obtain higher periodicity (λ), which is obtained in the experiment together with simulation with an average error of around 7%. In addition to this figure, Fig. 3.13. is also given to see how the simulation is able to predict both perfect helices and imperfect helical structures, in addition to compacted helices shown in Fig. 3.3. As it clear from Fig. 3.13. (a-c), and based on the explanation given for Fig. 3.12., we can see that how changing the grating angle affects the shape of the helices. Also, using a higher depth of grating can result in imperfect helices as demonstrated in Fig. 3.13. (d-f). For all cases, the simulation is capable of predicting the behavior of the structure from ribbon to helices. As a consequence, if the mechanical and material properties (e.g. stress inside each layer, elastic modulus, Poisson's ratio) and geometric dimensions (e.g. thickness of the thin films, length and width of mesas, and also grating parameters) are given properly, this method of simulation is able to be used as a tool to obtain robust designs before starting

the fabrication process. Hence, the fabrication would be cost-effective while the time of fabrication with several trials and errors would be decreased considerably.

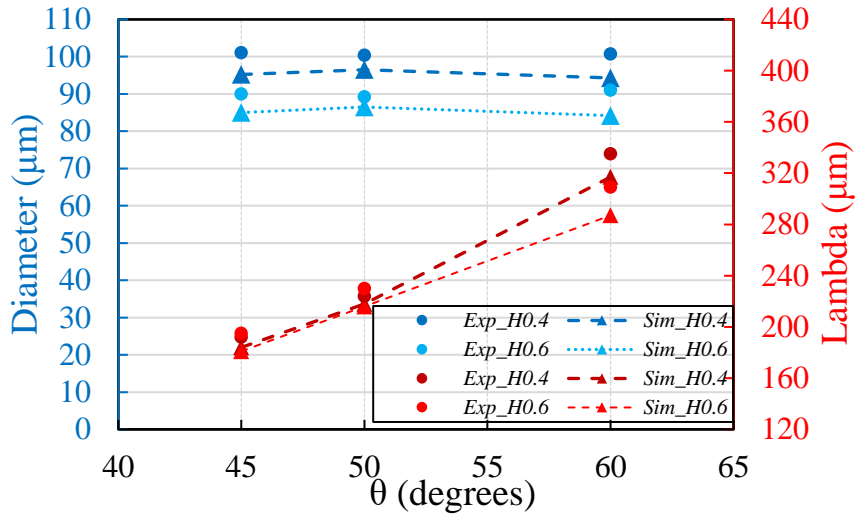


Fig. 3.12. Comparison between experimental and simulation results for grating parameters of $w/L=g/L=0.025$

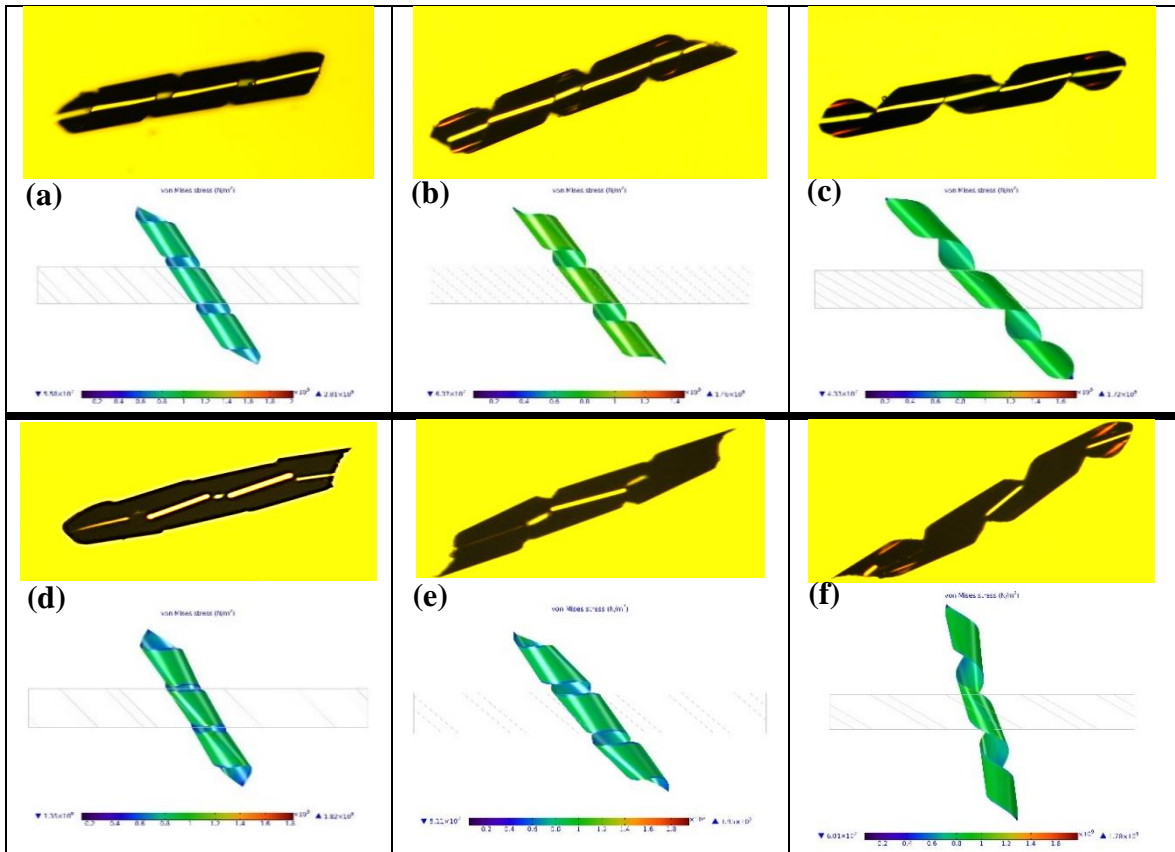


Fig. 3.13. Comparison between experimental and simulation results; (a) and (d) $\theta=45^\circ$, (b) and (e) $\theta=50^\circ$, (c) and (f) $\theta=60^\circ$. From a-c, $w/L=g/L=0.025$ while $H/T_{HF} = 0.4$, and from e-f, $g/L=0.025$, $w/L=0.1$ while $H/T_{HF} = 0.6$. For all cases $L=1050 \mu\text{m}$, and $W=120 \mu\text{m}$

3.3 Propulsion

In this section, the swimming behavior of the fabricated swimmers will be discussed. Basically, the coil's magnetic field strength, \mathbf{B} , is limited by currents. The bigger the magnetic moment, \mathbf{m} , the higher the torque generated as discussed in Eq. (2-16). Higher torque is useful to overcome the viscous torque, which scales linearly with the rotation rate. As a result, the swimmer with the bigger magnetic moment is capable of moving at higher frequencies. In order to increase the magnetization, we increased the thickness of nickel three times which results in a three times bigger volume of the magnetic material. moreover, by increasing the thickness, we basically increase the strength of the magnetization vector and the saturation field as well. As a conclusion, we expect an increase in the torque at least three times by increasing the thickness of the nickel nanolayer three times [129, 130]. Noted that, to make sure about how much the magnetization is change and as a result torque is increased, we needed a magnetometer equipment, like vibrating sample magnetometer (VSM) that we lack such equipment in our labs. Considering our method offered in section 3.2., we fabricated new sandwich swimmers with 150 nm nickel (i.e. 100 nm LF SiN_x/150 nm Ni/170 nm HF SiN_x) instead of 50 nm nickel.

The performance of such robots under a rotating magnetic field with a magnitude of 3.6 mT and acoustic field with an amplitude of 10 volts and various frequencies have been investigated and recorded. The experiments were repeated three times for each frequency to express the velocity vs frequency range defined by error bars. As a post-processing step, the videos were collected and analyzed through an image processing procedure using the code developed in our group. The extracted trajectories have been filtered by the Savitzky-Golay (S-Golay) filtering method with a frame length of 25 and an order of 3. This helped us to reach a suitable curve fitting to the obtained wavy-like curves without over-fitting. After that, the velocity of each frame has been calculated based on the convolution of the data and the first derivative coefficients given by the S-Golay filtering. Since the data comprise of both x and y coordinates together with the orientation of the swimmer, we have been able to achieve both the swimming velocity and the lateral velocity by a rotation matrix with the help of the orientation angle of the swimmers (α). For the velocity calculations, we first took the mean of

three sets of velocity data, and then, the error bars have been used considering the standard deviations for each set of data.



Fig. 3.14. The new swimmer with 150 nm sandwich nickel

In the experiments, we aimed to check the behavior of just one swimmer with a diameter of $60\ \mu\text{m}$, length of $740\ \mu\text{m}$, and wavelength of $246\ \mu\text{m}$ (shown in Fig. 3.14.). The experiments have been performed both inside a small tube with an inner diameter of $1.6\ \text{mm}$, and then a reservoir to observe the effect of both the rotating magnetic field and acoustic field on the velocity and the trajectory of the swimmer. The considered coordinate system for all experiments is represented in Fig. 3.15. Considering this figure, the swimmer's velocity is analyzed in two components according to the local coordinate frame: a) forward velocity (V_{sw1}) which represent the displacement of the swimmer with respect to time, based on the direction parallel to the helical axis of the swimmer; and b) lateral velocity (V_{sw2}) which means the displacement/time of the swimmer in a direction perpendicular to the helical axis.

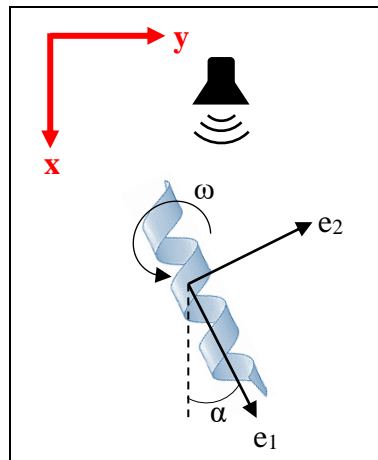


Fig. 3.15. Coordinate systems and the direction of swimming

3.3.1 Magnetic swimming performance in an mm-scale tube

The behavior of the swimmer in a small circular channel is, in a sense, different from the other big containers. In small containers, the swimmer tends to swim near the solid boundaries due to higher viscous drag near those regions. The motion behavior of our swimmers inside the small tube is analogous to its microorganism counterparts [25, 131] as demonstrated as a time-lapse image in Fig. 3.16., in which the swimmer rotates in the vicinity of the channel wall and moves alongside the length of the channel. In helical microswimmers, it has been observed that the swimmer shows a tumbling behavior at low magnetic frequencies, followed by cork-screw-like motion at fairly high frequencies [30, 132, 133]. The velocity with respect to the frequency has been reported as a linearly increasing curve up to a critical frequency, beyond which, the velocity reduces. This critical frequency is called step-out frequency at which the magnetic torque could not overcome the viscous resistance [25, 31, 133].

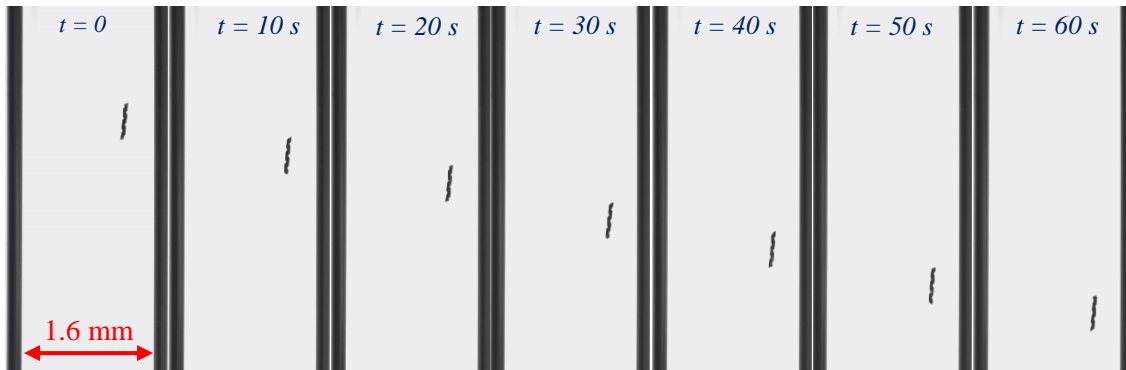


Fig. 3.16. Time-lapse image of the movement of the microswimmer through a circular channel at magnetic frequency of 5 Hz

In our swimmers, also, three regions have been observed as exhibited in Fig. 3.17. (a). Up to $f = 4$ Hz, the swimmer tumbles. For $4 \text{ Hz} < f < 17 \text{ Hz}$, the swimmer synchronizes to the magnetic field so that the speed of the swimmer linearly increases to reach a maximum of $110 \mu\text{m/s}$ corresponding to around 0.2 body length per second. After that, the swimmer enters the step-out region in which the rotation of the swimmer becomes irregular, resulting in a reduced velocity so that after 19 Hz the swimmer stopped moving. In addition to the forward velocity, we observed a movement perpendicular to the axis of the tube as well. This resulted in lateral velocity (V_{sw2}) shown in Fig. 3.17. (b) with respect to magnetic frequency. This velocity depends on several factors such as the radius of the channel, and the geometry of the helix [39]. The lateral drifting is believed to be due to the interaction with the walls [121]. In the

next section, we will see that this effect is more pronounced in the cuboid chamber. In Fig. 3.17. (c). it is clear that the swimmer inclines once swimming, specifically at higher frequencies. We believe that this deviation from the x-axis is due to the nonuniform magnetization of the swimmer. The effect of magnetization on the swimming of the swimmers with just helical tail coated with magnetic materials have been discussed before. However, it has been shown that in such robots first, they have a misalignment with the rotating magnetic field, and then, increasing the frequency helped them to be synchronized with the field [8, 12, 32, 133]. In our case, in which we used a helical magnetic thin film, however, this behavior has not been observed; instead, the swimmer first aligns with the rotating magnetic field, followed by misalignment at higher frequencies.

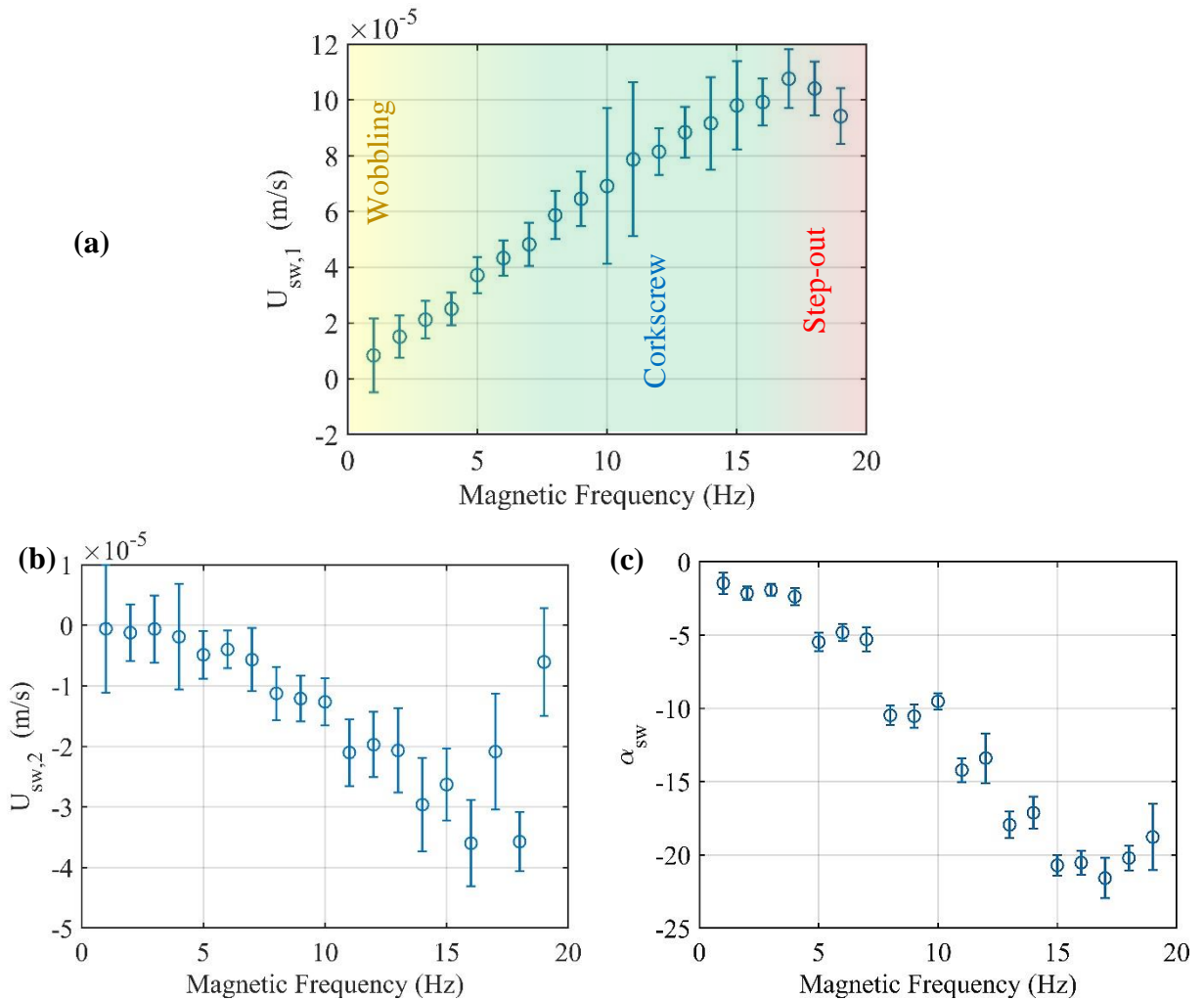


Fig. 3.17. swimming performance in a small tube. a) swimming velocity in the direction parallel to the helical axis, b) swimming velocity in the direction perpendicular to the helical axis, and c) the orientation angle of the swimmer

3.3.2 Magneto-acoustic swimming performance in a cuboid reservoir

In this section, the impact of both rotating magnetic field and acoustic field on the swimming performance of the swimmer will be examined. Without using acoustic actuation, the velocity-frequency curve has again three regions, i.e. wobbling, corkscrew, and step-out motion, like what was discussed in the previous section. However, since the swimmer swims near the glass surface, the effect of lateral drifting is more noticeable here. For this reason, in addition to the forward velocity, the swimmer exhibits significant lateral velocity as well. Fig. 3.18. is given to show the trajectory of the swimmer in a constant magnetic frequency and two different acoustic frequencies. When no acoustic field is applied to the swimmer, it tends to be inclined and move mostly in the lateral direction (y-direction). The forward and lateral velocities together with the swimmer orientation angles are demonstrated in Fig. 3.19. Up to $f = 4$ Hz, the swimmer shows a wobbling behavior, and after that, by increasing the frequency, all of the velocities and orientation angles increase. After $f = 14$ Hz, the swimmer enters the step-out regime. The maximum forward velocity is $125 \mu\text{m/s}$ which shows a small increase compared to what was achieved in the small tube; however, note that the maximum velocity obtained at a lower magnetic frequency here. Since the swimmer moves near the surface, we can see that the lateral velocity is much higher than that of the tube.

However, exerting an acoustic field cause the swimmer's distance to the surface to be increased. This allows the swimmer to be well-synchronized with the external magnetic field so that the orientation angle decreases, and as a result, the swimmer tends to move in the x-direction more. To this end, we used some kilohertz vibration ranges since the resonance frequencies of the utilized transducer are in kHz ranges at which the vibration modes are more pronounced [23]. Two frequencies with respect to the vibration modes of the whole structure as a doubly clamped configuration depicted in Fig. 3.20. To this end, a frequency-domain study in COMSOL has been employed and the modes of different frequencies less than 20 kHz have been investigated. The effect of two of them, 1kHz and 10kHz, has been reported since they show a considerable behavior in the amplitude of the modes: the maximum amplitude of 1 kHz is $220 \mu\text{m}$, and that of 10 kHz is $2.5 \mu\text{m}$. Both of these modes create traveling waves that would affect the distance of the swimmer to the surface. Sure enough, as depicted in Fig. 3.19. both velocities of the swimmer are improved by applying a vibration

frequency of 1 kHz. For instance, the step-out frequency goes beyond the $f = 14$ Hz that was obtained without acoustic actuation. It has resulted in maximum axial and lateral velocities of $240 \mu\text{m/s}$ and $270 \mu\text{m/s}$, respectively. On the other hand, the acoustic frequency of 10 kHz did not affect the swimming velocity too much. However, it affected the surface distance of the swimmer so that it can be synchronized well with the magnetic field for larger values of frequencies. It is worth mentioning that, the swimmer experiences the step-out for all cases once the orientation angle goes beyond 17 degrees. Hence, it can be concluded that the acoustic field increases the velocity by applying traveling waves to the swimmer while improving the orientation angle.

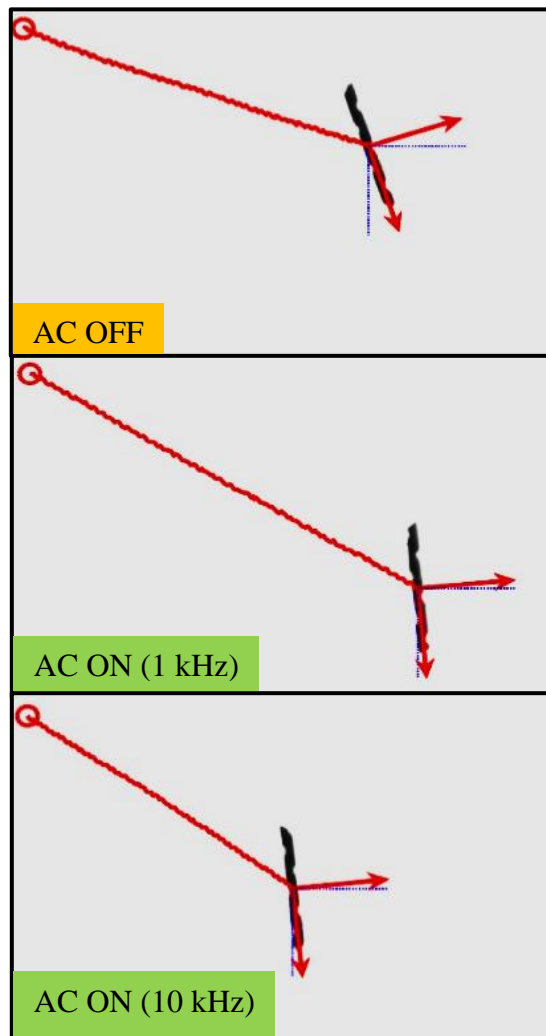


Fig. 3.18. Swimming trajectory under the magnetic frequency of 13 Hz

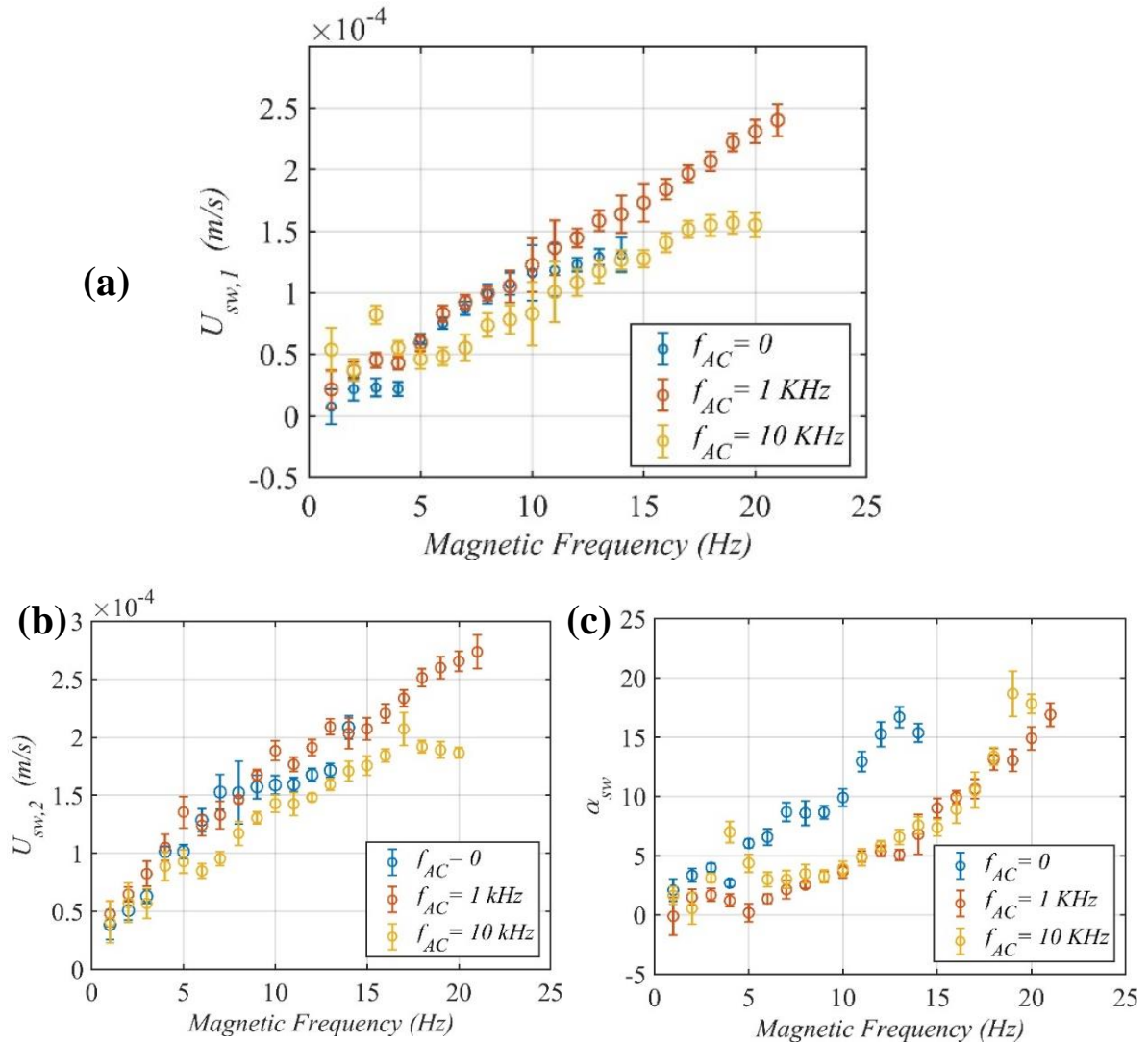


Fig. 3.19. Swimming performance under magneto-acoustic fields. A) forward velocities, b) lateral velocities, and c) orientation angles

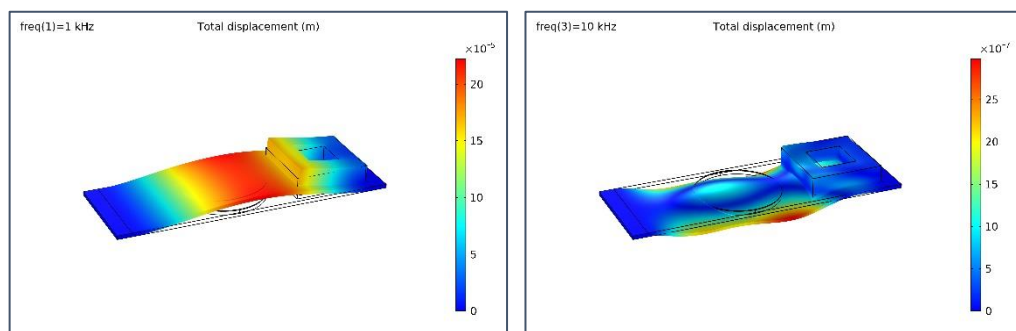


Fig. 3.20. Vibration modes for two acoustic frequencies, 1 kHz left, and 10 kHz right

4 CONCLUSIONS

Microswimming robots are recently emerging agents in biomedical applications. This dissertation is dedicated to fabrication, FEM modeling, and magneto-acoustic locomotion of helical multilayer microswimming robots. First, a specific method of microfabrication, i.e. self-assembly fabrication of non-crystalline nanomembranes is presented. To this end, bilayer and sandwich thin films are used with strain mismatch inside each layer. In noncrystalline nanomembranes in which the stress distribution and mechanical properties are isotropic, an additional step is required to force the structure to roll in a specific direction in order to take the form of helices. For this reason, two methods are proposed; 1) variation of aspect ratio and thickness, and 2) topography modification (grating). The first method demonstrates how the variation of aspect ratio can change over the rolling orientation of a bilayer (low frequency (LF) SiN_x /high frequency (HF) SiN_x). By applying some modifications in the top layer, however, this method is served as a technique to obtain helical structures. It is also expanded to create sandwich structures as well (LF SiN_x /Ni/HF SiN_x) which can be used as magnetized microswimming robots. However, since such a technique is demanding, so that requiring precise characterization, the other method is utilized to create microswimming robots. To this end, by developing several oriented slots through the structure, anisotropic stress distribution and anisotropic bending stiffness are imposed, leading to rolling in a direction in which energy minimization is more preferable. Hence, a characterization process is carried out by changing the grating parameters such as the width, gap, depth, and angle of the grating patterns. It is evident that using lower grating widths and gaps together with higher grating angles can lead to perfect helical structures. However, overusing or underusing of such parameters can affect negatively in obtaining helical structures.

In order to predict the behavior of rolling, several simulation procedures are proposed with the help of COMSOL V5.6. Considering 3D structural mechanics modules while taking the geometric nonlinearity into account. The rolling process is simulated by means of a bunch of boundary conditions inspired by the nature of rolling as observed through an optical camera. The stress mismatch is applied by defining various thermal expansion coefficients while changing the temperature. After a mesh study process, the results first are validated by

perfectly rolled up structures, followed by simulating the effect of aspect ratio in rolling. In the end, the helical structures generating from the grating method is molded, and the results are compared to those of experiments, which shows an error of less than 10% in all simulations.

The sandwich helical structures fabricated by the grating method, since containing nickel layer as a magnetic material, are served as microswimming robots that are remotely propelled by rotating magnetic field and acoustic field. To this end, first, a microswimmer with 150 nm nickel is fabricated and put under a permanent magnetic field of 0.5 T to be magnetized. After that, a Helmholtz coils setup, that has been previously prepared, produces an mT-scale magnetic field. The swimmer first is put inside a 1.6 mm circular channel full of isopropyl alcohol (IPA). Three motion regimes are obtained (wobbling at magnetic frequencies less than 4 Hz, corkscrew motion between 4 and 14 Hz, and step out motion at higher magnetic frequencies). Due to the effect of solid boundaries, the swimmer tends to move near the wall like its counterpart natural organisms. The maximum velocity of 0.2 body length per second is obtained, as well as a fairly small motion to the lateral side. The swimmer at high frequencies tilts which is most probably due to non-uniform magnetization. The swimming performance of the swimmer is also investigated in a cuboid PDMS reservoir. The forward velocity of the swimmer is fairly higher than that of the circular channel. The lateral velocity is more tangible in the reservoir since the swimmer has an interaction with the underneath wall which results in lateral drifting. To improve the velocity of the swimmer by generating traveling waves, an acoustic field is applied by an amplitude of 10 volts and two frequencies of 1 kHz and 10 kHz. Both frequencies help the swimmer to be synchronized with the magnetic field at higher magnetic frequencies. Both of the frequencies improve the velocity; however, the effect of 1 kHz acoustic waves is more pronounced due to the created stronger modes, so that the maximum velocity of 250 $\mu\text{m/s}$ and 275 $\mu\text{m/s}$ for the forward velocity and lateral velocity are obtained, respectively.

4.1 Future works

As future works, there are several improvements in fabrication, modeling, and propulsion that are discussed in the following.

- Fabrication

There are a couple of deficiencies in the first method of fabrication, by addressing of which the promising microswimming applications are feasible. For instance, if the helical structure is not anchored, although the modification is performed, however, it does not guarantee to obtain perfect helices. For this reason, a more extended study is required to investigate the effect of wrinkling modes, by modifying of which one will be able to reach consistency in obtaining helical microswimmers. On the controlling side of the helical parameters such as helical angles and periodicity together with the rolling diameter, a well-rounded characterization procedure is required to be aware of the effectiveness of changing the aspect ratio and thickness more accurately.

In the grating method, since a suitable investigation has been carried out, yet we need to develop it in order to obtain helices with much lower dimensions. One way to meet this aspiration is to create chromium photolithography masks with feature sizes less than a couple of microns. This mask should be accurately designed so that a smooth symmetry of the grating patterns through the surface of the mesas will be achievable. In terms of fabrication, although we tried to cover the nickel layer to improve its lifetime, however, there still a way for the liquids to penetrate this layer from the lateral sides. For this reason, we are ambitious about taking advantage of step coverage provided by plasma enhance chemical vapor deposition (PECVD) to cover the whole nickel layer. To get rid of the undercutting of nickel under wet etching process, two scenarios can be put forward: 1) using reactive ion etching (RIE) instead of wet etching (this requires a strong mask with high selectivity relative to the nickel layer. Metal masks are suitable options to do this mission), and 2) using a sacrificial layer that can be etched away readily in etchants that do not attack the nickel layer. For instance, resists are good options if no PECVD or PVD at high temperatures is used (instead of silicon nitride some other metals or dielectrics must be used or silicon nitride at low temperatures less than 200 °C can be deposited). Another example is using a germanium sacrificial layer that can be etched away easily in hydrogen peroxide since it does not attack nickel at all.

- Modeling and simulation

We tried to have a boundary condition as a carbon copy of the real releasing process. However, the intermediate states of the deformation are demanding to be observed by typical cameras as the process happens in less than a couple of milliseconds. For this reason, high-speed cameras are a suitable option to have a more comprehensive look at the deformation process.

Since the simulation process as a result of considering the geometric nonlinearity takes too long, so that performing a well-rounded characterization is arduous. For this reason, instead of using 3D models, one should use 2D models like layered shell models or plates. Another option is to use symmetry modules to just model half of the structure. Another option would be increasing the loads step by step as a parametric study. We tried some of them like layered shell models, however, the time of solving did not change considerably. Further study is required to be performed to improve this kind of model like applying special constraints such as contacts between each layers. ABAQUS software may be helpful to define such constraints more precisely as well.

- Propulsion

The first thing in the locomotion of the microswimmers is to make sure that they are magnetized properly under a uniform magnetic field. To obtain the magnetic properties of the swimmer, it has to put into a vibrating sample magnetometer (VSM) instrument. This will help us to investigate the behavior of the swimmer more profoundly.

The housing of the Helmholtz coils is fabricated by 3D printing materials that are extremely susceptible to heat changes, such that it can be easily deformed at temperatures higher than 80 °C. This problem hindered us to increase the current to obtain higher torques and better performance at high magnetic frequencies. A new design of such coils is required as a result. The alternative materials for the coil can be plexiglass, or in an ambitious case, we may design a frame so that the coils are free of any housing, which improves the heat transfer inside the coils. Another way is to design a frame and implement powerful fans to keep the temperature of coils down to the ambient temperature.

Although helpful, however, the disk piezo transducers unable to provide powerful traveling waves. To make it more powerful, one may increase the amplitude by an amplifier. However, in the setup that we used, the microscope glass is susceptible to be broken at high amplitudes. One way to improve their performance is to change over the setup in which no glass is utilized. Another option is to use focus transducers that can be suspended in a way to convey the energy directly to the liquid. Surface modification of the chamber would be another possibility; for instance, creating some roughness in the walls of the reservoirs or creating slots through the surface.

We investigated a small number of frequencies with respect to the modes created as a result of vibrating the setup. One may expand this range of frequencies and see the performance of the swimmer. There is likely to be an optimized frequency to obtain the best performance. In addition, the boundary condition can be changed to see the effects of the vibration modes on the swimming performance.

Bibliography

- [1] Li J and Pumera M 2021 3D printing of functional microrobots *Chemical Society Reviews* **50** 2794-838
- [2] Gao W, Feng X, Pei A, Kane C R, Tam R, Hennessy C and Wang J 2014 Bioinspired helical microswimmers based on vascular plants *Nano letters* **14** 305-10
- [3] Tian H, Liu H, Shao J, Li S, Li X and Chen X 2020 An electrically active gecko-effect soft gripper under a low voltage by mimicking gecko's adhesive structures and toe muscles *Soft Matter* **16** 5599-608
- [4] Ceylan H, Giltinan J, Kozielski K and Sitti M 2017 Mobile microrobots for bioengineering applications *Lab on a Chip* **17** 1705-24
- [5] Tabak A F and Yesilyurt S 2012 Experiment-based kinematic validation of numeric modeling and simulated control of an untethered biomimetic microrobot in channel. In: *2012 12th IEEE International Workshop on Advanced Motion Control (AMC)*: IEEE) pp 1-6
- [6] Zhang L, Peyer K E and Nelson B J 2010 Artificial bacterial flagella for micromanipulation *Lab on a Chip* **10** 2203-15
- [7] Nelson B J, Kaliakatsos I K and Abbott J J 2010 Microrobots for minimally invasive medicine *Annual review of biomedical engineering* **12** 55-85
- [8] Ceylan H, Yasa I C, Yasa O, Tabak A F, Giltinan J and Sitti M 2019 3D-printed biodegradable microswimmer for theranostic cargo delivery and release *ACS nano* **13** 3353-62
- [9] Chen X-Z, Liu J-H, Dong M, Müller L, Chatzipirpiridis G, Hu C, Terzopoulou A, Torlaccik H, Wang X and Mushtaq F 2019 Magnetically driven piezoelectric soft microswimmers for neuron-like cell delivery and neuronal differentiation *Materials Horizons* **6** 1512-6
- [10] Wu J, Balasubramanian S, Kagan D, Manesh K M, Campuzano S and Wang J 2010 Motion-based DNA detection using catalytic nanomotors *Nature Communications* **1** 1-6
- [11] Zhou H, Mayorga-Martinez C C, Pané S, Zhang L and Pumera M 2021 Magnetically Driven Micro and Nanorobots *Chemical Reviews*
- [12] Abbott J J, Peyer K E, Lagomarsino M C, Zhang L, Dong L, Kaliakatsos I K and Nelson B J 2009 How should microrobots swim? *The international journal of Robotics Research* **28** 1434-47
- [13] Berg H C and Anderson R A 1973 Bacteria swim by rotating their flagellar filaments *Nature* **245** 380-2
- [14] Nakamura S and Islam M S 2017 *The Bacterial Flagellum: Methods and Protocols*, ed T Minamino and K Namba (New York, NY: Springer New York) pp 243-51
- [15] Charon N W, Cockburn A, Li C, Liu J, Miller K A, Miller M R, Motaleb M A and Wolgemuth C W 2012 The unique paradigm of spirochete motility and chemotaxis *Annual review of microbiology* **66** 349-70
- [16] Gray J and Hancock G 1955 The propulsion of sea-urchin spermatozoa *Journal of Experimental Biology* **32** 802-14
- [17] Wu Z, Chen Y, Mukasa D, Pak O S and Gao W 2020 Medical micro/nanorobots in complex media *Chemical Society Reviews* **49** 8088-112
- [18] Stanton M M, Park B W, Miguel-López A, Ma X, Sitti M and Sánchez S 2017 Biohybrid microtube swimmers driven by single captured bacteria *Small* **13** 1603679
- [19] Alapan Y, Yasa O, Yigit B, Yasa I C, Erkoc P and Sitti M 2019 Microrobotics and microorganisms: Biohybrid autonomous cellular robots *Annual Review of Control, Robotics, and Autonomous Systems* **2** 205-30
- [20] Bunea A I, Martella D, Nocentini S, Parmeggiani C, Taboryski R and Wiersma D S 2021 Light-Powered Microrobots: Challenges and Opportunities for Hard and Soft Responsive Microswimmers *Advanced Intelligent Systems* 2000256
- [21] Tahara H, Takabe K, Sasaki Y, Kasuga K, Kawamoto A, Koizumi N and Nakamura S 2018 The mechanism of two-phase motility in the spirochete *Leptospira*: Swimming and crawling *Science advances* **4** eaar7975
- [22] Schenck J F 2000 Safety of strong, static magnetic fields *Journal of magnetic resonance imaging* **12** 2-19

- [23] Ahmed D, Baasch T, Jang B, Pane S, Dual J and Nelson B J 2016 Artificial swimmers propelled by acoustically activated flagella *Nano letters* **16** 4968-74
- [24] Li J, Li T, Xu T, Kiristi M, Liu W, Wu Z and Wang J 2015 Magneto–acoustic hybrid nanomotor *Nano letters* **15** 4814-21
- [25] Zhang L, Abbott J J, Dong L, Peyer K E, Kratochvil B E, Zhang H, Bergeles C and Nelson B J 2009 Characterizing the swimming properties of artificial bacterial flagella *Nano letters* **9** 3663-7
- [26] Bell D J, Leutenegger S, Hammar K, Dong L X and Nelson B J 2007 Flagella-like propulsion for microrobots using a nanocoil and a rotating electromagnetic field. In: *Proceedings 2007 IEEE international conference on robotics and automation: IEEE*) pp 1128-33
- [27] Caldag H O, Acemoglu A and Yesilyurt S 2017 Experimental characterization of helical swimming trajectories in circular channels *Microfluidics and Nanofluidics* **21** 1-13
- [28] Zhang L, Abbott J J, Dong L, Kratochvil B E, Bell D and Nelson B J 2009 Artificial bacterial flagella: Fabrication and magnetic control *Applied Physics Letters* **94** 064107
- [29] Nakamura S and Islam M S 2017 *The Bacterial Flagellum*: Springer) pp 243-51
- [30] Li J, Sattayasamitsathit S, Dong R, Gao W, Tam R, Feng X, Ai S and Wang J 2014 Template electrosynthesis of tailored-made helical nanoswimmers *Nanoscale* **6** 9415-20
- [31] Tottori S, Zhang L, Peyer K E and Nelson B J 2013 Assembly, disassembly, and anomalous propulsion of microscopic helices *Nano letters* **13** 4263-8
- [32] Tottori S, Zhang L, Qiu F, Krawczyk K K, Franco-Obregón A and Nelson B J 2012 Magnetic helical micromachines: fabrication, controlled swimming, and cargo transport *Advanced materials* **24** 811-6
- [33] Chatzipirpiridis G, de Marco C, Pellicer E, Ergeneman O, Sort J, Nelson B J and Pané S 2018 Template-Assisted Electroforming of Fully Semi-Hard-Magnetic Helical Microactuators *Advanced Engineering Materials* **20** 1800179
- [34] Peters C, Hoop M, Pané S, Nelson B J and Hierold C 2016 Degradable magnetic composites for minimally invasive interventions: Device fabrication, targeted drug delivery, and cytotoxicity tests *Advanced Materials* **28** 533-8
- [35] Huang G and Mei Y 2015 Helices in micro-world: Materials, properties, and applications *Journal of Materiomics* **1** 296-306
- [36] Acemoglu A and Yesilyurt S 2015 Effects of poiseuille flows on swimming of magnetic helical robots in circular channels *Microfluidics and Nanofluidics* **19** 1109-22
- [37] Caldag H O and Yesilyurt S 2019 Trajectories of magnetically-actuated helical swimmers in cylindrical channels at low Reynolds numbers *Journal of Fluids and Structures* **90** 164-76
- [38] Caldag H O, Acemoglu A and Yesilyurt S 2017 Experimental characterization of helical swimming trajectories in circular channels *Microfluidics and Nanofluidics* **21** 136
- [39] Acemoglu A and Yesilyurt S 2014 Effects of geometric parameters on swimming of micro organisms with single helical flagellum in circular channels *Biophysical journal* **106** 1537-47
- [40] Vrakatseli V E, Kalarakis A N, Kalamponias A G, Amanatides E K and Mataras D S 2018 Glancing angle deposition effect on structure and light-induced wettability of RF-sputtered TiO₂ thin films *Micromachines* **9** 389
- [41] Hawkeye M M and Brett M J 2007 Glancing angle deposition: fabrication, properties, and applications of micro- and nanostructured thin films *Journal of Vacuum Science & Technology A: Vacuum, Surfaces, and Films* **25** 1317-35
- [42] Huang Z and Bai F 2014 Wafer-scale, three-dimensional helical porous thin films deposited at a glancing angle *Nanoscale* **6** 9401-9
- [43] Robbie K, Brett M and Lakhtakia A 1996 Chiral sculptured thin films *Nature* **384** 616-
- [44] Robbie K and Brett M 1997 Sculptured thin films and glancing angle deposition: Growth mechanics and applications *Journal of Vacuum Science & Technology A: Vacuum, Surfaces, and Films* **15** 1460-5
- [45] Ghosh A and Fischer P 2009 Controlled propulsion of artificial magnetic nanostructured propellers *Nano letters* **9** 2243-5
- [46] Zhang X, Zhang X, Bernaerts D, Van Tendeloo G, Amelinckx S, Van Landuyt J, Ivanov V, Nagy J B, Lambin P and Lucas A 1994 The texture of catalytically grown coil-shaped carbon nanotubes *EPL (Europhysics Letters)* **27** 141
- [47] Lu M, Li H-L and Lau K-T 2004 Formation and growth mechanism of dissimilar coiled carbon nanotubes by reduced-pressure catalytic chemical vapor deposition *The Journal of Physical Chemistry B* **108** 6186-92

- [48] Amelinckx S, Zhang X, Bernaerts D, Zhang X, Ivanov V and Nagy J 1994 A formation mechanism for catalytically grown helix-shaped graphite nanotubes *Science* **265** 635-9
- [49] Wang W, Yang K, Gaillard J, Bandaru P R and Rao A M 2008 Rational synthesis of helically coiled carbon nanowires and nanotubes through the use of tin and indium catalysts *Advanced Materials* **20** 179-82
- [50] Bandaru P, Daraio C, Yang K and Rao A 2007 A plausible mechanism for the evolution of helical forms in nanostructure growth *Journal of Applied Physics* **101** 094307
- [51] Zhang H-F, Wang C-M and Wang L-S 2002 Helical crystalline SiC/SiO₂ core– shell nanowires *Nano letters* **2** 941-4
- [52] Zhang H-F, Wang C-M, Buck E C and Wang L-S 2003 Synthesis, characterization, and manipulation of helical SiO₂ nanosprings *Nano Letters* **3** 577-80
- [53] Wang Y, Xu J, Wang Y and Chen H 2013 Emerging chirality in nanoscience *Chemical Society Reviews* **42** 2930-62
- [54] Han T, Reneker D H and Yarin A L 2007 Buckling of jets in electrospinning *Polymer* **48** 6064-76
- [55] Yu J, Qiu Y, Zha X, Yu M, Yu J, Rafique J and Yin J 2008 Production of aligned helical polymer nanofibers by electrospinning *European Polymer Journal* **44** 2838-44
- [56] Shariatpanahi S, Abdollahzadeh I, Shirsavar R, Bonn D and Eftehadi R 2011 Micro helical polymeric structures produced by variable voltage direct electrospinning *Soft Matter* **7** 10548-51
- [57] Zhao Y, Miao X, Lin J, Li X, Bian F, Wang J, Zhang X and Yue B 2017 Coiled Plant Tendril Bioinspired Fabrication of Helical Porous Microfibers for Crude Oil Cleanup *Global Challenges* **1** 1600021
- [58] Farrar D, Ren K, Cheng D, Kim S, Moon W, Wilson W L, West J E and Yu S M 2011 Permanent polarity and piezoelectricity of electrospun α -helical poly (α -amino acid) fibers *Advanced Materials* **23** 3954-8
- [59] Prinz V Y, Seleznev V, Gutakovskiy A, Chehovskiy A, Preobrazhenskii V, Putyato M and Gavrilova T 2000 Free-standing and overgrown InGaAs/GaAs nanotubes, nanohelices and their arrays *Physica E: Low-dimensional Systems and Nanostructures* **6** 828-31
- [60] Zanardi Ocampo J M, Vaccaro P O, Fleischmann T, Wang T-S, Kubota K, Aida T, Ohnishi T, Sugimura A, Izumoto R and Hosoda M 2003 Optical actuation of micromirrors fabricated by the micro-origami technique *Applied physics letters* **83** 3647-9
- [61] Chun I S and Li X 2008 Controlled assembly and dispersion of strain-induced InGaAs/GaAs nanotubes *IEEE Transactions on Nanotechnology* **7** 493-5
- [62] Yu M, Huang Y, Ballweg J, Shin H, Huang M, Savage D E, Lagally M G, Dent E W, Blick R H and Williams J C 2011 Semiconductor nanomembrane tubes: three-dimensional confinement for controlled neurite outgrowth *ACS nano* **5** 2447-57
- [63] Golod S, Prinz V Y, Wägli P, Zhang L, Kirfel O, Deckhardt E, Glaus F, David C and Grützmacher D 2004 Freestanding SiGe/Si/Cr and SiGe/Si/Si_xN_y/Cr microtubes *Applied physics letters* **84** 3391-3
- [64] Golod S, Prinz V Y, Mashanov V and Gutakovskiy A 2001 Fabrication of conducting GeSi/Si micro- and nanotubes and helical microcoils *Semiconductor Science and Technology* **16** 181
- [65] Prinz V Y and Golod S 2006 Elastic silicon-film-based nanoshells: formation, properties, and applications *Journal of applied mechanics and technical physics* **47** 867-78
- [66] Seleznev V, Prinz V Y, Aniskin V and Maslov A 2009 Generation and registration of disturbances in a gas flow. 1. Formation of arrays of tubular microheaters and microsensors *Journal of applied mechanics and technical physics* **50** 291-6
- [67] Mei Y, Huang G, Solovev A A, Ureña E B, Mönch I, Ding F, Reindl T, Fu R K, Chu P K and Schmidt O G 2008 Versatile approach for integrative and functionalized tubes by strain engineering of nanomembranes on polymers *Advanced Materials* **20** 4085-90
- [68] Schulze S, Huang G, Krause M, Aubyn D, Quiñones V A B, Schmidt C K, Mei Y and Schmidt O G 2010 Morphological differentiation of neurons on microtopographic substrates fabricated by rolled-up nanotechnology *Advanced Engineering Materials* **12** B558-B64
- [69] Huang W, Koric S, Yu X, Hsia K J and Li X 2014 Precision structural engineering of self-rolled-up 3D nanomembranes guided by transient quasi-static FEM modeling *Nano letters* **14** 6293-7
- [70] Stoychev G, Zakharchenko S, Turcaud S, Dunlop J W and Ionov L 2012 Shape-programmed folding of stimuli-responsive polymer bilayers *ACS nano* **6** 3925-34
- [71] Huang T, Liu Z, Huang G, Liu R and Mei Y 2014 Grating-structured metallic microsprings *Nanoscale* **6** 9428-35

- [72] Michaels J A, Wood D R, Froeter P J, Huang W, Sievers D J and Li X 2019 Effect of Perforation on the Thermal and Electrical Breakdown of Self-Rolled-Up Nanomembrane Structures *Advanced Materials Interfaces* **6** 1901022
- [73] Yang Z, Kraman M D, Zheng Z, Zhao H, Zhang J, Gong S, Shao Y V, Huang W, Wang P and Li X 2020 Monolithic Heterogeneous Integration of 3D Radio Frequency L– C Elements by Self-Rolled-Up Membrane Nanotechnology *Advanced Functional Materials* 2004034
- [74] Sang L, Zhou H, Yang Z, Kraman M D, Zhao H, Michaels J A, Sievers D J, Schutt-Aine J E, Li X and Huang W 2019 Monolithic radio frequency SiN x self-rolled-up nanomembrane interdigital capacitor modeling and fabrication *Nanotechnology* **30** 364001
- [75] Huang W, Zhou J, Froeter P, Walsh K, Liu S, Michaels J, Li M, Gong S and Li X 2017 CMOS-compatible on-chip self-rolled-up inductors for RF/mm-wave applications. In: *2017 IEEE MTT-S International Microwave Symposium (IMS): IEEE* pp 1645-8
- [76] Huang W, Zhou J, Froeter P J, Walsh K, Liu S, Kraman M D, Li M, Michaels J A, Sievers D J and Gong S 2018 Three-dimensional radio-frequency transformers based on a self-rolled-up membrane platform *Nature Electronics* **1** 305-13
- [77] Dai L and Zhang L 2013 Directional scrolling of SiGe/Si/Cr nanoribbon on Si (111) surfaces controlled by two-fold rotational symmetry underetching *Nanoscale* **5** 971-6
- [78] Zhang L, Deckhardt E, Weber A, Schönenberger C and Grützmacher D 2005 Controllable fabrication of SiGe/Si and SiGe/Si/Cr helical nanobelts *Nanotechnology* **16** 655
- [79] Tian Z, Huang W, Xu B, Li X and Mei Y 2018 Anisotropic rolling and controlled chirality of nanocrystalline diamond nanomembranes toward biomimetic helical frameworks *Nano letters* **18** 3688-94
- [80] Tian Z, Zhang L, Fang Y, Xu B, Tang S, Hu N, An Z, Chen Z and Mei Y 2017 Deterministic self-rolling of ultrathin nanocrystalline diamond nanomembranes for 3D tubular/helical architecture *Advanced Materials* **29** 1604572
- [81] Cui J, Adams J G and Zhu Y 2018 Controlled bending and folding of a bilayer structure consisting of a thin stiff film and a heat shrinkable polymer sheet *Smart Materials and Structures* **27** 055009
- [82] Guo Q, Zheng H, Chen W and Chen Z 2014 Modeling bistable behaviors in morphing structures through finite element simulations *Bio-medical materials and engineering* **24** 557-62
- [83] Guo Q, Zheng H, Chen W and Chen Z 2013 Finite element simulations on mechanical self-assembly of biomimetic helical structures *Journal of Mechanics in Medicine and Biology* **13** 1340018
- [84] Chen Z 2014 Geometric nonlinearity and mechanical anisotropy in strained helical nanoribbons *Nanoscale* **6** 9443-7
- [85] Chen Z, Guo Q, Majidi C, Chen W, Srolovitz D J and Haataja M P 2012 Nonlinear geometric effects in mechanical bistable morphing structures *Physical review letters* **109** 114302
- [86] Chen C, Song P, Meng F, Li X, Liu X and Song J 2017 Quantitative analysis and predictive engineering of self-rolling of nanomembranes under anisotropic mismatch strain *Nanotechnology* **28** 485302
- [87] Chun I S, Challa A, Derickson B, Hsia K J and Li X 2010 Geometry effect on the strain-induced self-rolling of semiconductor membranes *Nano letters* **10** 3927-32
- [88] Chen C, Song P, Meng F, Ou P, Liu X and Song J 2018 Effect of topological patterning on self-rolling of nanomembranes *Nanotechnology* **29** 345301
- [89] Xu B, Zhang X, Tian Z, Han D, Fan X, Chen Y, Di Z, Qiu T and Mei Y 2019 Microdroplet-guided intercalation and deterministic delamination towards intelligent rolling origami *Nature communications* **10**
- [90] Xu L, Gong D, Chen K, Cai J and Zhang W 2020 Acoustic levitation applied for reducing undesired lateral drift of magnetic helical microrobots *Journal of Applied Physics* **128** 184703
- [91] Dow H S, Kim W S and Lee J W 2017 Thermal and electrical properties of silicon nitride substrates *AIP Advances* **7** 095022
- [92] Dun H, Pan P, White F R and Douse R W 1981 Mechanisms of Plasma-Enhanced Silicon Nitride Deposition Using SiH₄/N₂ Mixture *Journal of the Electrochemical Society* **128** 1555
- [93] Nishidate Y and Nikishkov G P 2006 Generalized plane strain deformation of multilayer structures with initial strains *Journal of Applied physics* **100** 113518
- [94] Mahoney A W, Sarrazin J C, Bamberg E and Abbott J J 2011 Velocity control with gravity compensation for magnetic helical microswimmers *Advanced Robotics* **25** 1007-28
- [95] Li W, Kang Z, Ye Y and Jiang Y 2010 Influences of process parameters of low frequency PECVD technology on intrinsic stress of silicon nitride thin film. In: *5th International Symposium on Advanced*

- Optical Manufacturing and Testing Technologies: Optoelectronic Materials and Devices for Detector, Imager, Display, and Energy Conversion Technology*: International Society for Optics and Photonics) p 765824
- [96] Henrie J, Kellis S, Schultz S M and Hawkins A 2004 Electronic color charts for dielectric films on silicon *Optics express* **12** 1464-9
- [97] Ardigo M R, Ahmed M and Besnard A 2014 Stoney formula: Investigation of curvature measurements by optical profilometer. In: *Advanced Materials Research*: Trans Tech Publ) pp 361-6
- [98] Metzler M and Patel R 2017 Plasma Enhanced Chemical Vapor Deposition (PECVD) of Silicon Dioxide (SiO₂) Using Oxford Instruments System 100 PECVD
- [99] Nelson N, Rakowski R, Franks J, Woolliams P, Weaver P and Jones B 2014 The effect of substrate geometry and surface orientation on the film structure of DLC deposited using PECVD *Surface and Coatings Technology* **254** 73-8
- [100] Iliescu C, Avram M, Chen B, Popescu A, Dumitrescu V, Poenar D, Sterian A, Vrtacnik D, Amon S and Sterian P 2011 Residual stress in thin films PECVD depositions *Journal of Optoelectronics and Advanced Materials* **13** 387-94
- [101] Ye J, Chen Q and Zheng Y 2008 Magnetic properties of nickel film formed under magnetic fields *Journal of Physics D: Applied Physics* **41** 205011
- [102] Savić S M, Tadić M, Jagličić Z, Vojisavljević K, Mancic L and Branković G 2014 Structural, electrical and magnetic properties of nickel manganite obtained by a complex polymerization method *Ceramics International* **40** 15515-21
- [103] Corell D, Ou H, Dam-Hansen C, Petersen P-M and Friis D 2009 Light emitting diodes as an alternative ambient illumination source in photolithography environment *Optics Express* **17** 17293-302
- [104] Williams K R, Gupta K and Wasilik M 2003 Etch rates for micromachining processing-Part II *Journal of microelectromechanical systems* **12** 761-78
- [105] Walker P and Tarn W H 1990 *CRC handbook of metal etchants*: CRC press)
- [106] Schulz A, Häberle E, Walker M and Stroth U DETECTION AND IDENTIFICATION OF PINHOLES IN PECVD THIN FILM BARRIER COATINGS
- [107] Martins J A and Romão E C 2016 Analyzing 2D segment by Multiphysics in heat transfer and solid mechanics, pondering variables by Design of Experiment (DOE) *Engineering Science and Technology, an International Journal* **19** 1929-35
- [108] <https://doc.comsol.com/5.6/doc/com.comsol.help.sme/StructuralMechanicsModuleUsersGuide.pdf>
- [109] <https://www.comsol.com/blogs/heat-transfer-deformed-solids/>
- [110] <https://www.comsol.com/multiphysics/analysis-of-deformation>
- [111] <https://www.comsol.com/multiphysics/stress-and-equations-of-motion>
- [112] Chason E and Guduru P R 2016 Tutorial: Understanding residual stress in polycrystalline thin films through real-time measurements and physical models *Journal of Applied Physics* **119** 191101
- [113] Nix W 2014 *Metallic Films for Electronic, Optical and Magnetic Applications*: Elsevier) pp 353-421
- [114] Tabata O, Kawahata K, Sugiyama S and Igarashi I 1989 Mechanical property measurements of thin films using load-deflection of composite rectangular membranes *Sensors and actuators* **20** 135-41
- [115] Guyot N, Harmand Y and Mézin A 2004 The role of the sample shape and size on the internal stress induced curvature of thin-film substrate systems *International journal of solids and structures* **41** 5143-54
- [116] Sadeghian H, Yang C, Goosen J, Van Der Drift E, Bossche A, French P and Van Keulen F 2009 Characterizing size-dependent effective elastic modulus of silicon nanocantilevers using electrostatic pull-in instability *Applied Physics Letters* **94** 221903
- [117] Zhou L and Huang H 2003 Young's Modulus Variation with Thickness of Thin Films *MRS Online Proceedings Library Archive* **795**
- [118] Ao Z and Li S 2011 Temperature-and thickness-dependent elastic moduli of polymer thin films *Nanoscale research letters* **6** 1-6
- [119] Fedorchenko A I, Wang A-B and Cheng H H 2009 Thickness dependence of nanofilm elastic modulus *Applied Physics Letters* **94** 152111
- [120] Çaldağ H O 2016 Characterization of trajectories of magnetically actuated microswimmers with helical tails in circular channels.
- [121] Qiu F and Nelson B J 2015 Magnetic helical micro-and nanorobots: Toward their biomedical applications *Engineering* **1** 021-6

- [122] Nagy Z, Ergeneman O, Abbott J J, Hutter M, Hirt A M and Nelson B J 2008 Modeling assembled-MEMS microrobots for wireless magnetic control. In: *2008 IEEE International Conference on Robotics and Automation: IEEE*) pp 874-9
- [123] Cendula P, Kiravittaya S, Mönch I, Schumann J and Schmidt O G 2011 Directional roll-up of nanomembranes mediated by wrinkling *Nano letters* **11** 236-40
- [124] Cendula P, Kiravittaya S, Mei Y, Deneke C and Schmidt O 2009 Bending and wrinkling as competing relaxation pathways for strained free-hanging films *Physical Review B* **79** 085429
- [125] Froeter P, Huang Y, Cangellaris O V, Huang W, Dent E W, Gillette M U, Williams J C and Li X 2014 Toward intelligent synthetic neural circuits: directing and accelerating neuron cell growth by self-rolled-up silicon nitride microtube array *ACS nano* **8** 11108-17
- [126] Deneke C, Müller C, Jin-Phillipp N and Schmidt O 2002 Diameter scalability of rolled-up In (Ga) As/GaAs nanotubes *Semiconductor science and technology* **17** 1278
- [127] Huang M, Rugheimer P, Lagally M and Liu F 2005 Bending of nanoscale ultrathin substrates by growth of strained thin films and islands *Physical Review B* **72** 085450
- [128] Timoshenko S 1925 Analysis of bi-metal thermostats *Josa* **11** 233-55
- [129] Hemmous M, Layadi A, Kerkache L, Tiercelin N, Preobrazhensky V and Pernod P 2015 Magnetic properties of evaporated Ni thin films: effect of substrates, thickness, and Cu underlayer *Metallurgical and Materials Transactions A* **46** 4143-9
- [130] Hasan M, Shafi M, Siddiquy M, Rahim M and Islam M 2016 Electrical, Magnetic and Morphological Properties of E-Beam Evaporated Ni Thin Films *Journal of Scientific Research* **8** 21-8
- [131] Lauga E, DiLuzio W R, Whitesides G M and Stone H A 2006 Swimming in circles: motion of bacteria near solid boundaries *Biophysical journal* **90** 400-12
- [132] Li T, Li J, Morozov K I, Wu Z, Xu T, Rozen I, Leshansky A M, Li L and Wang J 2017 Highly efficient freestyle magnetic nanoswimmer *Nano letters* **17** 5092-8
- [133] Morozov K I and Leshansky A M 2014 The chiral magnetic nanomotors *Nanoscale* **6** 1580-8

APPENDIX

Fabrication Recipe

The fabrication processes flow is depicted in Fig. A1, which is divided into two main fabrication techniques (i.e., bottom-up fabrication and top-down fabrication). In the following the steps of fabrication is elaborated.

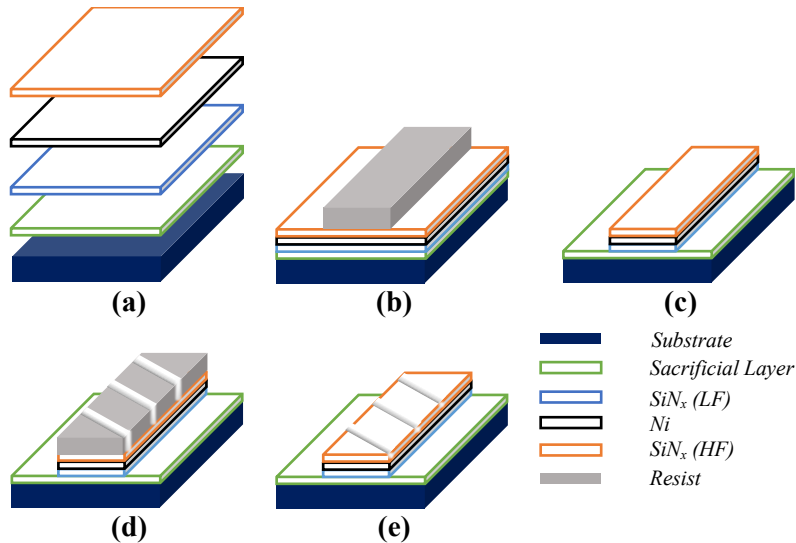


Fig. A1. Process flow of fabrication of self-rolled up helical structure: a) bottom-up deposition, b) the first lithography, c) consecutively RIE, wet etching, and RIE, d) the second lithography, and e) RIE

a) Bottom-up deposition

Substrate: 4 inch bare silicon ($500 \pm 10 \mu\text{m}$) or Si/SiO₂ (thermally grown) to have a clean and uniform substrate

Sacrificial layer: Fresh chromium pellets are put inside a tungsten crucible. The chamber of PVD has to be clean without any particles. The vacuum should reach 5×10^{-6} mTorr and the electron beam focus on the middle of the crucible. Increase the current very smoothly and wait a minute to let the oxides evaporated. Open the shutter and set the current so that to reach a deposition rate of $2.5 \text{ \AA}/\text{sec}$. The temperature of the substrate has not to exceed $25 \text{ }^\circ\text{C}$. After 250 nm thickness the shutter is closed and the current slows down step by step. After breaking the vacuum, the sample should be kept in a clean petri dish while it is sealed by parafilm.

LF SiN_x: Before performing the main deposition process, the chamber has to be cleaned by the specific recipe of the device. First, a trial deposition is carried out on a dummy wafer with

similar deposition time of the main deposition. After that, the main sample is put inside the device by using the recipe mentioned below, which result in around 160 nm of LF SiN_x in 20 minutes.

Table A1. PECVD Recipe for LF SiN_x

Temperature	Power	Pressure	Frequency	5%SiH ₄ /N ₂	NH ₃	N ₂
300 [°C]	20 [W]	650 [mTorr]	380 [kHz]	400 [sccm]	20 [sccm]	600 [sccm]

Nickel deposition: The recipe is exactly the same as for sacrificial layer. However, nickel is a ferromagnetic material that is actuated by the magnetic field inside the E-Beam PVD device. So, if using fresh pellets, one need to ramp up the current slowly and wait for a half an hour to allow the melted nickel to be stabilized. After that, the deposition process can be carried out.

HF SiN_x: The process of deposition is exactly the same as what mentioned for LF SiN_x. However, the low frequency power should be kept off. The process of fabrication is done for 24 minutes resulting in around 310 nm.

b) First Lithography

Fresh AZ5214E photoresist (PR) is poured on the surface of the wafer using a plastic pipet smoothly so that no bubbles remain on the surface. Using the following recipe, a thickness of around 1.2 micron of resist is spin coated.

Table A2. PR spin coating recipe

Time	Acceleration	Speed
60 [s]	450 [rpm ²]	4000 [rpm]

After this step, the sample rest for a minute followed by putting on a hot plate for 1 minuet at 105 °C. Next step is photolithography with the following recipe with soft contact, and the light field mask shown in Fig. A2.

Table A2. Photolithography Exposure Parameters

Exposure Time	Energy	Mask Thickness	Sample Thickness	PR Thickness
6 [s]	120 [mJ]	2.37 [mm]	500 [μm]	1 [μm]

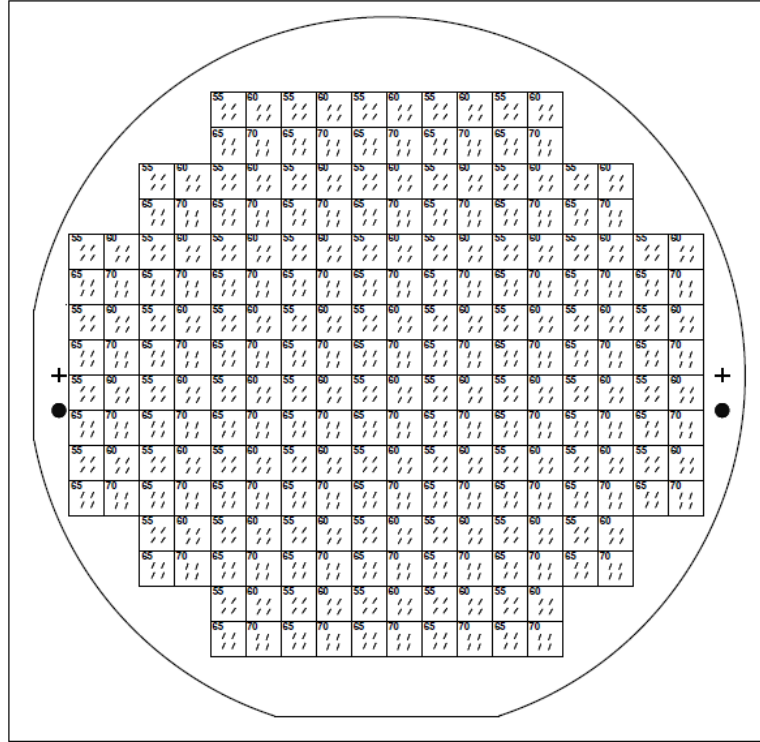


Fig. A2. First photolithography mask

Having the photolithography done, the sample is stabilized in a clean environment (yellow room) for 1 minuet. Finally, it is put inside AZ 726 MIF developer for less than 1 minuet to have the exposed regions gone completely with the lowest possible undercutting. It would be better to shake the petri dish very smoothly to have the developing process uniform.

c) Etching

HF and LF SiN_x dry etching: The top and bottom layers are etched away under a dry etching process by RIE device with the following recipe:

Table A3. RIE Recipe for LF and HF SiN_x

Temperature	Pressure	SF_6	CHF_3
20 [$^{\circ}\text{C}$]	10 [mTorr]	20 [sccm]	80 [sccm]

After 1.5 minutes, the top layer is removed.

Nickel wet etching: Using FeCl_3 85% diluted in DI-water with a ratio of 1:20, 50 nm of nickel is removed in less than 15 seconds.

d) Second photolithography

The sample after RIE is put inside hot acetone (in a glass petri dish) at 40 °C for a couple of minutes to get rid of photoresist residues, followed by rinsing in IPA, DI-water and drying by nitrogen gas. Sometimes the residue is remained on the sample that can be removed by mechanical cleaning using a soft swab. Another option is using piranha solution that is not recommended since it is dangerous. After that, the sample experience another photolithography steps like what mentioned in part (b) with a second mask shown in Fig. A3.

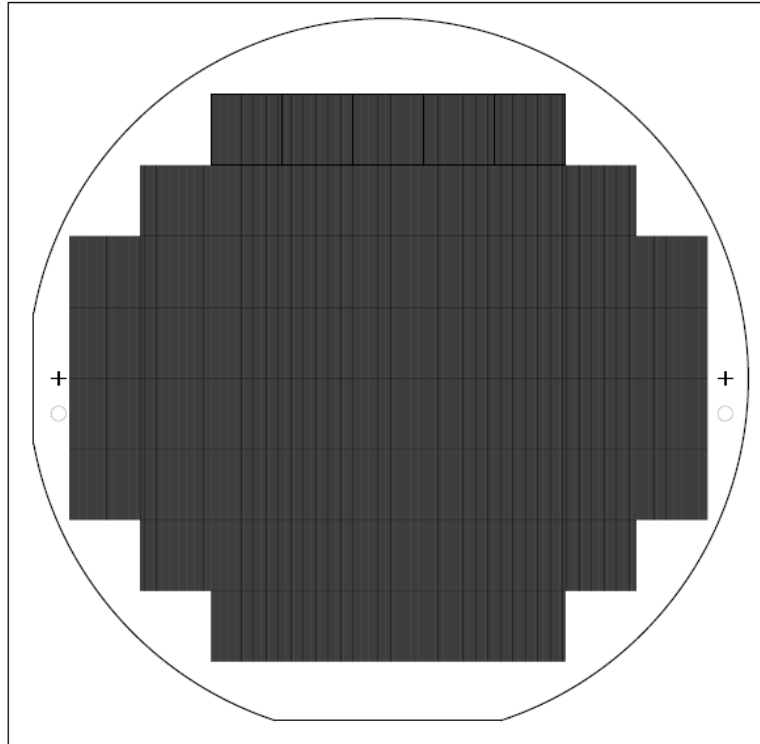


Fig. A3. second photolithography mask

e) RIE of top layer

In order to deepen the patterns into the structure, second RIE process with the same recipe of part (c) is used. The depth should be optimized since based on the conditions of the chamber

the etching rate is different. For this reason, it is recommended to first clean the chamber, run an etching process for a dummy wafer, and then performing the main etching process.

f) Wet etching of sacrificial layer

Having the topological modifications imposed to the structure, the photoresist is cleaned by acetone, IPA, DI-water, and nitrogen gas. If cutting the sample to small pieces needed, the photoresist can be cleaned afterwards. For cutting the sample, dicing saw machine or scriber device or a pen-like diamond would be useful. Then, the sample is put on a flat surface with a sharp edge, so that the scratches on the sample is parallel to those regions. Then by applying a small force, the desired regions are separated. After these steps, the sample is put inside a chromium etchant, CrO₁, for around 1.30-2 hours at ambient temperature to let the helices released without attacking the nickel layer too much. Then the swimmers can be transferred to a water container by collecting them using a magnet with a metal interlayer to be separated and let the swimmers floated in the water.